



UNIVERSITÀ DEGLI STUDI DI CATANIA

IN CONVENZIONE CON



UNIVERSITÀ DEGLI STUDI DI PALERMO

DOTTORATO DI RICERCA IN
SCIENZA DEI MATERIALI E NANOTECNOLOGIE XXIX CICLO

Aurora Piazza

**Thermally induced effects in
controlled atmosphere on Graphene and
Molybdenum disulfide**

Tutor:

Prof. S. Agnello (UniPA)

Co-Tutor:

Dr. F. Giannazzo (CNR-IMM of Catania)

Coordinatore:

Prof.ssa M. G. Grimaldi (UniCT)

Tesi per il conseguimento del titolo di Dottore di Ricerca

Alla mia famiglia

”C’è stato un sogno una volta [...];
si poteva soltanto sussurrarlo:
ogni cosa più forte di un sospiro
l’avrebbe fatto svanire.
Era così fragile”.

Il gladiatore

(*Gladiator*, Ridley Scott, 2000)

Contents

Introduction:2D Materials	1
1 Graphene	5
1.1 Physical and chemical properties	5
1.1.1 Electrical and transport properties	9
1.1.2 Optical properties	13
1.1.3 Thermal properties	14
1.1.4 Mechanical properties	15
1.1.5 Chemical properties	16
1.2 Applications	17
1.3 Graphene preparation methods	22
1.3.1 Exfoliation of Graphite	22
1.3.2 Epitaxial graphene by graphitization of Silicon Carbide	24
1.3.3 Chemical Vapor Deposition of graphene on catalytic metals	28
1.3.4 Graphene Transfer	30
1.4 Doping of Graphene	31
1.4.1 Surface transfer doping of graphene	32
1.4.2 Substitutional doping of graphene	34
1.5 Raman spectra of Graphene	35
1.5.1 Number of Layers and Orientation	39
1.5.2 The effects of Doping	42
1.5.3 The effects of Strain	45
2 Molybdenum disulfide (MoS_2)	47
2.1 Physical properties	47
2.1.1 Electronic properties	50

2.1.2	Optical properties	54
2.1.3	Thermal properties	56
2.1.4	Mechanical properties	57
2.2	Applications	58
2.3	Synthesis and exfoliation of layered MoS ₂	64
2.3.1	Mechanical exfoliation	64
2.3.2	Chemical Vapour Deposition of layered MoS ₂	65
2.3.3	Identifying monolayers	65
2.4	Tuning the MoS ₂ properties via thermal or plasma treatment	67
3	Experimental Techniques	71
3.1	Theoretical background of the employed experimental techniques	71
3.1.1	Raman spectroscopy	71
3.1.2	Raman microscopy	83
3.1.3	Atomic Force Microscopy (AFM)	85
3.1.4	Amplitude Modulation AFM	91
3.1.5	AFM Image Modes	97
3.2	Experimental Set-up	100
3.2.1	μ -Raman spectrometer	100
3.2.2	Atomic Force Microscope	103
4	Materials and Treatments	107
4.1	Materials	107
4.1.1	Gr on C-face of 4H-SiC	108
4.1.2	Gr on SiO ₂ /Si and Gr on Al ₂ O ₃ /Si	109
4.1.3	MoS ₂ on SiO ₂ /Si	110
4.2	Treatments	110
4.2.1	Thermal treatments in muffle oven	110
4.2.2	Thermal treatments in situ	112
4.2.3	Thermal treatments in PARR reactor	112
5	Experimental Results	115
5.1	Graphene on C-face of SiC	115
5.2	Graphene on SiO ₂ /Si	123
5.2.1	Effects of thermal treatment in an Oxygen atmosphere	124

5.2.2	Aging effect	132
5.2.3	Effects of thermal treatment vs. Atmosphere .	136
5.2.4	In situ study of thermal effects on Gr	146
5.2.5	Electrical characterization of doping effect induced by oxygen	151
5.3	Graphene on Al ₂ O ₃ /Si	153
5.3.1	Effects of thermal treatment in an Oxygen atmosphere	155
5.4	MoS ₂ on SiO ₂ /Si	157
5.4.1	Effects of thermal treatment in an Oxygen atmosphere	159
	Summary	163
	Bibliography	167
	Curriculum Vitae	195
	Publications	197
	Conferences participation	199
	Acknowledgments	201

Introduction:2D Materials

Since the discovery of fullerene and single layer carbon nanotubes (CNT), which are 0D and 1D carbon nanomaterials respectively, researchers tried to isolate 2D graphitic materials or to make 1D nanoribbons from 2D crystals. The same chemical element or compound can exhibit different properties in different dimensionality, which not only defines the atomic structure of the material but also determines the properties to a significant degree [1, 2, 3, 4, 5]. The early results came since 2004 with the first isolation and electrical characterization of graphene (Gr) transistors published by Geim's group [6]. In the last 10 years more than a dozen kinds of 2D crystals have been isolated and studied and now the 2D materials family includes not just carbon materials but also transition metal dichalcogenides (TMDCs), oxides, and layered metals.

Layered Van der Waals materials, existing in nature in the bulk form, represent the most common source of 2D materials. Layered materials exhibit strong in-plane bonds, while weak Van der Waals forces between the layers make them ready for exfoliation. Among the most promising applications of 2D materials are electronic devices [2, 3, 7]. In relation to electrical properties, we can have a complete family of electric materials from the 2D crystals, such as superconductors, metallic materials, semimetals, semiconductors, insulators. Figure 1 shows the list of all the current members in the 2D layered materials family. However, stability is a critical issue. The blue shaded materials are stable under ambient conditions (room temperature in air) in monolayers; those probably stable in air are shaded green but those

that may be stable only in inert atmosphere are shaded pink. Grey shading means monolayer has been exfoliated and verified by atomic force microscopy (AFM), but no further information has yet been provided.

Graphene family	Graphene	hBN 'white graphene'	BCN	Fluorographene	Graphene oxide
2D chalcogenides	MoS ₂ , WS ₂ , MoSe ₂ , WSe ₂		Semiconducting dichalcogenides: MoTe ₂ , WTe ₂ , ZrS ₂ , ZrSe ₂ and so on	Metallic dichalcogenides: NbSe ₂ , NbS ₂ , TaS ₂ , TiS ₂ , NiSe ₂ and so on	
				Layered semiconductors: GaSe, GaTe, InSe, Bi ₂ Se ₃ and so on	
2D oxides	Micas, BSCCO	MoO ₃ , WO ₃	Perovskite-type: LaNb ₂ O ₇ , (Ca,Sr) ₂ Nb ₃ O ₁₀ , Bi ₄ Ti ₃ O ₁₂ , Ca ₂ Ta ₂ TiO ₁₀ and so on		Hydroxides: Ni(OH) ₂ , Eu(OH) ₂ and so on
	Layered Cu oxides	TiO ₂ , MnO ₂ , V ₂ O ₅ , TaO ₃ , RuO ₂ and so on			Others

Figure 1: 2D materials family [7].

Three rules of thumb to obtain a 2D crystal from its 3D layered parent can be helpful for the search of new 2D materials: first, 3D layered materials with high melting temperature, typically over 1000°C, have better chances; second, potential 3D layered better parents have chemical inertness; third, insulating and semiconducting 2D crystals are more likely to be stable after exfoliation or synthesis [7].

In addition to the isolation of a single atomic plane of 2D material, the overlap of the individual layers by means of Van der Waals bonds, with consequent formation of heterostructures, would reveal new phenomena.

These Van der Waals heterostructures, as schematically shown in fig. 2, are promising for the creation of new devices with multilayer specially chosen, because there is no strict requirement related to lattice matching between the stacked 2D crystals [7].

Besides the exfoliation from parent bulk crystals, from which small flakes of 2D materials for laboratory experiments are typically obtained, research have been focused in the last years to develop methods for the growth of high quality 2D materials on large area.

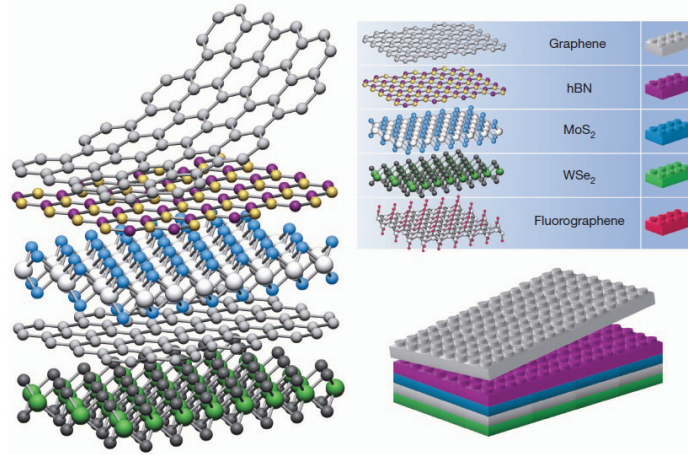


Figure 2: Common 2D materials: Graphene, MoS_2 , hBN, WSe and Fluorographene, with a schematic example of the "building" of Van der Waals heterostructures [7].

In the case of Gr, the two main scalable approaches to obtain single or few layer films with excellent electronic quality on large area are the chemical vapour deposition (CVD) on catalytic metal substrates [8] and the thermal decomposition of silicon carbide by high temperature thermal processes [9, 10]. CVD approaches for the growth of other 2D materials beyond Gr, such as TMDCs, are also under development [11, 12]. Furthermore, the possibility of growing 2D materials heterostructures by the so-called Van der Waals epitaxy concept is also under investigation [13].

The thesis work is mainly focused on two 2D materials: graphene (Gr) and molybdenum disulfide (MoS_2). Particular attention has been placed on the production and characterization of the two materials, and mainly on the investigation of the effects of doping of these materials by opportune post-production treatments in controlled atmosphere by thermal procedures. One of the aims of this work, apart from considering and clarifying the physical aspects of the thermally induced processes, is to improve the performances of these 2D materials in electronic and optoelectronic field and in the perspective to study the materials for the preparation of opportune Gr/ MoS_2 heterostructures.

This thesis is mainly organized in five chapters, as follows:

Chapter 1 contains an overview of the general physical properties of Gr and its main applications; the production methods (in particular the exfoliation from graphite, the growth by chemical vapor deposition (CVD) and the epitaxial growth on SiC) and transfer of Gr on insulating substrates (such as SiO₂); of the effects due to doping (intentional or not) and how to evaluate, using the μ -Raman spectroscopy, various aspects such as the number of Gr layers, doping effects and strain effects.

Chapter 2 collects an overview of the general physical properties of MoS₂ and its main applications; the synthesis and exfoliation of layered MoS₂ (in particular the mechanical exfoliation from bulk of MoS₂ and the growth by chemical vapor deposition (CVD)) and the identification of a single layer or a few layers of MoS₂.

Chapter 3 reports an overview of the experimental techniques used, in particular Raman spectroscopy and atomic force microscopy, with a description of the equipments used.

Chapter 4 describes the samples used and the treatments to which they were subjected during the thesis work.

Chapter 5 collects the experimental activity on samples used. In particular graphene on different substrates samples were employed (SiC, SiO₂/Si, Al₂O₃/Si) and MoS₂ samples on a SiO₂/Si substrate. The graphene samples on SiO₂ and on Al₂O₃, as well as MoS₂ samples, were subjected to thermal treatments in air and in controlled atmosphere, in order to evaluate the effects and identify changes controllable as a function of temperature, atmosphere and treatment time.

A chapter with the main conclusions closes the thesis.

Chapter 1

Graphene

1.1 Physical and chemical properties

Graphene is a crystalline allotrope of carbon, consisting of a two-dimensional (2D) layer of atoms packed in a honeycomb lattice (see *Fig. 1.1*) [4]. The atomic monolayer graphene can be considered the basic structure for many carbon allotropes [4]: for example, the overlapping of different planes of graphene, bound by weak Van der Waals type forces constitutes the graphite; carbon nanotubes (CNT) are two-dimensional structures obtained by wrapping a layer of graphene in the form of a cylinder; while the fullerene, generally indicated as zero-dimensional structure, is obtained by folding on itself, in spherical form, the graphene sheet [14] (*Fig. 1.1*).

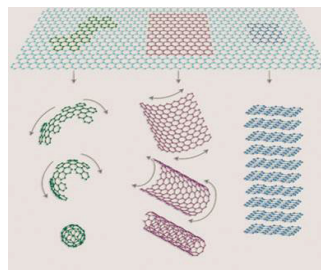


Figure 1.1: Schematic representation of the allotropes of carbon derivable from graphene. To the left, it is shown a typical structure of fullerene; in the center a carbon nanotube; to the right the graphite multilayer structure [4, 15].

In the electronic configuration of carbon ($Z = 6$), $1s^2 2s^2 2p^2$, the $1s$ orbital electrons are inert and do not contribute to chemical bonding, while those of orbitals $2s$, $2p_x$ and $2p_y$, following hybridization, form the planar sp^2 orbital, which generates the strong σ bonds among C atoms that guarantee high mechanical stability of graphene. The hybrid sp^2 orbital gives rise to bonds with angles of 120° in the plane and determines the shape of the typical hexagonal lattice structure. The remaining $2p_z$ orbital is directed perpendicular to the sp^2 orbital plane and originates the extraordinary electronic properties of graphene or gives rise to π bonds with other atoms. By linear Combination of Atomic Orbitals (LCAO) method it is possible to calculate the distribution of molecular orbitals in an aromatic system. Using this approach, the linear combination of a number N of $2p_z$ orbitals generates an equal number of molecular orbitals: $N/2$, at lower energies, are totally filled π -bonding orbitals and $N/2$, at higher energies, are totally empty π^* anti bonding orbitals. The electrons in these π and π^* orbitals are delocalized over the aromatic system. As a consequence, the C-C distance of 0.142 nm for each pair of nearest-neighbor C atoms is approximately the average length of a single ($0.154nm$) and a double bond ($0.134nm$). Considering Gr as an infinitely extended sheet, the calculation of energy band structure can be addressed solving the Schrödinger equation for the electrons in the Gr hexagonal lattice in the tight-binding approximation [16].

The Gr structure can be divided in two sub-lattices A and B, as indicated in Fig. 1.2(a) by full and empty circles respectively, in order to satisfy the equivalence conditions to define the Bravais lattices [17]. The basis lattice vectors a_1 and a_2 (see Fig. 1.2(a)) can be defined as:

$$a_1 = \frac{a}{2}(3, \sqrt{3}) \quad a_2 = \frac{a}{2}(3, -\sqrt{3}) \quad (1.1)$$

where a is the C-C distance which is exactly 0.142 nm in the case of Gr.

Considering the Gr reciprocal lattice in the momentum space, the corresponding basis vectors b_1 and b_2 are:

$$b_1 = \frac{2\pi}{3a}(1, \sqrt{3}) \quad b_2 = \frac{2\pi}{3a}(1, -\sqrt{3}) \quad (1.2)$$

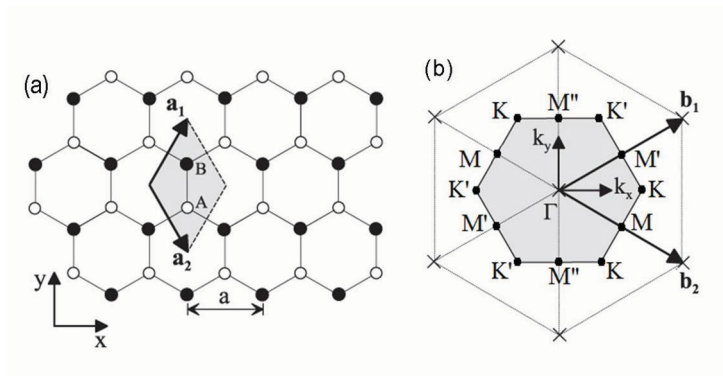


Figure 1.2: (a) Crystal structure of monolayer Gr with A and B atoms shown as empty and full circles. The shaded rhombus is the conventional unit cell while a_1 and a_2 are primitive lattice vectors. (b) Reciprocal lattice of Gr. The first Brillouin Zone is indicated with the high symmetry point Γ as the centre, K and K' as the two non-equivalent corners and M , M' , and M'' as the three non-equivalent centers of the edge while b_1 and b_2 are reciprocal lattice vectors [17].

In Fig. 1.2(b) the first Brillouin Zone of the Gr reciprocal lattice is indicated with the high symmetry point Γ as the centre, K and K' as the two non-equivalent corners and M , M' , and M'' as the three non-equivalent centers of the edge. The energy bands obtained from the solution of the Schrödinger equation in the tight-binding approximation can be expressed as:

$$E_{\pm}(k) = \pm t \sqrt{3 + f(k)} \quad (1.3)$$

where $f(k)$ is a function of the momentum k and t is the hopping energy ($t \approx 2.8eV$ estimated by ab initio calculations [18]), defined as the energy required for an electron to hop from a C atom to the three nearest-neighbors atoms.

$$f(k) = 2 \cos \sqrt{3} k_y a + 4 \cos \frac{\sqrt{3}}{2} k_y a \cos \frac{3}{2} k_x a \quad (1.4)$$

The positive sign in Equation 1.3 refers to the upper antibonding band (π^*), while the negative sign refers to the lower bonding band (π) respectively.

In Fig. 1.3(a) the calculated valence and the conduction band energies are plotted as a function of the momentum $|k|$ along the

directions defined by the high symmetry points (e.g. Γ , M and K) of the first Brillouin Zone. As is visible in *Fig. 1.3(b)*, the energy difference between the conduction and valence band is maximum in correspondence with the Brillouin zone centre Γ , whereas it is null (zero band gap) in the K and K' corners of the Brillouin zone, where the valence band maximum and conduction band minimum merge in the singularity points, called Dirac points or neutral charge point (CNP).

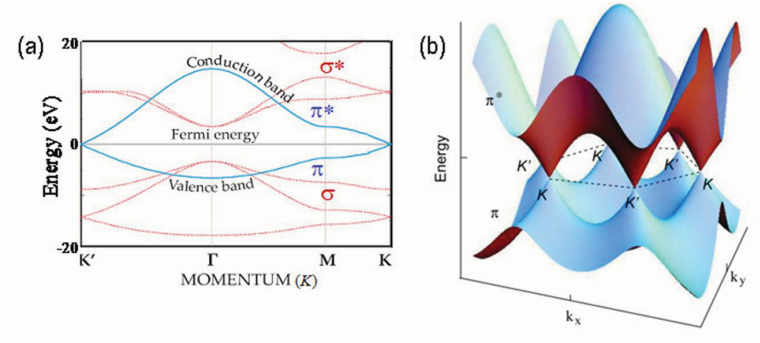


Figure 1.3: (a) Energy dispersion relation of the σ (red) and the π (blue) bands of the momentum $|k|$ along the directions defined by the high symmetry points Γ , M and K [19]. (b) Dispersion relation of Gr in the first Brillouin Zone [20].

It is important to calculate the dispersion relations close to K (or K'). For this purpose, the wavevector k can be expressed as $k = K + k'$, where K is the wavevector of the K point (with the origin in the Brillouin zone center) and k' is a wavevector with the origin in the K point. Close to the K point, the Eq. 1.3 can be expanded using the Taylor series and approximated as [16]:

$$E_{\pm}(k') \approx \pm \hbar \nu_F k' \quad (1.5)$$

where ν_F is the Fermi velocity, with a value $\nu_F \approx 10^6 m/s$. This linear dispersion relation for electrons energy in Gr is different from the usual parabolic relation:

$$E(k) = \frac{\hbar^2 k^2}{2m} \quad (1.6)$$

for electrons in semiconductors, where the electron velocity is:

$$\nu = \frac{\hbar k}{m} = \sqrt{\frac{2E}{m}} \quad (1.7)$$

The linear dispersion relation indicated earlier is similar to that of massless particles (such as photons) or that of ultra-relativistic particles, with the exception of the Fermi velocity value which is $\nu_F \approx c/300$ lower than the speed of light $c = 3 \cdot 10^8 m/s$. The linear dispersion relation in Gr has been experimentally verified in different ways, for example the most direct approach is using angle resolved photoemission spectroscopy, that is able to measure the energy and the wavevector of photoemitted electrons with energy value below the Fermi level [20].

1.1.1 Electrical and transport properties

Many of the peculiar electronic properties of Gr, such as the density of electronic states linearly depending on the energy and the ambipolar current transport [16], are a direct consequence of the linear dispersion relation.

The density of electronic states (ρ) in Gr can be calculated starting from the dispersion relation [16, 21]. Clearly, close to the Dirac point ($E = 0$) it is a linear function of the energy E :

$$\rho(E) = \frac{g_s g_\nu}{2\pi \hbar^2 \nu_F^2} |E| \quad (1.8)$$

where $g_s = 2$ and $g_\nu = 2$ are the spin and valley degeneracy, respectively.

This dependence of the density of states on the energy for Gr has strong implications both on the electronic and optical properties of Gr. For a fixed value of the Fermi energy, the carrier density, n , in Gr can be expressed as:

$$n = \int_0^\infty \rho(E) f(E) dE \quad (1.9)$$

where $\rho(E)$ is the density of states and $f(E)$ is the Fermi distribution (see Eq.1.10)

$$f(E) = \frac{1}{1 + \exp\left(\frac{E - E_F}{kT}\right)} \quad (1.10)$$

A plot of the carrier density as a function of $E_F - E_D$ (where D is the Dirac point) at a temperature $T = 300K$ is reported in *Fig.1.4*

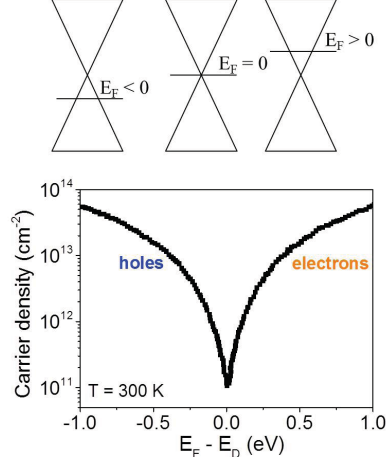


Figure 1.4: Carrier density as a function of $E_F - E_D$ at a temperature $T = 300K$ and (top) the variation of the E_F level in the Dirac cones.

The majority carriers are electrons when $E_F - E_D > 0$ (Fermi level in the conduction band) and holes when $E_F - E_D < 0$ (Fermi level in the valence band). Noteworthy, even at the neutrality point ($E_F = E_D$), where the density of states is zero, a finite value of the carrier density

$$n_i = p_i = \frac{\pi}{6} \left(\frac{k_B T}{\hbar v_F} \right)^2 \approx 6.5 \cdot 10^{10} \text{ cm}^{-2} \quad (1.11)$$

is found, due to thermal effects.

The 2D electron nature of Gr was immediately clarified since the first experiments on this material [4, 22] by the observation of the quantum Hall effect (QHE), which is the demonstration to reveal 2D electron phenomena. A peculiar feature of graphene is its characteristic Hall effect: in the traditional Hall effect, electric current, flowing on the metal surface under the presence of a transverse magnetic field, produces a potential difference (Hall potential) between the two metal faces. Because of the ratio between the potential difference and the flowing current (Hall resistivity) is directly proportional to the applied magnetic field, Hall effect is usually employed for the measurement of

magnetic fields. In a bi-dimensional metal system, at temperature close to the absolute zero, Hall resistivity becomes quantized, and assumes values around h/ne^2 (where h is the Planck's constant, n a positive integer number and e is the electric charge). However, graphene exhibits a different QHE. Because of the quantum-mechanic effect, named Berry's phase, Hall resistivity assumes only values for which n is an odd integer number. These properties were observed for the first time by Novoselov et al. at environmental temperature and not near the absolute zero, as seen in the metals, anyway demonstrating the 2D nature of graphene electrons [22]. This is due to the fact that, in graphene, the magnetic energy of electron is 1000 times higher than that of other materials.

Generally, the experimental quantity that is measured during current transport measurements is the conductivity σ , which is related to the carrier mobility μ and to the electron density n by

$$\sigma = qn\mu \quad (1.12)$$

where q is the electron charge.

Under ideal experimental conditions, such as for free-standing graphene [23], giant carrier mobility was observed, $\mu \approx 10^5 \text{cm}^2 \text{V}^{-1} \text{s}^{-1}$ at room temperature.

Between the mobility and the electron mean free path l , a relation can be obtained by a semi-classical approach based on the Boltzmann theory and the relaxation time approximation [24, 25],

$$\mu = \frac{q\nu_F\tau}{\hbar\sqrt{\pi n}} = \frac{ql}{\hbar\sqrt{\pi n}} \quad (1.13)$$

where τ is the relaxation time for a fixed value of Fermi energy. It is clear that the limiting factors for the electron mobility of Gr are directly related to the scattering mechanisms, which limit the electron mean free path.

Under ideal conditions (which allow to consider the Gr as a planar sheet with no defects, no contamination or environmental influences), the only limiting factor for the electron mean free path is the dispersion of longitudinal acoustic phonons ($l_{A,Phon}$), inversely proportional to the squared root of electron density and to the temperature T [26] as

$$l_{A,Phon} \propto \frac{1}{T\sqrt{n}} \quad (1.14)$$

As illustrated in Fig 1.5, the electron mean free path (Fig 1.5 (a)), mobility (Fig 1.5 (b)) and conductivity (Fig 1.5 (c)) can be calculated at different temperatures and plotted vs the carrier density for a micrometric Gr sample [19].

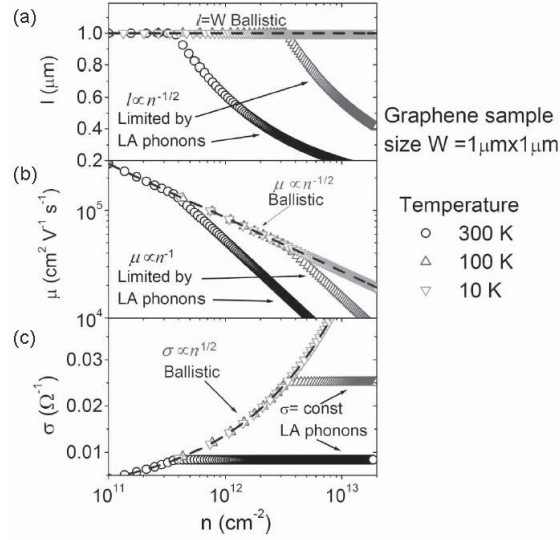


Figure 1.5: Graphs showing calculated intrinsic electron mean free path, l , (a), mobility, μ , (b) and conductivity, σ , (c) versus the carrier density, n , at three different temperatures ($T = 10, 100$ and 300K) for a Gr sample with size $W = 1\mu\text{m} \cdot 1\mu\text{m}$ [19].

Under practical experimental conditions, at room temperature and under ambient environment, the mobility as well as the electron mean free path of Gr can be significantly reduced due to several effects. For example the Gr is very sensitive to the interaction with the substrate and with the external environment [19]. Furthermore, mobility can be dependent on the Gr synthesis method (i.e. defects and deformations, chemical modifications), and on the successive manipulation processes (such as the Gr transfer procedure), and/or on any additional processes for devices fabrication, which can introduce structural and morphological damages or chemical residues [27]. Typical mobility values of Gr devices reported in the literature can range from $\sim 10^2\text{cm}^2\text{V}^{-1}\text{s}^{-1}$ to $\sim 10^4\text{cm}^2\text{V}^{-1}\text{s}^{-1}$ at room temperature [19].

1.1.2 Optical properties

The particular electronic structure of Gr is reflected also on the optical properties, in particular in the absorption and transmission of light. Notably, the optical absorption of a monolayer is quite constant ($\sim 2.3\%$) in UV-Vis and NIR range, as illustrated in Fig 1.6. Furthermore, the absorbance of a few-layers of Gr stack increases proportionally to the number of layers (for N up to 4) [28, 29, 30].

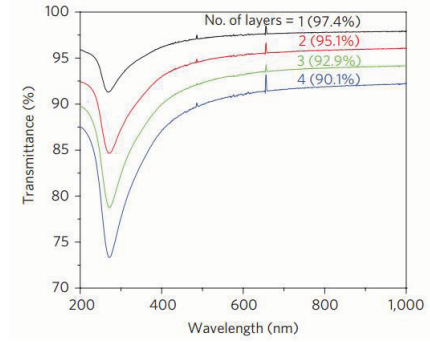


Figure 1.6: UV – VIS spectra for a different number of Gr layers, from the single layer to a four layer stack [28]. The transmitted light decreases almost proportionally with the number of layers.

As a results of the linear dispersion relation of Gr around the Dirac point, the optical conductance G (related to the optical inter-band transitions) results to be independent on frequency in a wide range of photon energies and in according to the universal optical conductance G_o [31]:

$$G(\omega) = G_o \equiv \frac{\pi e^2}{2h} \approx 6.08 \cdot 10^{-5} \Omega^{-1} \quad (1.15)$$

This constant behavior of G with the photon frequency implies that other observable quantities such as the optical transmittance T , the absorbance A and the reflectance R are frequency independent as well.

For a freestanding Gr monolayer T , R and A can be expressed applying the Fresnel equations in the thin-film, in the form:

$$T \equiv \left(1 + 2\pi \frac{G}{c}\right)^{-2} = \left(1 + \frac{\pi\alpha}{2}\right)^{-2} \approx 1 - \pi\alpha = 97.7\% \quad (1.16)$$

$$R \equiv \frac{1}{4}\pi^2\alpha^2 T < 0.1\% \quad (1.17)$$

$$A = 1 - T = 2.3\% \quad (1.18)$$

where,

$$\alpha = \frac{e^2}{\hbar c} \approx \frac{1}{137} \quad (1.19)$$

is the fine structure constant.

Despite its high absorbance (considering its atomic thickness), in absolute terms Gr can be considered as an excellent transparent conductor. It is currently investigated as a replacement of ITO for applications in optoelectronics and photovoltaic. Due to its high flexibility (see section 1.1.4), it is the ideal candidate for flexible and organic light emitting devices.

1.1.3 Thermal properties

In addition to the electronic band-structure, also the phononic dispersion relation has very important implications on some physical properties of Gr such as the thermal conductivity and the specific heat. Considering again the unit cell of the Gr lattice, formed by two carbon atoms, three Acoustic (A) and three Optical (O) phonon modes can be calculated. It is particularly relevant to consider that the dispersion relation between the phonon energy and the wave vector q is linear for low $|q|$ values, for example near to the centre of the Brillouin zone, for Longitudinal (LA) and in-plane Transverse (TA) Acoustic phonons, while the out-of-plane flexural (ZA) Acoustic phonons follows a quadratic dispersion (see Fig. 1.7). The group velocities for TA and LA in the case of Gr are from 4 to 6 times higher than those in other materials such as silicon and this property can be attributed to the strength of the sp^2 bonds and to the small mass of carbon atoms. Gr exhibits a thermal conductivity among the highest of known materials, ranging from 2000 to $5000 W m^{-1} K^{-1}$ [32, 33, 34] for suspended single layer membranes, at room temperature. The specific heat for a single layer of Gr, is mainly related to the lattice vibrations (phonons) at all practical temperatures. To date, the specific heat of single-layer of Gr was not measured directly, but it is possible to make a comparison with the specific heat of graphite. At room temperature the specific heat of graphite is $\sim 30\%$ higher than that of diamond due to the higher density of states at low phonon frequencies [35].

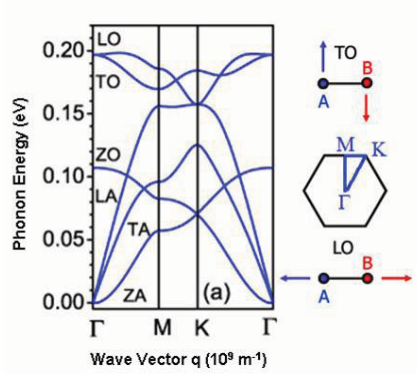


Figure 1.7: Phonon dispersion of Gr along high symmetry lines in the Brillouin zone. Three Acoustic (A) and three Optical (O) phonon modes are reported. At low q , the wave vector energy dependence is linear for Longitudinal (LA) and in-plane Transverse (TA) Acoustic phonons and quadratic for out-of-plane flexural (ZA) Acoustic Phonon [36].

The thermal conductivity κ is linearly related to the specific heat c , to the group velocity ν and to the phonon mean free path λ . In the diffusive regime (for a Gr size $L \gg \lambda$), κ can be expressed as:

$$\kappa = \sum c\nu\lambda \quad (1.20)$$

The high values of κ measured for a suspended Gr membrane are the result of the high specific heat, the high group velocities and the long phonon mean free path (600nm for suspended Gr). On the other hand, structural disorder can easily degrade the thermal conductivity of Gr [37]. Analogously to the charge transport properties described above, also the in-plane thermal conductivity is seriously conditioned when the carbon membrane is sustained by a substrate. In the case of Gr sustained on SiO_2 a decrease of the thermal conductivity of one order of magnitude occurs as a result of the coupling and scattering of Gr phonons with the substrate vibrational modes [38].

1.1.4 Mechanical properties

Also from the mechanical viewpoint, Gr reveals outstanding properties, such as a high flexibility alongside one of the highest in-plane

tensile modulus, which are related again to the peculiar 2D hexagonal structure of sp^2 hybridized carbon atoms. These mechanical properties are the basis for many potential applications of Gr. The Young's modulus is used to describe these properties whose value is given by the ratio between the stress tensor of the mechanical tension applied to the material (σ), and that of the deformation undergone (ε). If the two tensors are uniaxial, the Young's modulus along the x axis, is given by:

$$E = \frac{\sigma_x}{\varepsilon_x} = \frac{1}{V_0} \left(\frac{\partial^2 E_S}{\partial \varepsilon_x^2} \right)_{E_0} \quad (1.21)$$

where V_0 and E_0 are, respectively, values of the equilibrium volume and energy, and E_S is the strain energy. In the case of Gr, it makes more sense to consider the stiffness in the plane because of the two-dimensional nature of the material. We can then rewrite Eq. 1.21:

$$E = \frac{1}{A_0} \left(\frac{\partial^2 E_S}{\partial \varepsilon_x^2} \right)_{E_0} \quad (1.22)$$

where normalization for the equilibrium surface, A_0 , is used. A systematic experimental analysis of elastic and strength properties [39] were conducted on μm size suspended circular membranes of Gr stressed by Atomic Force Microscope (AFM) tips. By these results it was possible to calculate a Young's modulus of $1.02 \pm 0.03 TPa$ (about 200 times greater than that of steel) under experimental conditions in which the energy from in-plane strain was the most relevant contribution [40].

1.1.5 Chemical properties

Highly crystalline graphene surfaces appear to be chemically inert, and usually interact with other molecules via physical adsorption ($\pi - \pi$ interactions). However, it is possible to functionalize graphene surface by anchoring several chemical groups such as carboxyl (COOH), carbonyl (COH), hydrogen (CH) and amines (NH₂) at the edges, which are more chemically reactive. In 2009, Novoselov et al. reported the obtainment of a fully hydrogenated graphene sheet, termed "graphane" (Fig. 1.8): the hydrogenation route is reversible at 450° C, and unlike graphene, graphane behaves as a semiconductor [41]. However, the synthesis of this compound still needs to be improved and further analysis related to the C-H bonding nature using XPS should be carried out.

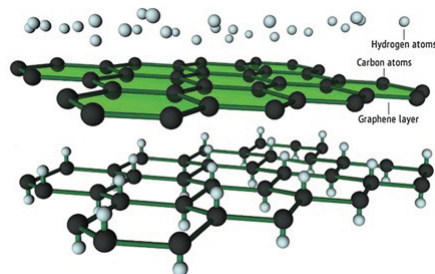


Figure 1.8: Graphane structure. (Top) Schematic image of the reaction between graphite and hydrogen; (bottom) Schematic image of Graphane [42].

In order to make the graphene surface more chemically reactive, either surface defects or high degrees of curvature need to be introduced. In several studies the graphene reactivity is increased by reacting it with halogen atoms such as fluorine [43].

1.2 Applications

Thanks to its extraordinary properties, graphene has found application in field-effect transistors, in transparent conducting electrodes, in functional devices such as energy storage systems and photovoltaics, gas sensors, and in biological field.

Transparent conductors Transparent conductors (TCs) are an essential part of different electronic devices, such as touch screen displays, electronic papers, organic light-emitting diodes (OLEDs) (a schematic example is shown in Fig. 1.9), and other photonic technologies: they require a low sheet resistance with high transmittance (of over 90%) depending on the specific application. With high electrical conductivity, high carrier mobility, and moderately high optical transmittance in the visible range of the spectrum, graphene materials are the best candidates for the development of a new category of TCs. Different researches, in recent years, have demonstrated that graphene has a transmittance and sheet resistance combination comparable to traditionally indium tin oxide (ITO), and can be a valid alternative to it as transparent conducting coating in electronic devices, furthermore, graphene is cheaper than ITO and is characterized

by mechanical flexibility and chemical durability, important features for flexible electronic devices, in which ITO usually fails [28].

Solar cells and similar light harvesting devices are strongly influenced by the type of TC used. Transparent conducting films of solution-processed [44] and CVD grown graphene [45] have been used and implemented for inorganic [46], organic, hybrid [47] and dye sensitized solar cells (DSSC) [48, 49]. In particular for DSSC, graphene replaces ITO at the anode, reducing the recombination rate and thus improving the efficiency of the device [48].

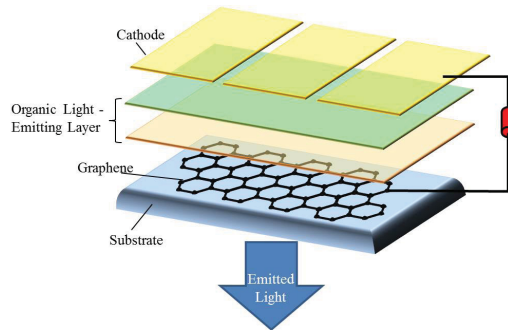


Figure 1.9: OLED using graphene as transparent conductor.

Field effect transistors (FETs) Due to its excellent carrier mobility and saturation velocity, as well as the ambipolar current transport, graphene has been considered for next generation high frequency transistors applications. The field effect transistor (FET) is currently the most used device in the fields of analog and digital (i.e. logic) electronics. FET is made up of a doped semiconductor substrate, usually Si, on which three terminals are applied: gate, source and drain (as shown in Fig. 1.10). The operation of these devices is based on the ability to control the electrical conductivity of the channel region, and thus the electric current passing between the source and drain contacts, by applying a bias to the gate electrode. Since the experimental values of the field-effect mobility of graphene are one order of magnitude higher than that of Si, GFETs are able to operate at higher frequency than Si FETs. Furthermore, the use of graphene affords to achieve chips having lower size than that of traditional FETs. The world smallest transistor, having a thickness

of one atom and a width of about ten, was created in 2008 [50]. GFETs with 100 GHz switching frequency have been reported by Lin et al. [51]. In addition, studies have been carried out on graphene p-n junctions, in which carrier type and density in two adjacent regions were locally controlled by electrostatic gating [52]. Among the major limitations of GFETs is that they cannot be turned off effectively due to the absence of a band gap and therefore are not suitable for logic applications (that require switching between the two states of conductivity). Several researches are being targeted at opening a band gap in graphene through different approaches: nanoribbons formation [53], application of a perpendicular electric field to bilayer graphene [9] and chemically modified graphene [41]. Nevertheless, all of these approaches have so far been unable to open a band gap wider than 360 meV [54], limiting the on/off ratio to about 10^3 , much less than the required 10^6 for logic applications. Moreover, they can often introduce defects and contaminants into GFETs, reducing its performances [55]. The issue of the low on/off ratio can be addressed adopting new transistors architectures different than lateral FETs. Although such devices allow for on/off ratios of 10^6 , more work on integration is required to enable the full use of graphene for logic applications.

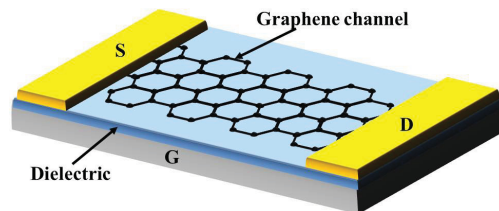


Figure 1.10: Structure of field effect graphene transistor: a source (*S*) and a drain (*D*) are connected through a graphene channel, which allows the passage of an electron at time.

Chemical and biological sensors Another interesting application of graphene is in the field of the chemical and biological sensors. Its ultrasensibility is due to its large surface area, its single-atom thickness and its low electric noise, and can be improved by functionalizing graphene with various organic and inorganic species (atoms, nanoparticles, polypeptides and nucleotides). The atomically thin structure

can also enable many novel sensing schemes, such as nanoporous membranes for DNA probing and sequencing [56, 57]. Different studies have shown that graphene molecular sensors are able to detect gases such as NO_2 , NH_3 , H_2 and CO with a sensibility up to some parts per million [58]. There are two types of chemical sensors based on graphene: the GFETs, in which a variation in the conductivity responds to nearby charge fluctuation brought by molecular binding near or on graphene, and graphene or graphene-derivate electrochemical sensors, which detect redox potential and the current of certain species. Lu et al. observed that GFETs, having graphene functionalized with single stranded DNA, are highly sensitized towards vapor analytes [59]. To realize biological sensors, graphene has been functionalized with receptors that selectively bind to specific target species. In fact, ultrasensitive devices based on graphene are able to detect a range of biological molecules such as glucose, cholesterol, hemoglobin and DNA. For example, Ohno et al. obtained an aptamer (specific oligonucleotide or peptide filaments) modified GFETs, having a high sensitivity and good selectivity toward immunoglobulin E protein [60].

Drug delivery systems and bio-applications In biology and biotechnological fields, graphene has recently gained great attention due to its large surface area, chemical purity and its ability to be functionalized. Graphene can solubilize and bind drug molecules, acting as a drug delivery vehicle: thanks to its lipophilic character, graphene sustains the passage of some drugs through biological membranes. So far, most of the work is focused on the study and investigation the loading and in vitro behavior of aromatic anticancer drugs [61]. However, given the safety and regulatory obstacles and long timescale associated with drug development, graphene-based drug delivery systems will be commercially introduced in 15 years.

Thanks to its extraordinary mechanical properties graphene can also found application in tissue engineering field. In fact graphene could be incorporated into the scaffold material to enhance its mechanical properties and modulate its biological performance in areas such as cell adhesion and proliferation [61]. Moreover, various graphene-based nanomaterials have been used to fabricate functionalized biosystems

integrated with nucleic acids, peptides, proteins and even cells (Fig. 1.11) [62].

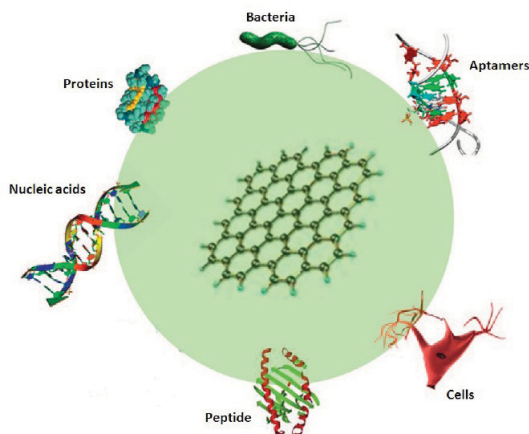


Figure 1.11: Graphene and its derivatives have been reported to be functionalized with peptides, DNAs, proteins, aptamers, and cells through physical adsorption or chemical conjugation. The functionalized graphene biosystems with unique properties have been used to build up biosensors, and biodevices [62].

Nevertheless, it is important to underline that before graphene can be widely used in such biomedical applications, the understanding of its biocompatibility, biodistribution and its toxicity is needed. There are still few studies related to graphene toxicity, which is strongly influenced by its morphology, size and synthesis method.

Electrochemical devices Recently, graphene has been used as a material for the construction of supercapacitors, thanks to its high intrinsic electrical conductivity, good resistance to oxidative processes, high temperature stability and an accessible and defined pore structure. In 2009, Stoller et al. realized the first prototype of graphene-based electrochemical double-layer capacitors, having an optimal energy and density power (Fig. 1.12) [63].

Graphene nanosheets are also used as support material for platinum catalysis in fuel cells, due to the strong interaction with platinum and its small particle sizes, graphene leads to an increase of the cat-

alytic activity in methanol fuel cells [64].

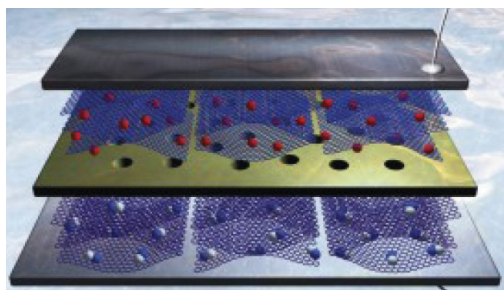


Figure 1.12: In a supercapacitor device two high-surface-area graphene-based electrodes (blue and purple hexagonal planes) are separated by a membrane (yellow). Upon charging, anions (white and blue merged spheres) and cations (red spheres) of the electrolyte accumulate at the vicinity of the graphene surface. Ions are electrically isolated from the carbon material by the electrochemical double layer that is serving as a molecular dielectric [65].

However, in order to replace the common supporting material (activate carbon, carbon black, graphite) in such devices, graphene must be superior in terms of performance and cost. With its high theoretical surface area and ability to facilitate electrons or hole transfer along its two-dimensional surface, graphene can be also used in lithium ions batteries, since, the introduction of graphene should help to overcome some issues due to the poor electrical conductivity, and should give rise to novel coreshell or sandwich-type nanocomposite structures. Yoo et al. demonstrated that the use of graphene nanosheets in conjunction with carbon nanotubes and fullerenes increased the battery charge capacity [66].

1.3 Graphene preparation methods

1.3.1 Exfoliation of Graphite

Andre Geim and Konstantin Novoselov were the first, in 2004, to be able to experimentally isolate graphene [6], starting from bulk graphite, by the scotch tape technique and transferring it on the surface of a silicon dioxide (SiO_2) on Silicon (Si). Monolayer flakes were identified exploiting the optical contrast due to the interference of light

reflected at Gr/SiO_2 and SiO_2/Si interfaces, which is maximized for properly chosen SiO_2 thicknesses [6]. Innovative experiments, usefully clarifying the properties of this 2D material, led the two researchers to win the Nobel prize for physics in 2010; demonstrating the interest from the scientific community in this field of research. The used production technique, generally known as mechanical exfoliation, still provides the best quality Gr crystallites and is currently used for several research purposes. However, due to the limited lateral size of obtained Gr flakes (not exceeding $100\mu m$ in the best conditions) [4], this approach is not suitable for all those activities that require larger membranes on extended area. Several other strategies have been proposed to increase the yield and the efficiency of the exfoliation approach [67]. Alternatively it is possible to enhance the exfoliation yield by oxidative and chemical-intercalation reactions which limit the van der Waals interactions as well as the hydrophobic character of the carbon membrane in order to enhance its dispersibility in a wide range of solvents. The weakness in this case is connected to the reverse reaction to reduce Gr oxide, for example with hydrazine hydrate, which gives back a partially damaged and not totally reduced Gr [68, 69].

It is possible to obtain single-layer of materials, with high efficiency, using thermal exfoliation techniques. Rapid high temperature heating through graphite oxide [70] as well as low temperature exfoliation of graphite under vacuum [67], have yielded some of the highest surface areas of all exfoliation methods. In the years several methods of exfoliation, such as the electrolytic exfoliation, or the thermal quenching have been proposed which exploit high temperatures and fast cooling down steps, or finally the superficial fluid exfoliation in organic solvent and in presence of surfactants.

Nevertheless, all these approaches are suitable to create macroscopic amounts of Gr, but are not suitable for applications in the microelectronic field.

To date, the real alternatives to produce large area Gr appropriate for electronic applications are the graphitization of Silicon Carbide (SiC) surface and the Chemical Vapor Deposition (CVD) of Gr on catalytic metals. Both strategies are able to give high quality, controllable thickness and wafer scale Gr membranes, suitable for several

applications even in microelectronic field.

1.3.2 Epitaxial graphene by graphitization of Silicon Carbide

Silicon Carbide (SiC) is a semiconductor that currently constitutes the material of choice for high power electronics [71]. Different polytypes of SiC can be found in nature, but the most used ones for applications are the hexagonal polytypes (6H- and 4H-SiC). Si and C atoms are covalently bonded in SiC. The hexagonal polytypes consist in a stacking of planes formed by Si-C dimers with peculiar sequence, giving rise to the 4H- or 6H-SiC. As a consequence, SiC wafers always expose two faces with different terminations, (the Si-terminated face (0001) and the C-terminated face (000 $\bar{1}$)), which are oriented orthogonally to the growth axis (c-axis) of the hexagonal lattice as also illustrated in Fig. 1.13.

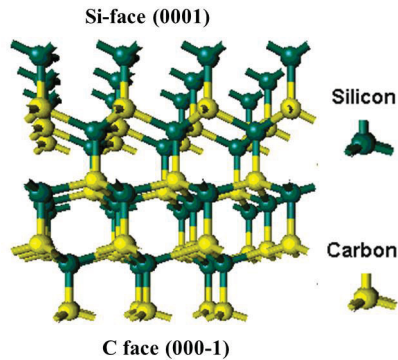


Figure 1.13: Illustration of the hexagonal polytype SiC which exposes two faces with different terminations: the Si-face (0001) and the C-face (000 $\bar{1}$)

Subjecting the SiC at high temperature thermal processes, it occurs a sublimation of Si from the surface, leaving an excess of C, which is reorganized to form graphene-like islands that grow to form an extended film of Gr. Indeed, almost in the same period when the first experiments on Gr exfoliated from graphite were carried at Manchester (UK), the group led by W. de Heer at Georgiatech (US) [72] started to work on the controlled graphitization of SiC to achieve the formation of single or few layers of Gr.

At first, the graphitization of SiC was mainly carried out in Ultra-High Vacuum (UHV) in a range of temperatures around 1200-1400°C. In the years this growth technique was exploited to obtain Gr layers on both the (0001) Si-face [9, 73], and the (000 $\bar{1}$) C-face [10, 74]. It was clear, however, that the growth of Gr on Si-face was easier and more controllable than the growth on the C-face. In addition, on Si-face thinner layer compared to those on the C-face can be obtained. Moreover, Gr grown on both sides by the UHV method was affected by a restricted homogeneity and by a low quality on large area. Greater homogeneity and larger Gr domains with uniform thickness were obtained by performing the thermal treatments in inert gas (Ar) atmosphere at higher pressure (up to the atmospheric one) and at higher temperatures (above 1600°C) [75].

The possibility of growing uniform Gr layers on large area opened the way to the application of sophisticated spectroscopic techniques (typically requiring mm² sample areas), such as X-ray Photoemission Spectroscopy (XPS) and Angle-Resolved Inverse Photoemission Spectroscopy (ARPES), which are able to provide information both on the chemical bonds and on the electronic structure of epitaxial Gr [76]. The growth of Gr layers, in addition to pressure and temperature depends, also, on the orientation of SiC. The structure and electronics properties of graphene layers vary if it is grown on Si-face (0001) or on C-face (000 $\bar{1}$) of the SiC. Single or few layers of Gr can be obtained on the Si-face, with a very good control on the thickness. These layers also exhibit a very precise epitaxial alignment with respect to the substrate and are stacked each other with the Bernal stacking (the same stacking of Gr sheets within graphite). On the other hand, under similar experimental conditions, multilayers of Gr are obtained on the C face, with a poor control on the uniformity. Moreover, a rotational (turbostratic) misorientation between the different layers is observed [77]. These different structural features are evident from Low Energy Electron Diffraction (LEED) patterns, reported in Fig. 1.14 for Gr layers on the Si-face and C-face of SiC. These different structural characteristics are also reflected in the ARPES measurements. Representative ARPES spectra for single layer and bilayer Gr on the Si-face are reported in Fig. 1.14 (c) and (d) respectively, clearly indicating a modification of the band structure with increasing the number of

layers, consistently with the Bernal stacking. In the case of Gr multilayers on the C-face, the ARPES spectra consist of several Dirac cones shifted along the wavevector axis (Fig. 1.14 (e)), indicating that the different Gr layers are electronically decoupled each other.

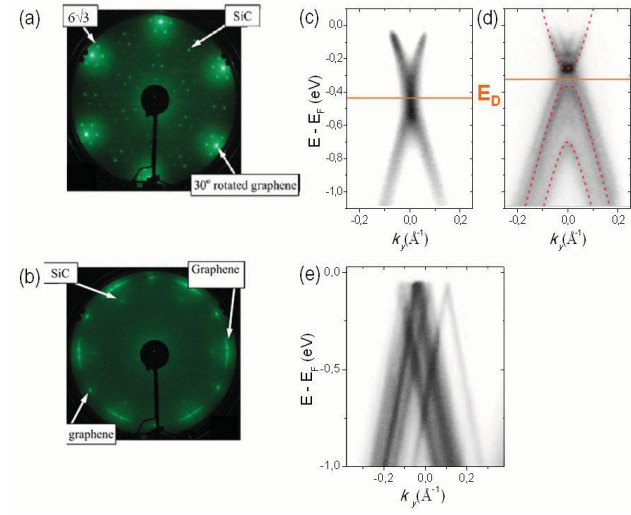


Figure 1.14: LEED patterns for Gr grown on (a) the Si-face and on (b) the C-face. Dispersion of the π - bands measured with ARPES perpendicular to the ΓK -direction of the Gr Brillouin zone for (c) a Gr single layer and (d) a double layer on the Si-face and for (e) multilayer Gr on the C-face.

The different structural and electronic properties between Gr on the Si and C faces are the consequence of different growth mechanisms. To date, a good understanding of the Gr growth mechanism on the Si-face has been reached. In this case, the growth is mediated by the formation of a $(6\sqrt{3} \times 6\sqrt{3})R30^\circ$ reconstructed C interface layer (called "buffer layer") which represents the precursor of Gr formation [78]. The "buffer layer" consists of a layer of carbon atoms with hexagonal lattice, which are partially sp^3 hybridized due to covalent bonds with Si atoms of the substrate. The first Gr layer is obtained after the formation of a new interfacial buffer layer and the conversion of the old one into a fully sp^2 hybridized sheet. Furthermore, the role played by the buffer layer as a template for Gr growth fully explains the stacking order (Bernal stacking) between Gr layers on the Si-face [79].

To date, a clear understanding of Gr growth on the C-face of SiC has not been reached. Differently than for Si-face, an interfacial buffer layer has not been observed for the C-face and this can account for the rotational disorder between stacked Gr layers. Recently, the presence of ~ 1 nm thick interfacial amorphous layer of SiC has been observed by atomic resolution transmission electron microscopy (with low energy, 60 keV, electron beam) for Gr grown at high temperatures and atmospheric pressure on the C-face of SiC [80]. Interestingly this layer exhibits a not uniform composition, the presence of Si decreases, while increasing that of C toward the interface with Gr. This amorphous layer can work as a precursor for Gr formation on the C-face of SiC.

Among the most interesting properties of the Gr on SiC (0001) system is the possibility of tailoring the electronic properties by intercalation of proper atomic species at the interface. The most commonly used intercalating species is hydrogen. During annealing at temperatures between 600°C and 1000°C in molecular hydrogen at atmospheric pressures, hydrogen intercalation occurs, which decouples the buffer layer from the SiC (0001) surface [81]. The intercalation with hydrogen causes the breaking of the covalent bonds between the sp^3 -hybridized C atoms of the buffer layer and the Si atom of the SiC (0001) surface with the conversion of the buffer layer into a Quasi-Free-standing Epitaxial Graphene (QFEG) layer (see, Fig. 1.15).

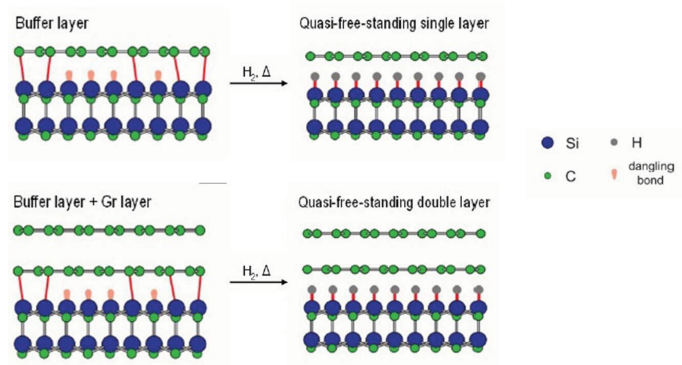


Figure 1.15: Schematic illustration before and after the hydrogen treatment for an as grown buffer layer (up) and an as grown buffer layer plus a second Gr layer (down) [81].

1.3.3 Chemical Vapor Deposition of graphene on catalytic metals

The most promising method, low cost and very accessible for the production of graphene on a large area is the chemical vapor deposition (CVD) on metal substrates (Ni, Pd, Ru, Ir and Cu), since with this approach high quality samples are get [8]. The catalytic metal is exposed to an organic gas flow (such as methane), that decomposes to carbon radicals to form few layers or even a single layer of Gr. The epitaxial growth on catalytic metals is ruled by two different mechanisms, which depend on the solubility of the carbon atoms in the metal at the growth temperature. In this context, Ni and Cu, which are the most used substrates for Gr CVD growth [8, 19], exhibit a different behavior, due to the very different C solid solubilities in these two materials. The maximum solubility of C atoms in Ni is 0.6% at the melting temperature, $T_M = 1455^\circ\text{C}$ (as illustrated in Fig. 1.16 (c)), whereas in the case of Cu its value at the melting temperature, $T_M = 1085^\circ\text{C}$, is much lower (0.0076%), as illustrated in Fig. 1.16 (d). As a result, when a polycrystalline Ni substrate is exposed at high temperature ($\sim 900 \div 1000^\circ\text{C}$) to the hydrocarbon gas, this decomposes in carbon radicals, which dissolves into the metal bulk. During the cooling down step, due to the reduced C solubility in the metal with decreasing the temperature, carbon atoms segregate on Ni surface forming graphitic layers (see Fig. 1.16 (a)).

On the other hand, C atoms do not dissolve within Cu, due to the low solubility limit, but diffuse on its surface. Studies on the coating as a function of time of growth of graphene on Cu have shown that the process is self-limiting, that is, after the entire surface of the Cu was covered with graphene, subsequent layers of graphene are not formed. In addition, Raman analysis performed on the entire sample at the end of growth shows that 95% of the surface is covered with a single layer of graphene, while the rest is covered by multilayers, which are predominantly formed in the proximity of the Cu grain boundaries [8, 82].

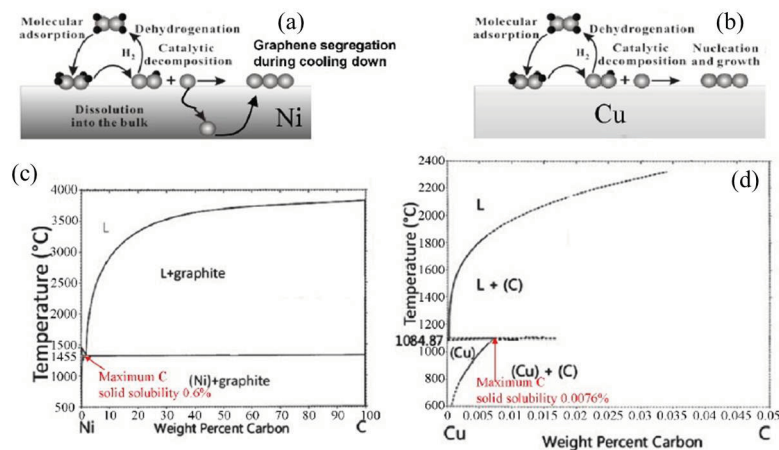


Figure 1.16: Schematization of the growth process of Gr by CVD on Ni (a) and on Cu (b). Below the phase diagrams for the binary system Ni-C (c) and Cu-C (d): the maximum solid solubility of C is strongly different in Ni and Cu, with $\sim 0.6\%$ at $T_M = 1455^\circ C$ and $\sim 0.0076\%$ at $T_M = 1085^\circ C$ for Ni and Cu respectively [82].

Fig. 1.17 (A) shows a SEM (scanning electron microscopy) image of graphene domains on Cu in the initial stages of growth, when the surface is partially covered [8]. An image at higher resolution (Fig. 1.17 (B)) shows the presence of steps and corrugations (wrinkles) on the surface of the graphene, and evidence of multilayer near the edges of the different domains [8].

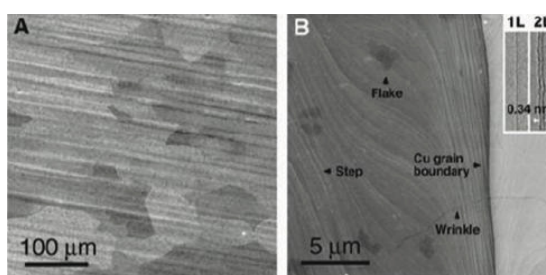


Figure 1.17: (A) Scanning electron microscopy (SEM) image of graphene grown on Cu by CVD. (B) SEM image at higher resolution showing edges of graphene domains where there are multilayers; the inset shows the folding on the edge of the graphene [8].

The grain boundaries separating the domains represent one of the main factors that degrade the electrical and mechanical properties of this material [83, 84]. Moreover, the as-grown Gr shows characteristic corrugations generically called "wrinkles" [8]. Their formation originates from the difference between the negative thermal expansion coefficient of Gr ($\lambda_{Gr} = -6 \cdot 10^{-6} K^{-1}$ at $27^\circ C$) and the Cu positive one ($\lambda_{Cu} = 17 \cdot 10^{-6} K^{-1}$). These literature results led to the conclusion that, to date, the most convenient method to produce graphene is the growth on catalytic metals. Between the substrate metals Cu is preferred, since higher quality samples are obtained, whereas in the case of Ni thin layers of graphite are found and the process is not self-limiting, by contrast to Gr grown on Cu [8].

1.3.4 Graphene Transfer

For the use of Gr in many applications, after growth by CVD on metals it is necessary the transfer to other substrates. Generally, the most used approach to separate Gr from the growth substrate exploits the chemical etching of the metal layer. Ni and Cu are commonly etched away by chemical solutions such as $FeCl_3$ [85], $Fe(NO_3)_3$ [86], $(NH_4)_2S_2O_8$ [28]. In principle, Gr can be fished using the target substrate directly from the etching solution after the complete dissolution of the metal [85], but this procedure exposes the Gr membranes to a high probability of rippling and breaking and cannot be applied for large area samples. To reduce these problems, a support polymeric film is typically attached to the Gr membrane, before metal etching. The polymeric film has the purpose of preserving the integrity of Gr and planarity as well as to improve the handling. One of the polymers adopted is the Poly(Methyl-MethAcrylate)(PMMA), which is typically deposited on the top of Gr by spin-coating. After metal etching, the PMMA/Gr film is placed on the desired target substrate and the PMMA layer is removed using proper solvents (acetone, as an example, see fig. 1.18) [87]. Notwithstanding, this approach is affected by several weaknesses: due to the rigidity of the baked PMMA layer, Gr is frozen with the wrinkled topography formed during the cooling down step of the CVD growth and coherently transferred on the final substrate. This rigid causes a bad accommodation on the target surface so that Gr risks of being rippled and cracked during the

PMMA dissolution. To overcome this limitation, several attempts have been made, such as the deposition of a second PMMA layer directly over the transferred PMMA/Gr layer to dissolve the first polymer film [86] or the introduction of a heat treatment step to increase the adhesion between the PMMA/Gr stack and the substrate [88], which also involves a partial softening of the polymer. PMMA has another weakness: the partial covalent bonding with the Gr causes a partial removal of polymer, with a consequent partial degradation of the Gr electrical performances. The Gr cleanliness and the related properties can be improved by appropriately choosing chemical baths to dissolve PMMA [89] or alternatively exploiting thermal annealing in H_2 gas at the appropriate temperature [89, 90], without damaging the Gr.

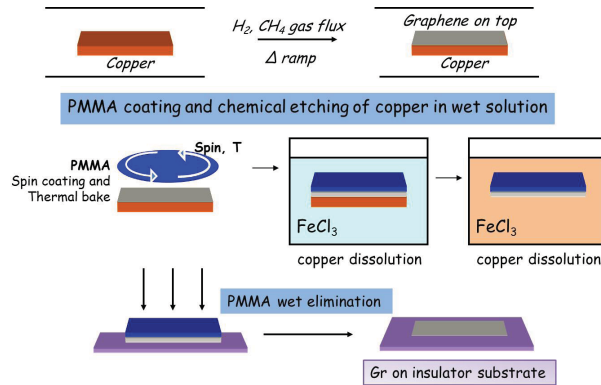


Figure 1.18: Schematic illustration of the procedure for CVD growth of graphene on Cu and of the transfer procedure with PMMA on an insulating substrate (for example SiO_2).

In spite of the above mentioned issues related to the need of Gr transfer, CVD deposition on catalytic metals is currently the most used approach to produce Gr on large area for electronics applications, due to the relatively lower cost of metal substrates (as compared to SiC), and to its versatility.

1.4 Doping of Graphene

The π electrons in graphene play a key role to determine many of its electrical properties, and the doping effect is of particular

sensitivity because of the interaction of this π band with impurities [91]. This sensitivity can be a disadvantage because of the difficulty to avoid charged impurities [92]; on the other hand, it is a key to improve the electrical conductivity and in the use of graphene as a transparent conductive film to achieve sheet resistances comparable to ITO [28].

There are different ways to dope the Gr. Generally the doping takes place during the phase of growth of the material, using suitable precursors (as we will see in section 1.4.2). It may be necessary, however, to dope graphene after the growth phase. For this purpose various studies have been done on the most suitable methods for inducing and control doping. For example Masubuchi et al. [93] have created a graphene/graphene oxide/graphene junction by locally oxidizing a layer of Gr with the aid of atomic force microscopy (AFM) tip showing the possibility to tune the degree of oxidation and doping. Another example is the photochemical oxidation of Gr using a UV light source in the presence of oxygen [94]. Among the most studied and used methods is the use of heat treatments or plasma treatments under controlled atmosphere, by exploiting the doping for charge transfer (as we shall see in the next paragraph). In these years there have been several experiments using different atmospheres (such as oxygen, nitrogen, fluorine, hydrogen, argon, etc...) [95, 96, 97] in order to evaluate the effects obtained and subdividing them even varying the temperature [98].

1.4.1 Surface transfer doping of graphene

The large surface-to-volume ratio makes graphene extremely sensitive to the environment. The adsorption of properly chosen chemical groups on the surface of graphene has the ability to inject or withdraw electrons, creating n-type or p-type doping [99]. These molecules, which are adsorbed on the surface, must be controlled in order to create a material with a specific type of doping. Most importantly, the nature of the adsorption (chemisorbed or physisorbed, for example) will impact the stability of graphene doping. Previous research has shown that the doping level in graphene can be modified through adsorption or desorption of gas/vapor molecules (for example, O₂, CO₂, N₂, H₂O, CO, etc) [100]. Attachment/detachment of molecules

changes the local carrier concentration in graphene that leads to step-like changes in the resistance. In addition, contamination and adsorbed molecules from the ambient air play a significant role in imperfections and large variance in the mobility of graphene-based field effect transistors [101]. To achieve desired functionalities, a deeper understanding of graphene surface chemistry is required. Moreover, controlled tuning of the Fermi level in graphene by doping would be highly desirable in view of the use of graphene in realistic microelectronics. The functional groups can also be introduced in the process of fabricating graphene-based devices due to exposure to chemicals or some thermal treatment process. As explained earlier, high quality CVD graphene enables the preparation of large area films from which transparent electrodes, transistors, and other electronic devices can be developed [8, 85, 102]. However, the synthesis of CVD graphene often involves the removal of the graphene from its metal growth substrate, followed by transfer to a target substrate for device fabrication. This process involves exposing the graphene to both aqueous and atmospheric gas environments [103], resulting in the attachment of chemical groups to the graphene. These groups can dope the graphene and alter its electronic properties. This process is called unintentional doping, as it is a byproduct of the transfer process and exposure to the environment and the doping level is neither controlled nor it is the main focus of the process.

Oxygen molecules exhibit a variety of chemical reactions with aromatic molecules [104] and carbon nanotubes [105]. The adsorbed oxygen is a well-known hole dopant for carbon nanotubes. In a recent experiment O_2 trapped between graphene and a SiO_2 substrate induced hole-doping [96]. This doping effect can be enhanced in the presence of moisture. A common method for desorption of chemical groups, oxygen, and moisture from graphene exploits heat treatment. To this end, thermal annealing has been investigated extensively to eliminate contamination and alter the electronic properties of graphene [106]. Cheng et al. reported that annealing at high temperature ($T > 400^\circ C$) brings graphene in close contact with the SiO_2 substrate it was deposited on and induces increased coupling between them [89]. Thermal annealing has activated the ability of diatomic oxygen to accept charges from graphene. However, this method in-

duced a pronounced structural distortion due to the close coupling of graphene to the SiO₂ substrate [96]. Tailoring the electronic properties of graphene was performed through controlled heat treatment without degrading its structural properties. The basic cause of these changes is uncertain, and a systematic study to understand the mechanisms behind the interaction between graphene and the chemical groups bounded to its surface is still lacking and highly desired. Furthermore, the variation in mobility and charge carrier concentration in CVD-graphene depends on the donor or acceptor nature of the chemical. Therefore, a controlled environment for graphene doping provides the opportunity to further tailor the electronic structure by altering the concentration of different dopants.

1.4.2 Substitutional doping of graphene

The extremely high charge mobility of graphene suggests great potential to be exploited for applications in next-generation microelectronics. Control of the carrier density towards n- and p-type conductive channels is of importance in fabricating logic devices. The conventional ion implantation technique in silicon based FETs induces damage in the structure of graphene. In addition, graphene's zero bandgap raises difficulties for controlling electrical conductivity as compared to conventional semiconductors [6]. Substituting carbon atoms with foreign molecules showed that it is possible to open the bandgap and modulate the carrier types and concentration to make p- and n-type FETs [107, 108, 109]. In general, doping adjusts the work function of the graphene, which is necessary to control charge injection and collection in devices such as solar cells and light emitting devices. In addition, chemical doping can further increase the conductivity of graphene for transparent conductive electrode applications [28, 110]. Graphene can be readily p-doped through adsorbents from air like oxygen and moisture [96, 106, 111]. For n-doping, nitrogen is considered to be an excellent element for the chemical doping of carbon materials because it is of comparable atomic size and contains five valence electrons available to form strong valence bonds with carbon atoms. N-doped graphene has been created through chemical vapor deposition (CVD) using ammonia [107] and Pyridine [112] as nitrogen-doping sources, as shown schematically in Fig 1.19. In a typical CVD

growth, NH_3 (gas) is introduced into the flow as a nitrogen source. Nitrogen atoms substitutionally dope the graphene lattice when recombination of carbon atoms occurred in the CVD process.

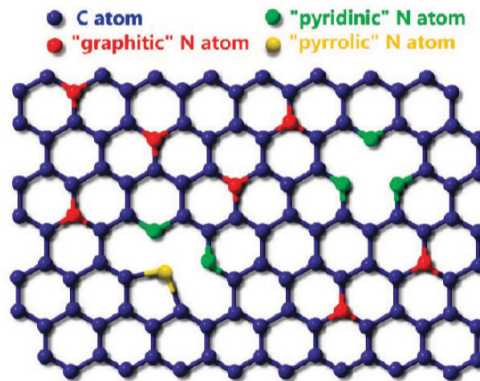


Figure 1.19: Schematic representation of the *n*-doped graphene. The blue, red, green and yellow spheres represent the C, "graphitic" N, "pyridinic" N, and "pyrrolic" N atoms in the *n*-doped graphene, respectively [107].

Furthermore, a segregation phenomenon was utilized to turn the trace amounts of carbon and nitrogen dissolved in bulk materials to synthesize nitrogen doped graphene [113]. However, these processes were performed at high temperatures to "drive-in" the dopants. Moreover, doping through chemical treatments is unstable, as physically adsorbed molecules will be desorbed under heat or vacuum [114, 115]. Therefore, a low-temperature, defect-free, and controllable method of doping of graphene is greatly needed.

1.5 Raman spectra of Graphene

Raman spectroscopy has long been used as a powerful tool to analyze carbon materials. This section is focused to understand the origin of the Raman bands of graphene and the analysis of defects and doping in graphene based on the Raman spectra.

Two prominent features are found in graphene Raman spectra: the G band and the 2D band (also called G'). Figure 1.20 displays the Raman spectra of perfect graphene (without defects). The D and D' bands are two additional features that are inactive in perfect

graphene, but they become active in the presence of defects. Figure 1.20 shows the Raman spectra of defective graphene where these two peaks can be explicitly identified.

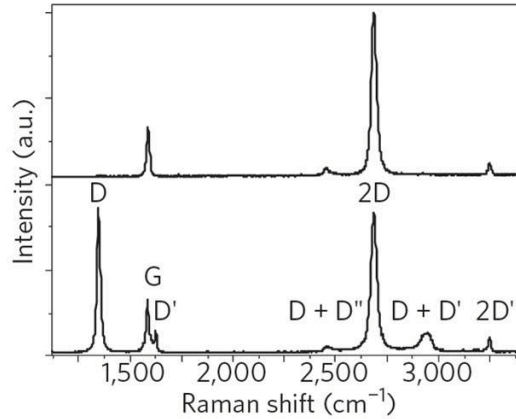


Figure 1.20: Raman spectra of perfect monolayer graphene (top) and defective monolayer graphene (bottom) [116].

Raman is an inelastic scattering of light, which can be originated from different interactions between the light and solids. In graphitic materials the inelastic scattering is mainly governed from electron-phonon interaction [117, 118, 119]. For this reason, it is important to analyze the phonon dispersion of those materials in order to analyze the Raman spectra [119, 120].

As previously reported, the unit cell of graphene is formed by two atoms. It results in six possible phonon dispersion branches: three optical and three acoustic.

For one acoustic branch (A) and one optic (O) phonon branch, the atomic vibrations are perpendicular to the graphene plane, and they correspond to the out-of-plane (o) phonon modes. For two acoustic and two optic phonon branches, the vibrations are in-plane (i). Furthermore, the phonon modes are classified as longitudinal (L) or transverse (T) according to whether the vibrations are parallel or perpendicular to the wave-propagating direction specified by the wave vector. The longitudinal acoustic (LA) and the longitudinal optical (LO) modes are always in-plane modes along with the iTA and iTO

modes, which are normal to the LA and LO modes. In addition, there are two out-of-plane modes denoted by oTA and oTO that are normal to the other four modes [121, 122]. Therefore, along the high-symmetry Γ - K or Γ - M directions, the six phonon dispersion curves are assigned to LO, iTO, oTO, LA, iTA, and oTA phonon modes (see Figure 1.21).

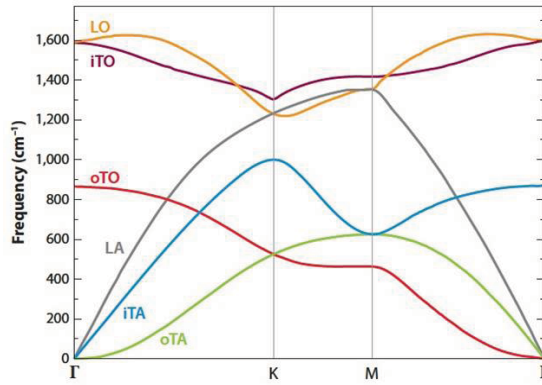


Figure 1.21: Phonon dispersion relation of graphene showing three acoustic (A) and three optic (O) phonon branches. Vibrations are in-plane (*i*) or out-of-plane (*o*) and longitudinal (*L*) or transverse (*T*) with respect to the direction Γ - K and Γ - M in the Brillouin zone [123].

From Fig. 1.21, it is possible to observe two degenerations: one for TO and LO branches at the Γ point, called E_{2g} symmetry mode from the group theory; and the second for TO branch at the K point, called the A'_1 symmetry mode. These degeneracies are called Kohn anomalies and they give rise to a strong interaction between electrons and phonons [124, 125]. Then, it is possible to define an electron-phonon coupling (EPC) at the E_{2g} and A'_1 symmetry points that are responsible for the main features of the Raman spectra of graphene. The E_{2g} point symmetry gives rise to the G band and it is due to the in-plane stretching of the carbon-carbon bonding [126, 127, 128] as shown in Fig. 1.22a.

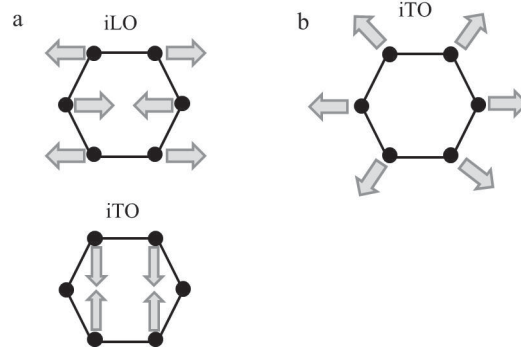


Figure 1.22: Atomic vibration modes at (a) E_{2g} symmetry point due to the degeneracy of in-plane trasverse and longitudinal phonons and at (b) the A_1' symmetry due to the in-plane transverse phonons.

The G band is the signature of all the sp^2 carbon allotropes (graphene, graphite, CNT, etc.). It is also the only first-order stokes Raman scattering process in graphene. A first-order stokes Raman process means that only one scattering process occurs and a schematic of this process is presented in Fig. 1.23a, showing the whole process in which the electrons are excited to the conduction band, and then a phonon with a very small momentum ($q \approx 0$) is emitted (G peak in the Raman spectra), and finally the electron-hole recombination process occurs.

For the A_1' point symmetry, the situation is quite different. Figure 1.22b shows the atomic displacement associated with this vibration mode, so called "breathing mode". Interestingly, this process is prohibited in perfect graphene, and the intensity is dependent on the amount of lattice defects. This mode causes the so-called D band. This D band is a second-order Raman process where the excited electrons are elastically scattered from K to K' , in the momentum space, then the electron is scattered back inelastically, emitting a phonon of momentum q ($q \neq 0$), and finally the recombination process occurs, as shown in Fig. 1.23b. This is a inter-valley process, because the electron scattering takes place between the two cones in the momentum space (K and K'). Similarly to the D band, D' is the result of an elastic (defect) and an inelastic scattering but takes place in the same cone (Fig. 1.23c) and is called intra-valley process.

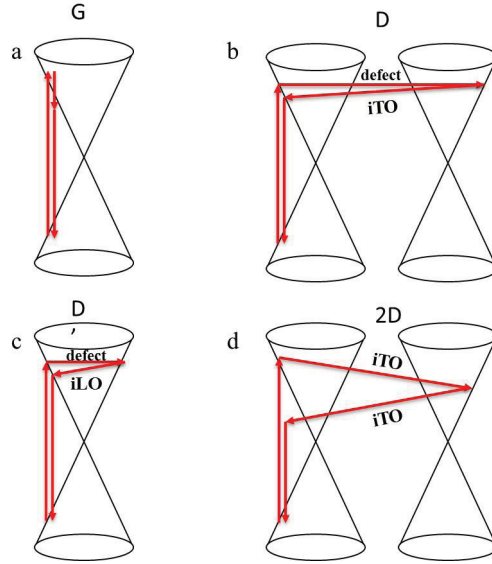


Figure 1.23: Raman process for (a) G, (b) D, (c) D', and (d) 2D bands.

Finally, the 2D band is the most intense of the bands present in graphene. It is also an inter-valley process as D, but the excited electrons are inelastically scattered from K to K', emitting a phonon of momentum q and then inelastically scattered back to K by a phonon of momentum $-q$ for momentum conservation. The process is plotted in Fig. 1.23d. The Raman shift of 2D band is approximately two times that of D band. For that reason, the 2D band is considered as the overtone of the D band. It is important to note that the high intensity of 2D band is part of the signature for perfect graphene. The 2D loses intensity with the presence of defects, inversely proportional to the intensity of the D band. This characteristic band has been used also to identify the monolayer nature of the graphene film [22, 129].

1.5.1 Number of Layers and Orientation

The shape of the 2D peak can be used to determine the number of graphene layers (up to ~ 5 layers) in few layer graphene samples [129]. Above 5 layers the 2D lineshape becomes indistinguishable from graphite. The change in electronic band structure when moving from single layer graphene to several layers causes a change in 2D

peak shape and intensity [129]. Figure 1.24 shows the evolution of the 2D peak with number of layers for several excitation energies.

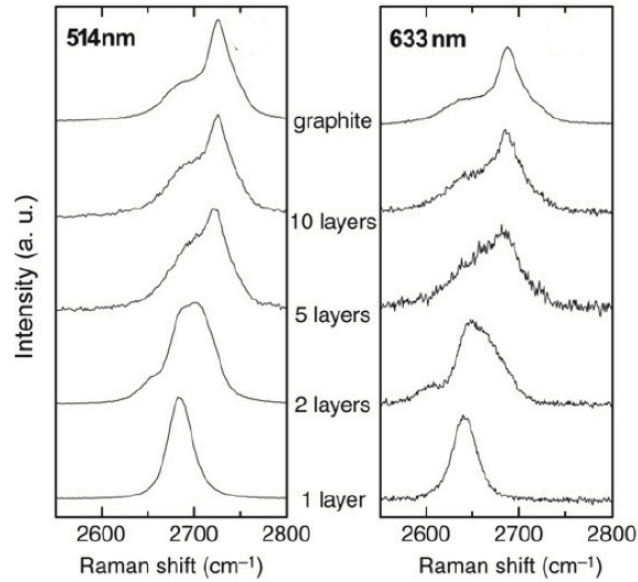


Figure 1.24: Evolution of the 2D peak for an increasing number of graphene layers. The 2D peak of the Raman spectra evolves from single peak in mono layer towards the structure seen in graphite. The measurements were performed with 514nm and 633nm laser light [129].

Figure 1.25 shows the four different Raman processes associated to the 2D band that are possible for bilayer graphene with its double band structure.

This leads to a combination of four peaks, from each of the double resonant Raman processes, used to fit to the measured 2D peak in bilayer graphene. The 2D lineshape continues to change as layers are added and the electronic band structure continues to change, eventually tending to that of graphite.

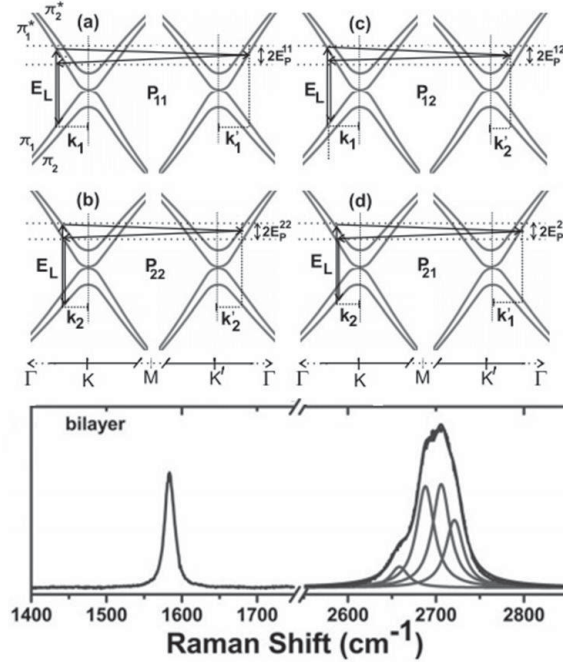


Figure 1.25: The 2D Raman processes in bilayer graphene. (Top) Schematic view of the electron dispersion of bilayer graphene near the K and K' point showing both π_1 and π_2 bands. The four double-resonance (DR) process are indicated: (a) process P_{11} , (b) process P_{22} , (c) process P_{12} , and (d) process P_{21} . The wave vectors of the electrons (k_1, k_2, k'_1, k'_2) involved in each of these four DR processes are also indicated. (Bottom) Raman spectrum of the bilayer graphene performed with the 2.41 eV laser line [130].

The single linear band in mono layer graphene means there is only one 2D process available which produces a single Lorentzian 2D peak. Additionally for the case of 1L graphene the process is triple resonant and leads to a 2D peak that is significantly more intense than the G peak [121], this feature makes Raman spectroscopy particularly useful for identifying mono layer graphene. The 2D peak features outlined are valid when the graphene layers are Bernal AB stacked. For turbostratic graphite (unordered stacking) the difference in band structure leads to a single 2D peak but with FWHM almost double that of graphene and is upshifted by $\sim 20 \text{ cm}^{-1}$ [131].

There are other peaks besides the 2D peak that can be used to

study the number of layers in graphene samples. A mode related to the shearing of the graphene sheets on top of one another leading to a so called C-peak has been observed at $\sim 42 \text{ cm}^{-1}$ [132]. The intensity of this C peak scales directly with layer number and is not present in single layer (as seen in Fig. 1.26).

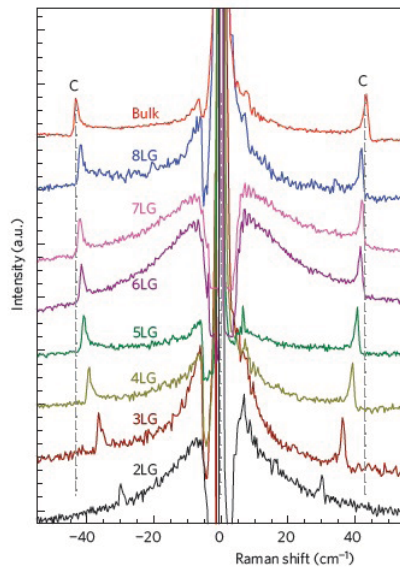


Figure 1.26: Stokes and Anti-Stokes Raman spectra for the C peak spectral region [132].

The peak is of limited practical use since the position is of such low frequency that it is usually below the notch filter that protects the measurement equipment from the intense Rayleigh scattered light.

1.5.2 The effects of Doping

The primary effect of electron or hole doping on the Raman spectrum of graphene is to move the G peak position due to stiffening or softening of the phonon modes [133, 134]. As a result the G peak upshifts in wavenumber for p-type doping and downshifts for n-type doping. However for low levels of doping, below $\sim 3 \times 10^{13} \text{ cm}^{-2}$, a modification of phonon dispersion near the Kohn anomaly causes the G peak to upshift for both p and n type doping [133, 134], but the G peak position in n type doping returns to downshifting at higher levels

of doping. The change in G peak position by doping has been observed for electronically gated bilayer [134] and single layer graphene [133]. Figure 1.27 (a) and (b) shows the change in G peak observed as doping in graphene is increased (via a back-gate). It is possible to estimate the charge carrier concentration in other samples by measuring the G peak position and comparing to plots such as Fig. 1.27.

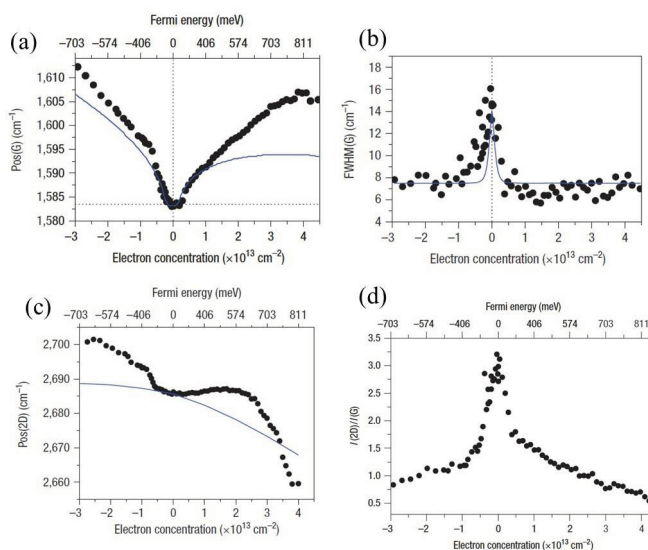


Figure 1.27: Raman measurement of monolayer graphene with a voltage applied to the back gate to control the electron concentration [133]. (a) (b) Position and full width at half maximum (FWHM) variations of the G peak with electron concentration. (c) Position changes of the 2D peak with electron concentration. (d) Changes of the intensities ratio of the 2D and G bands (I_{2D}/I_G) with electron concentration. The solid lines are predicted non-adiabatic trends [135].

However, it is necessary to determine if the charge doping is due to holes or electrons. This cannot be done by the only observation of G peak shift. Das et al. [133] observed a dependence of 2D peak shift on the character of the doping. As seen in Fig. 1.27(c) and as shown in Fig. 1.28, a plot of the Raman spectra of G (left) and 2D (right) bands at different values of the top-gate voltage, and as a consequence of electron concentration, (axis) can be used to evaluate the doping.

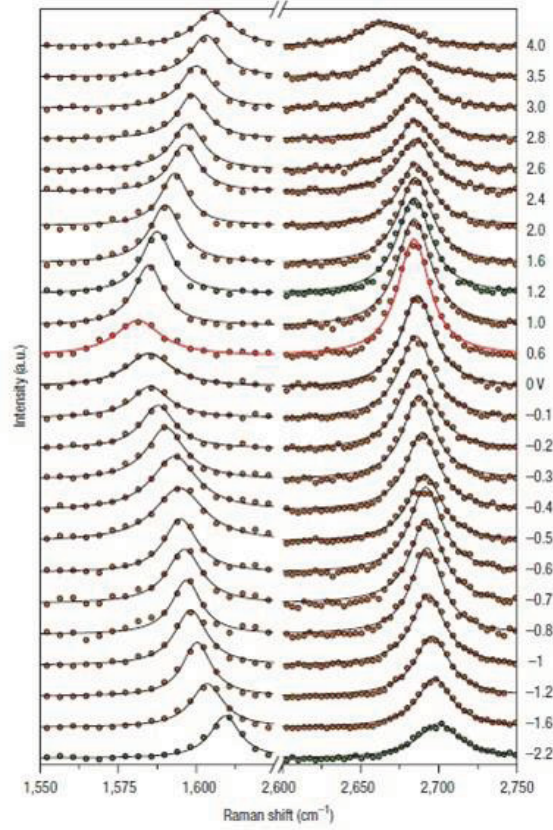


Figure 1.28: *G* and 2*D* frequency shift as a function electron concentration [133].

Based on the specific geometry the amount of induced charges into the graphene sheet was given by:

$$V_{TG} = 1.16 \times 10^{-7} \sqrt{n} + 0.723 \times 10^{-13} n \quad (1.23)$$

where n stands for the electron concentration in cm^{-2} and V_{TG} for the applied top gate voltage in Volts. The 2*D* peak shifts to lower frequencies under a high electron concentration (n-doping); and it shifts to higher frequencies under high hole concentration (p-doping).

Doping modifies, also, the 2*D* peak intensity due to the interactions with electrons in a double resonant process requiring real electronic states (as shown in Fig 1.27(d)) [121].

1.5.3 The effects of Strain

Raman measurements have shown that graphene placed under strain exhibits a change in G peak [136, 137]. Placing graphene under tensile strain usually softens vibrational modes, and the opposite occurs for compressive strain [116]. G peak position shifts of up to 14.2 cm^{-1} for 1% of strain have been observed [136]. Furthermore the G peak was split into two peaks [137, 138] due to components of the E_{2g} mode being parallel or perpendicular to the applied strain. When analysing the G peak care must be taken to distinguish between strain and doping, both of which can affect its position. Small amounts of strain can be caused by corrugations in a graphene sheet [139], however it is placing graphene on a flexible substrate and applying pressure that introduces significant levels of strain required for the G peak to split into two components [136, 137].

Until today there are several works in the literature with the description of experiments made on samples of Gr with the aim of highlighting the effects of strain [140, 141, 142] and distinguish these from the effects obtained by doping achieved with thermal treatment in a controlled atmosphere [98]. In particular Lee et al. [140] and Verhagen et al. [98] have recently shown that the strain and doping contributions can be distinguished from each other with a correlation analysis of the two dominant modes in the Raman spectrum of Gr, the G and 2D bands. These studies considered a correlation map between the positions of the two bands, so that each point on the graph is described as a linear combination of the vector strain and that of doping. Raman spectroscopy studies on samples of Gr undoped have shown that applying a strain effect there is an increase or decrease of the G and 2D bands position. Inserting in a graph the position of the 2D band as a function of the position of the G band it is found that the data fall on a straight line (called "Strain line"), which has a slope of 2.45 [142]. When the value of strain is kept constant, but varies the doping level, the same effect can be observed, but the data adapt to a straight line with a slope of 0.7 named "doping line" [133]. Furthermore the origin of the coordinate system corresponds to the position of the Raman bands of a sheet of graphene freestanding, which does not present strain and doping. The point of the map origin for a 2.33 eV excitation source is approximately equivalent to

(1582 cm^{-1} ; 2670 cm^{-1}). In Figure 1.29 it is shown an example of the correlation obtained by Verhagen et al. as a function of the temperature of a sample of graphene on a SiO_2/Si substrate. This map can be used to evaluate the level of strain or of doping in a sample of graphene after opportune treatment.

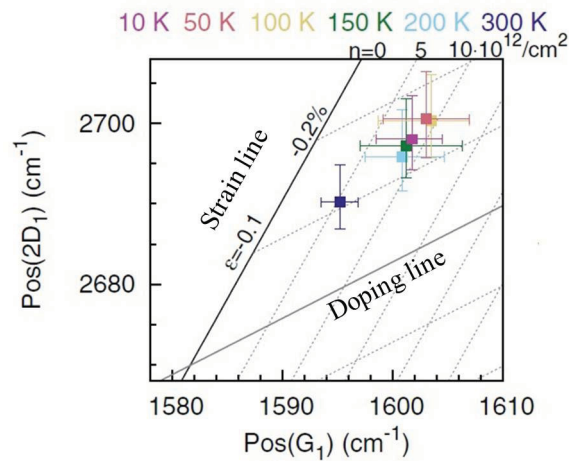


Figure 1.29: Temperature dependence of the correlation between the Raman shift of the G band ($\text{Pos}(G_1)$) and 2D band ($\text{Pos}(2D_1)$) of the spectra of monolayer of Gr. The solid black line indicates pure strain (ϵ) variation, with a slope of 2.45, and the solid gray line indicates pure doping (n) variation, with a slope of 0.7. Adapted to [98].

Chapter 2

Molybdenum disulfide



2.1 Physical properties

With the discovery and characterization of Gr in 2004, which has created great interest in last years, it became natural to explore the synthesis of Gr analogues of layered materials such as the transition metal dichalcogenides (TMDCs). The TMDCs, are two-dimensional semiconductors in which the atoms within the layer are held together by strong covalent forces while Van der Waals interaction enables stacking of the layers. The TMDCs are compounds of the type MX_2 , with M a transition metal atom (Mo, W, etc.) and X a chalcogen atom (S, Se, or Te.), in particular one layer of M atoms is sandwiched between two layers of X atoms [143].

Monolayers of MoX_2 compounds ($X = S, Se, \text{ and } Te$) are typically composed of Mo atoms sandwiched between X atoms, organized in a 2D hexagonal honeycomb structure (Figure 2.1(a)). Common polytypes of MoX_2 compounds are hexagonal 2H- MoX_2 and rhombohedral 3R- MoX_2 that are different in vertical stacking alignment [144, 145]. 2H- MoX_2 is composed of monolayers that are vertically stacked in ABAB sequence, while 3R- MoX_2 is composed by ABCABC sequence (Figure 2.1(b)) [143, 145]. However, 2H- MoX_2 is the naturally occurring and relatively stable polytype observed for MoX_2 compounds,

while 3R- MoX_2 is generally transformed into the 2H- MoX_2 upon heating [143].

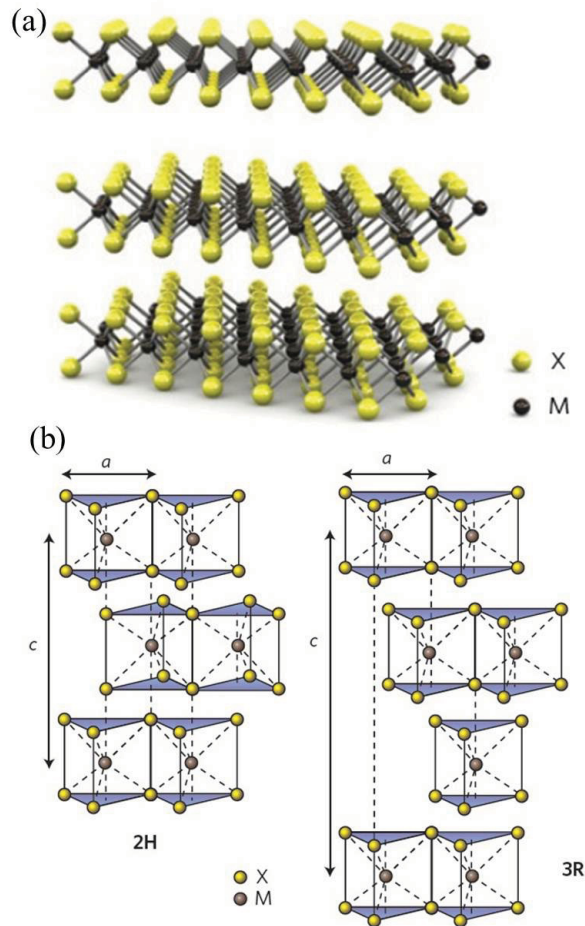


Figure 2.1: (a) Three-dimensional schematic representation of a typical MX_2 structure, with the chalcogen atoms (X) in yellow and the metal atoms (M) in grey. (b) Schematics of the structural polytypes: 2H (hexagonal symmetry, two layers per repeat unit, trigonal prismatic coordination), 3R (rhombohedral symmetry, three layers per repeat unit, trigonal prismatic coordination). The chalcogen atoms (X) are yellow and the metal atoms (M) are grey. [143].

The lattice parameters of the layered 2H- MoX_2 compounds are presented in Table 2.1. In bulk form 2H- MoX_2 compounds are indirect

bandgap materials with bandgap values of <1.3 eV as presented in Table 2.1. When the crystal thicknesses are reduced down to one layer, the bandgaps widen. Interestingly, they transform from indirect to direct bandgaps in this transition.

		MoS ₂	MoSe ₂	MoTe ₂
Lattice constants (Å) [146]	a	3.160	3.288	3.517
	c	6.147	6.460	6.981
	c/a	1.945	1.962	1.984
Interlayer height (Å)	$X-M$	3.19	3.23	3.63
Van der Waals gap (Å)	$X-X$	3.47	3.75	3.92
Bandgap energy (eV) [11]	<i>Bulk</i>	1.29	1.1	1.0
	<i>Monolayer</i>	1.89	1.58	1.23
Raman active modes (cm ⁻¹) [146, 147]	A_{1g}	409	243	171
	E_{2g}^1	383	283	232.4
	E_{1g}	287	168.8	116.8
Thermal conductivity (Wm ⁻¹ K ⁻¹)	k	18.06	2.3	2

Table 2.1: Properties of 2H-MoX₂ compounds.

Kumar et al. have conducted first principles calculations of the electronic structure of both bulk and monolayers of MoX₂ compounds, which are presented in Figure 2.2 [148]. These calculations generally show that the density of states around the Fermi level is mainly due to the molybdenum d states [148]. The calculations also show a strong hybridization between molybdenum d states and chalcogen p states below the Fermi level. Furthermore, it is demonstrated that the transition of the band structure from indirect to direct bandgap, when reducing the sheet thickness from bulk to monolayer, is due to changes in hybridization [149]. The transition from indirect to direct bandgap has also been experimentally demonstrated via photoluminescence studies of mono- and multilayered MoX₂ [149, 150, 151].

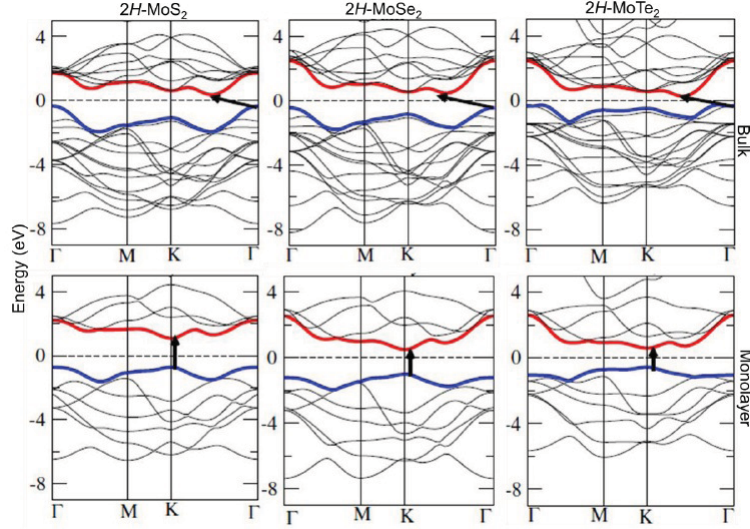


Figure 2.2: Band structures of bulk and monolayer MoX_2 compounds obtained using DFT calculations [148].

Similar to graphene, band structures of multilayered MoX_2 can be manipulated via various physical and chemical methods. Ramasubramanian et al. have demonstrated through DFT calculations, the tunability of the bandgap in bilayered 2H- MoX_2 using external perpendicular electric fields (bandgap values decrease with increasing electric field) [152]. At electric fields above 3 Vnm^{-1} , the structure shifts to become metallic in all MoX_2 compounds.

The tunability of the bandgap by reducing the number of layers, or alternatively the application of external electric fields, presents the possibility for a wide range of applications for layered MoX_2 compounds in the field of optoelectronics. It is worth to note in this context that there are also recent reports on the chemical intercalation of MoS_2 using ions such as Li^+ to reduce the bandgap [153].

2.1.1 Electronic properties

In developing a field effect transistor (FET), several properties of the semiconducting materials are of greatest importance: (a) the bandgap value that governs transistor switching, (b) charge density that describes the number of available free charges in the channel, and

(c) carrier mobility which rules the switching speed.

The main advantage of 2D transition metal dichalcogenides (TMDCs) over graphene is the presence of natural bandgaps, which allow the fabrication of FETs with very low OFF currents and high ON/OFF current ratios. The bandgap values of TMDCs are similar to those of Si (in the case of bulk materials) or even higher in the case of the monolayer (as is visible in the table 2.1). In monolayers of MoX_2 , even though the bandgap increases, it is still within the viable range.

The magnitude of charge density is also a vital factor for developing FETs. At room temperature, many intrinsic semiconductors have relatively low charge densities that are not sufficient for generating enough output current in FETs. Doping and intercalation procedures are routinely implemented to increase the desired charge density.

For the fabrication of FETs, enhanced charge carrier mobility in the semiconducting material is essential. In 2D TMDCs, the charge carriers are confined within the layer that can potentially offer increased mobility. However, this carrier mobility in the 2D materials is also influenced and reduced by various charge scattering effects such as: (a) Coulombic, (b) optical phonons, (c) acoustic phonons and (d) surface roughness [154].

Coulomb scattering: Coulombic scattering is caused by random charge impurities located within or on the surface of the 2D layer. The scattering from these charged centers in the electric quantum limit was first formulated by Stern and Howard in late 1960s [155]. As mentioned in the previous section in TMDCs, Coulombic charges, such as the ionic intercalants, can be used in order to control the size of the energy bandgap. This increases the charge densities, which is also desirable. However, the process also leads to increased Coulombic scattering effects, potentially reducing the carrier mobility.

Polar optical phonon scattering: In compound semiconductors, where the bonding is partially ionic, a polarization field arises [154]. The polarization field, forced into effect by the longitudinal-optical mode, causes a polar-optical interaction with the electrons, which scatters them and subsequently decreases their mobility.

Acoustic phonon scattering: Acoustic phonons operate via the generation of deformation potentials, which interact with charge carriers. These phonons produce crystal lattice deformations, which in turn produce localized electric potential affecting such carriers.

Surface roughness scattering: The influence of the surface or interface roughness on the mobility of 2D electrons has never been precisely assessed since the roughness behaviour is never quite clear. For calculations, generally the surface fluctuations are assumed to be randomly correlated spatially, with a correlation that follows a Gaussian distribution [156]. In this case, two perturbation parameters influence the scattering mechanism: the random fluctuations in thickness and the correlation length (or average distance) between two roughness centers. Minimizing these parameters with perfect lattice matching between the 2D TMDCs and their substrates have been suggested as possible methods to reduce the roughness scattering effect.

The carrier mobility in a thin layer is calculated using:

$$\mu = \frac{e}{m^*} \langle \tau \rangle \quad (2.1)$$

in which e is the point charge and τ is the transport relaxation rate of momentum in the (x, y) plane and m^* is the effective electron mass. Using the Born approximation, the transport relaxation time is calculated as [154]:

$$\frac{1}{\tau(E_k)} = \frac{2\pi}{\hbar} \sum_{k_z} \sum_{\mu} \int_{-\infty}^{\infty} N_i^{(\mu)}(z) dz |V_{k-k_z}^{(\mu)}(z)|^2 \times \\ \times (1 - \cos\theta_{kk_z}) \times \delta(E(k) - E(k_z)) \quad (2.2)$$

in which $N_i^{(\mu)}(z)$ is the concentration of the μ^{th} kind of charge center within the volume of $dx dy dz$ and θ_{kk_z} is the angle between k and k_z vectors. In addition, $V_{k-k_z}^{(\mu)}(z)$ is an important parameter that shows the intensity of scattering and is described as the matrix element of the scattering potential. It is a potential function that describes the intensity of the scattering effect on free carriers. By correctly estimating the scattering potential, the transport relaxation rate and

the associated mobility can be calculated. The overall carrier mobility can then be obtained using Mattheissens Rule [154]:

$$\frac{1}{\mu_{TOTAL}} = \frac{1}{\mu_C} + \frac{1}{\mu_{PO}} + \frac{1}{\mu_A} + \frac{1}{\mu_{SR}} \quad (2.3)$$

where μ_{TOTAL} is the overall mobility and μ_C , μ_{PO} , μ_A , μ_{SR} are the effective carrier mobilities limited by Coulombic, polar optical phonon, acoustic phonon and surface roughness scattering mechanisms, respectively.

Generally, Coulombic scattering is the dominant effect in reducing the overall charge carrier mobility at room temperature or below, for 2D materials such as graphene or MoS₂ [157]. According to Equation 2.2, to tackle this, an increase in the dielectric constant is needed. The increase in the dielectric constant (electrical permittivity) of either the surrounding environment or the 2D material reduces the Coulombic effect as it confines the electric field generated by the Coulombic charges within smaller regions; hence, to reduce the effect on mobile charge carriers, dielectric constant (κ) engineering has proven to be effective in enhancing the charge carrier mobility [157, 158]. In the case of MoS₂ ($\kappa \sim 5$), the theoretical carrier mobility is still dominated by Coulombic scattering at room temperature, and the mobilities agree with the commonly observed experimental values [157, 159].

Despite single layers of MoS₂ have a large intrinsic bandgap of 1.9 eV previously reported mobilities in the 0.53 cm²V⁻¹s⁻¹ range are too low for practical devices [22]. Radisavljevic et al. have fabricated a transistor from single-layer of MoS₂, obtained by mechanical exfoliation and transferred on a doped silicon substrate covered with a thickness of 270nm of SiO₂ [157]. The device made with a single layer of MoS₂ shows a typical value of mobility in the range 0.1-10 cm²V⁻¹s⁻¹. This value is lower than that obtained for the bulk of MoS₂ at room temperature, which has a mobility value in the range 200-500 cm²V⁻¹s⁻¹ [160]. Radisavljevic et al. have, therefore, deposited with atomic layer deposition (ALD), a layer of high- κ dielectric (30nm HfO₂) to increase mobility of the device and obtain the best potential from the single layer of MoS₂. In this way they have shown that a single layer of MoS₂ at room temperature can obtain mobility values of at least 200 cm²V⁻¹s⁻¹, demonstrating the potentialities for the realization of transistors with room-temperature

current on/off ratios of 1×10^8 and ultralow standby power dissipation [157].

2.1.2 Optical properties

Many 2D materials offer extraordinary optical properties that may be layer dependent. As mentioned previously, for MoX_2 the bandgap changes from indirect to direct, when the thickness is reduced to only one layer. As such, monolayer MoX_2 exhibits strong fluorescence.

Similar to graphene, the Raman spectra of TMDCs are also layer dependent, which also show strong changes of vibrational photospectroscopy upon intercalation and doping.

Figure 2.3(a) illustrates the Raman active modes for all the MoX_2 compounds (peak value details presented in Table 2.1). The A_{1g} , E_{1g} and E_{2g} correspond to the Raman active modes [146, 147]. Out of those, E_{2g} is a low frequency rigid layer mode, which reflects the van der Waals binding forces between planes. By reducing the thickness of MoS_2 to a monolayer, Raman peak shifts appear in comparison to its bulk counterpart (Figure 2.3(b)). The shifts are observed in the two major modes of MoS_2 , E_{2g}^1 and A_{1g} . For the E_{2g}^1 mode, the vibrations of both Mo and S atoms are limited to the horizontal plane, whereas for the A_{1g} mode, the displacements of S atoms are along the vertical plane. For monolayers of MoS_2 , the Raman peak shifts associated with E_{2g}^1 and A_{1g} modes are observed at 387 and 403 cm^{-1} , respectively [161, 162]. Along with an increase in the number of layers, the frequency of the A_{1g} mode is observed to increase, whereas the E_{2g}^1 mode is observed to decrease in frequency [161, 162, 163]. This indicates stiffening of the A_{1g} mode, which is expected with an increase in the number of layers, causing increased Van der Waals forces, which in turn suppresses the atomic vibrations along the vertical plane [161, 162]. Above five layers, both vibrational modes seem to converge to their bulk values [161, 162, 163]. Such thickness dependent Raman peak shifts offer an effective method for identifying the number of layers.

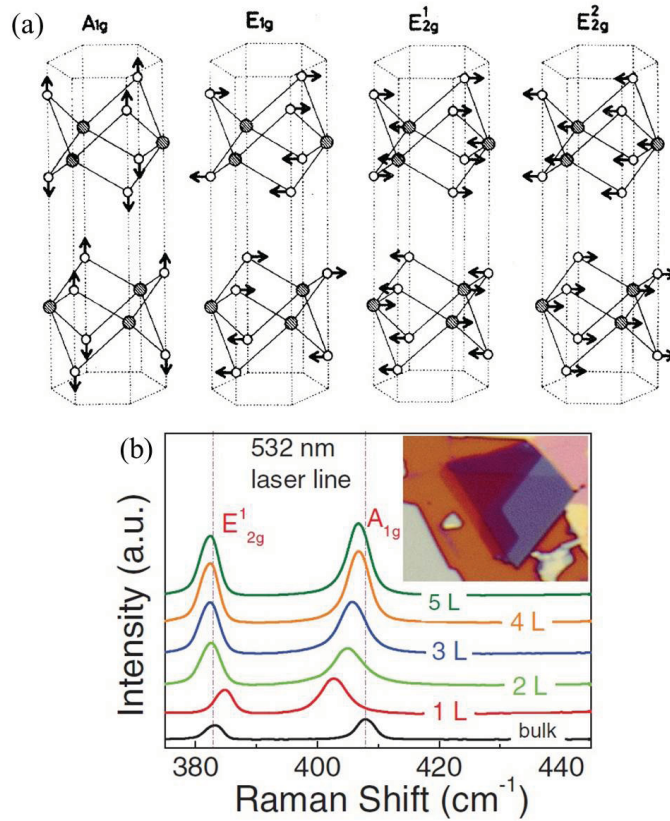


Figure 2.3: (a) Raman active modes of 2H-MoX₂ compounds. Dark shaded circles represent Mo atoms and the light circles represent chalcogen atoms [146]. (b) Raman spectra of MoS₂: from bulk to mono layers, with the laser wavelength of 532nm [162].

Monolayers of MoS₂ exhibit a significant increase in photoluminescence (PL) in comparison to their bulk structure, owing to the change in band structure from indirect to direct bandgap [149, 150, 151]. Figure 2.4(a) illustrates the PL spectra of mono- and bi-layer flakes with the inset showing the apparent reduction in quantum yield with an increasing number of layers. Figure 2.4(b) shows the optical images of mono- and multi-layer flakes on a silicon substrate and its corresponding PL images. It should be noted that the enhanced PL emission from the monolayer is visible and the emission from the multilayer is too weak to be observable in the PL image [151].

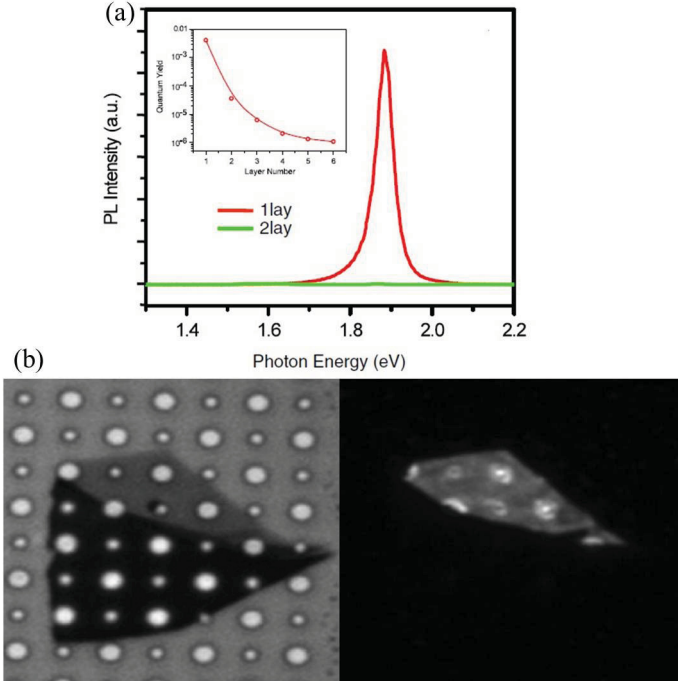


Figure 2.4: (a) PL spectra of a mono and bilayer MoS_2 flake with inset showing the change of quantum yield with increasing number of layers [149]. (b) Optical image of a mono and multilayer MoS_2 flake on silicon substrate with etched holes of 1 and 1.5 μm in diameter and its corresponding PL [149].

2.1.3 Thermal properties

Thermal conductivity of layered materials is directionally oriented. It has been shown that for MoS_2 , the thermal conductivity along the plane is $18.06 \text{ Wm}^{-1}\text{K}^{-1}$. Interestingly, this thermal conductivity drops to only $4.17 \text{ Wm}^{-1}\text{K}^{-1}$ for the out of plane direction [164]. Obviously, exfoliation and restacking of the layers reduce this thermal conductivity as they cause lattice mismatch, which promotes phonon scattering [165]. The relatively low thermal conductivity of the exfoliated MoX_2 group (Table 2.1), make these materials excellent candidates for thermally insulating solid lubricants. The changes in the thermal conductivity of MoS_2 and $MoSe_2$ with temperature are shown in Figure 2.5. As can be seen, they all decrease with increasing tem-

perature, which can be associated with the lattice vibrations at higher temperatures.

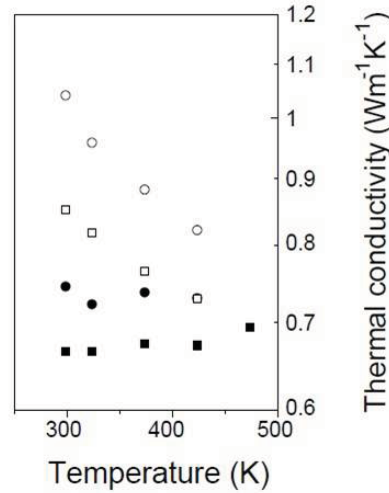


Figure 2.5: Thermal conductivities of MoS₂ and MoSe₂. MoS₂ (circle), and MoSe₂ (rectangle). Solid symbols indicate exfoliated and restacked compounds while open symbols indicate the pristine material [165].

2.1.4 Mechanical properties

In addition to the exciting electronic and optical properties that 2D TMDCs possess, understanding their mechanical properties is also of significant importance in the development of flexible mechanical devices and actuators. Bertolazzi et al. have demonstrated the strength and elasticity of suspended monolayers of MoS₂ to be comparable to that of stainless steel [166]. Gomez et al. have shown their ability to withstand elastic deformations up to tens of nanometers without breaking [167]. The average Young's modulus of suspended MoS₂ nanosheets are observed to be 270-330 GPa (in comparison to 180 and 1000 GPa for stainless steel and graphene, respectively) [166, 167]. Interestingly, MoS₂ monolayers show a transition in electronic properties from semiconducting to metal in the presence of mechanical strain [168, 169]. They change from direct to indirect bandgaps at small tensile strain (<2%) and shift into the metallic regime, before reaching the set tensile strength [169].

2.2 Applications

Electronic devices. MoX_2 have been favorite candidates in the fabrication of electronic components, especially FETs. The 2D TMDCs, just thanks to the manipulation of the electronic properties through, for example, doping and other approaches, with the ability to create both Schottky and ohmic contacts, are favorable materials for the electronics industry.

One of the first reports on 2D MoS_2 is Novoselov et al. work on measuring room temperature carrier mobilities on the order of 0.5 to 3 $cm^2V^{-1}s^{-1}$ [5]. More recently, Radisavljevic et al. demonstrated enhanced charge carrier mobility reaching values as large as $\sim 220 cm^2V^{-1}s^{-1}$ for monolayered MoS_2 , comparable to the values achieved in doped silicon thin films and graphene nanoribbons [157]. The use of a 30 nm thick HfO_2 layer as a high- κ dielectric top gate (Figure 2.6(a) and (b)) was the reason for such an increase as was comprehensively discussed in Section 2.1.1.

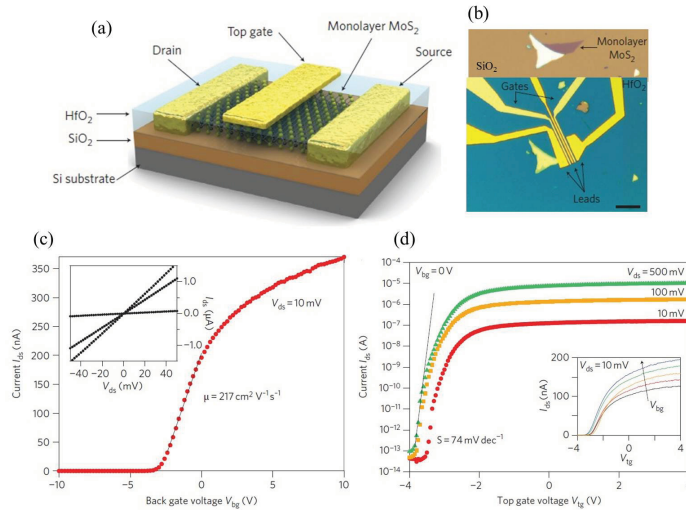


Figure 2.6: (a) 3D Schematic illustration and (b) optical microscope images of a monolayer MoS_2 FET. (c) The room temperature transfer characteristics of the FET, with inset showing drain-source current (I_{DS}) vs drain-source voltage (V_{DS}) curves for Back gate voltage (V_{GS}) values 0; 1, and 5 V. (d) The I_{DS} - V_{TG} curves recorded for a bias voltage ranging from 10 to 500 mV, showing ON/OFF ratios $> 10^6$ [157].

The field effect characteristics of this monolayered MoS₂ transistor, obtained at different gate voltages are shown in Figure 2.6(c) and (d). Remarkable drain-source current I_{ON}/I_{OFF} ratios of 10^6 and 10^8 for bias voltages of 10 mV and 500 mV, and OFF-state currents smaller than 100 fA indicate the high performance of the device.

Such monolayer transistors connected in series have been further developed into simple logic operators, signal amplifiers and even more complicated integrated circuits such as static random access memory (SRAM) and five-stage ring oscillators [170, 171, 172]. Furthermore, substrate and gate dielectric engineering have also been proven to result in significant enhancement of carrier mobilities in multilayer MoS₂ [159, 173]. The main issue with MoX₂ based FETs is the intrinsic theoretical limitation of the carrier mobility in such materials that remains under $500 \text{ cm}^2\text{V}^{-1}\text{s}^{-1}$; this still cannot quite rival that of silicon [157, 159]. However in a recent report, Das et al. have shown that eliminating the contact resistance effects through a novel selection of source/drain contacts can result in dramatic enhancement in carrier mobilities ($700 \text{ cm}^2\text{V}^{-1}\text{s}^{-1}$) in thin layers of MoS₂ [174]. FETs incorporating ultrathin MoSe₂ layer, with mobilities of $50 \text{ cm}^2\text{V}^{-1}\text{s}^{-1}$ and ON/OFF ratios $> 10^6$ have been recently realized [175]. In addition to FET structures, Spah et al. have reported heterojunction diodes achieved through Van der Waals epitaxial growth of a n-MoSe₂ on other p-type transition metal chalcogenides (WSe₂) [176]. These structures have proven to be effective in diode applications since they present excellent lattice matching. Another new application of MoS₂ has recently appeared in valleytronics, which involves channeling charge carriers into and out of valleys of set momentums [177, 178]. The crystal structure of MoS₂ creates two momentum valleys that are not symmetric. By using polarized light, it is possible to nudge carriers preferentially into one valley state or another. Due to their fast response, such interactions can be used in super high rate electronic and optical switches.

The relative abundance of TMDCs in nature, their high stability, and the ease of property manipulations, render 2D TMDCs one of the most promising building blocks for future electronic systems.

Battery electrodes. The electrochemical properties of layered MoX_2 structures as electrodes for lithium ion batteries have also been of growing research interest. Once again the lamellar structure of MoX_2 aids in alkali ion insertion in between the inter-layer and intra-layer spaces of these crystals. Obviously, the large inter-planar space in an MoX_2 lattice would be favorable to fast lithium intercalation and high lithium storage capacity [179]. 2D MoS_2 obtained from exfoliation and restacking, [179, 180] as well as solvothermal synthesis routes have been reported as electrodes for lithium ion batteries [181]. One of the major issues faced in the use of intrinsic layered MoX_2 in lithium ion batteries is the lack of cycling stability and rate capability limitations due to their proneness to very compact aggregation after repetitive cycles as well as the formation of gel-like polymeric layers due to electrochemically driven electrolyte degradation [182, 183, 184]. Recently Chang et al. have demonstrated high reversible capacities and cycling stability in MoS_2 /carbon-based (amorphous carbon and graphene) hydrothermally developed composites with uniformly dispersed 2D MoS_2 [183]. Mono- and multi-layered MoS_2 /graphene composites were reported to have specific capacities as high as 1100 mAhg^{-1} as well as excellent cycling stability [182, 185]. MoS_2 /reduced graphene oxide and mesoporous carbon composites have also been established as battery electrodes [184, 186]. Furthermore there are also reports on the application of MoS_2 electrodes in Mg ion batteries [187]. In addition to MoS_2 , other 2D MoX_2 compounds have also been used in lithium ion batteries. Morales et al. have successfully demonstrated the use of polycrystalline 2H- $MoSe_2$ as a cathode material in both lithium and sodium cells [188].

Catalysts. Layered TMDCs have been widely used in catalysis in their pristine forms as well as doped and composite forms [189, 190]. MoS_2 nanostructures have been commonly used as catalysts in catalytic reactions such as hydrodesulphurization (HDS) and more recently for hydrogen evolution reactions (HERs) [191, 192]. The catalytic activity is generally attributed to the unsaturated sites at the particle edge surfaces, parallel to the hexagonal axis of lamellar MoS_2 structures [193, 194]. For HERs, a systematic investigation of surface sites of MoS_2 nanoparticles on Au substrate (111) has revealed that

hydrogen evolution correlates linearly with the number of edge sites on the MoS₂ catalyst [192]. Hence, the key factors for optimization of the HER activity in MoS₂ are: increasing the catalytic activity of the active sites, enhancing the number of active sites (MoS₂ layer edges, therefore the applications of structures such as nanoribbons are advised) and increasing the electrical contact to the active sites (which is provided by the planar routes for electrons within the 2D structure). The integration of layered MoX₂ with the morphologically compatible graphene has also shown promise in increasing the catalytic activity. Li et al. have demonstrated that few layered MoS₂ structures synthesized on graphene sheets show enhanced electrocatalytic activity in HERs which has been attributed to the abundance of exposed MoS₂ edges on graphene and their excellent electrical coupling [195].

Optical devices. Layered MoX₂ are possible candidates for developing different types of optical devices, including solar cells based on photoelectrochemical, junction and organic technologies, semiconducting optical devices such as photo- and light emitting diodes. MoX₂ are used in photoelectrochemical solar cells, due to their inherent resistive nature to photocorrosion and energy bandgaps comparable to that of silicon that covers a large solar spectrum [196]. A good example is the work by Pathak et al. who developed MoSe₂ based photoelectrochemical cells by dipping the semiconductor electrodes in an ionic electrolyte forming a Schottky interface around which the photo generated electrons are harvested [197]. The efficiency of such photoelectrochemical solar cells is still much lower than ideal. The best electrode structures are those consisting of large surface areas with paths of minimum charge carrier scattering to increase the efficiency. Obviously, the best candidates will be vertically oriented planes of MoX₂, which are still challenging to create.

MoS₂ has also been incorporated as counter electrode catalysts in dye-sensitized solar cells. Significant conversion efficiencies of up to 7.59% have been observed similar to that of dye-sensitized solar cells with Pt counter electrodes [198]. Composite structures such as MoS₂ - carbon/carbon nanotubes, MoS₂ - graphene nanosheets have also been established as Pt-free counter electrode in dye-sensitized solar cells [199, 200, 201]. Relatively higher conversion efficiencies were

achieved in such structures (up to 7.69%), favoring the usage of low-cost MoS_2 carbon hybrid structures as Pt-free counter electrodes in dye-sensitized solar cells [201].

FETs based on 2D MoS_2 have been demonstrated as phototransistors [202, 203]. Voltage transfer curves (VTC) and dynamic responses of such phototransistors are presented in Figure 2.7. Single-layer MoS_2 is tuned to the energy bandgap of 1.8 eV, while the bandgap of double- and triple-layered MoS_2 is reduced to 1.65 and 1.35 eV, respectively.

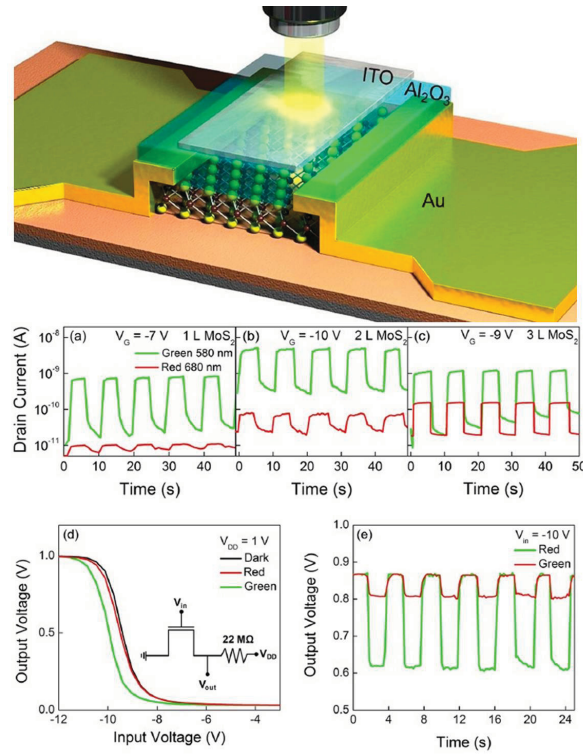


Figure 2.7: Schematic 3D view of monolayer MoS_2 phototransistor, with thick Al_2O_3 (50 nm) dielectric, and ITO topgate under monochromatic light. Respective photocurrent dynamics of (a) mono-, (b) bi-, and (c) tri-layer MoS_2 transistors under monochromatic red and green lights. (d) Dark and photo induced VTC curves of a photo-inverter composed of serially connected resistor and bilayer MoS_2 transistor (see the inset for the circuit). (e) Voltage dynamics of the resistive type photo-inverter under monochromatic red and green lights [202].

Sensors. 2D TMDCs offer great potential for the development of highly sensitive and low cost sensors. This includes optical, gas, bio, electrochemical and electromechanical sensors. The tunability of the bandgap allows for the fabrication of photodiodes and phototransistors that are engineered to almost any desired wavelengths in the UV, visible and IR regions.

Sensors based on 2D TMDCs offer great possibilities for developing highly sensitive, semiconductive, gas detection systems. Their remarkable sensitivity is based on the fact that the 2D layers are very sensitive to embedded Coloumbic charges. It is well-known that gas and vapor molecules can reduce or oxidize TMDCs; hence, this results in both a change of carrier charge mobility (according to Equation 2.2) and carrier concentration. These, in turn, change the conductivity of each layer, which can be readily measured. This effect can also be used in the development of sensitive electrochemical transducers. The Born approximation equation also suggests that the 2D films will be extremely sensitive to the materials that are adsorbed onto their surfaces and generate roughness changes. Biomaterials such as proteins, when adsorbed onto the surface of the 2D layers, change both the surface roughness and the permittivity, therefore causing changes in the electronic properties of each layer. Along these lines, it has been shown that 2D TMDC based sensors are highly sensitive to toxic gases and pollutants, as well as various chemical and biological agents [204, 205]. Zang et al. have demonstrated the applicability of single and multilayered MoS₂ FETs as room temperature highly sensitive NO gas sensors [205]. More recently, they have also developed flexible gas sensor arrays for detecting NO₂, based on MoS₂ thin film transistors with reduced graphene oxide electrodes [204]. Highly selective chemical vapor sensing properties towards organic compounds have also been reported in monolayered MoS₂ [206]. Furthermore, the addition of well-known catalysts such as Pt or Au onto the surface of the 2D layer increases the sensitivity. Electrochemically reduced monolayer MoS₂ nanosheets with good conductivity, superior electron transfer rates and high electrochemical activity have been successfully used for detecting glucose and biomolecules [207].

2.3 Synthesis and exfoliation of layered MoS_2

2.3.1 Mechanical exfoliation

Mechanical exfoliation is a simple technique that has become the most widespread process adopted for achieving monolayers since the discovery of graphene [6, 157]. It involves the application of a mechanical force, e.g. using adhesive tape, to exfoliate the bulk materials into mono- as well as multi-layered flakes (Figure 2.8).

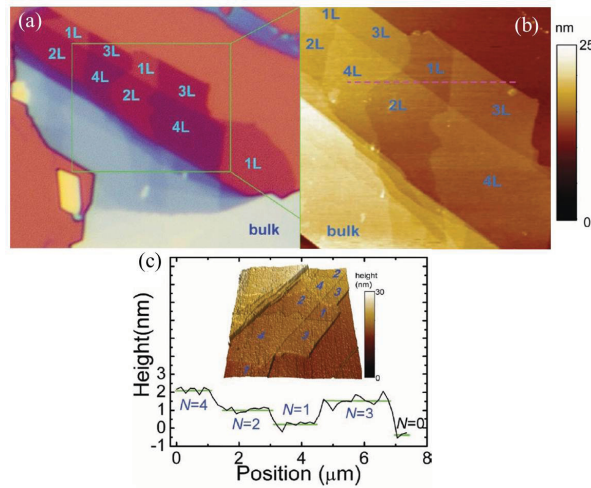


Figure 2.8: (a) Optical image of MoS_2 sample placed on the surface of a heavily doped silicon wafer capped by 285nm thick silicon dioxide. The number of layers (1 L, 2 L, 3 L, 4 L and bulk) are labeled. (b) AFM height image of the region inside the green square in (a). Inset: color bar of height signal. (c) Height profile along the dashed line in (b). Inset: 3D plot of the AFM height signal. [162].

This process exploits the weakly bonded nature of the layers between the planes. Its main limitation is that it cannot be implemented on a large scale. Many of the interesting properties and applications reported for monolayered MoS_2 have also been achieved through mechanical exfoliation [151, 157]. Mechanical exfoliation can be considered to be the most effective technique in establishing proof-of-concept studies, as it produces high quality intrinsic 2D materials. However,

for large scale fabrication of 2D devices, other options should be explored.

2.3.2 Chemical Vapour Deposition of layered MoS₂

Several chemical vapour deposition (CVD) methods for large-scale MoS₂ ultrathin films preparation have been reported recently. A typical process follows these two steps: first, different Mo and sulfur precursors are heated to a high temperature to let them evaporate; second, products deposit on the substrates at the cold zone. For example, MoO₃ and sulfur powder [11], MoCl₅ and sulfur powder, one precursor (NH₄)₂MoS₄ containing both molybdenum and sulfur [208], or molybdenum metal thin film on substrate and sulfur powder [12] have been used. The products of these methods are all polycrystalline single- or few- layer MX₂ with grain size 10-30nm [11, 12]. Recently, the mechanism of CVD method by MoO₃ and sulfur powder has been systematically studied, showing that the nucleation concentration was higher near the grain boundaries [11]. The precursor concentration and the chamber pressure played key roles in controlling the quality of the product. By modifying the process, the CVD method using MoO₃ ribbons as a precursor can produce single- or few- layer MoS₂ on micrometer scale.

2.3.3 Identifying monolayers

Following exfoliation, identifying the number of layers in the 2D TMDCs is a crucial step. Simple techniques for identifying monolayers are required to increase efficiency of the process. Mechanical procedures such as scanning probe microscopy (SPM) and atomic force microscopy (AFM) have already been established in identifying such thin layers [6, 209]. Raman spectroscopy is an excellent tool for identifying the layer dependent bond vibrational distinctions caused by lattice structural variations (as shown in Fig 2.3)[146]. The ability to map the wavenumber of the thickness dependent Raman vibration mode (E_{2g}^1), offers a method to accurately identify the number of MoX₂ layers. Interestingly, the A_{1g} mode is also dependent on the number of layers. Figures 2.9 illustrates the wavenumber map of E_{2g}^1 and A_{1g} modes of a multilayer MoS₂ flake [162].

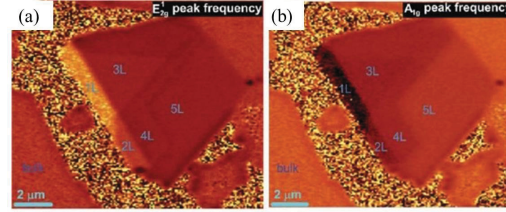


Figure 2.9: Raman peak frequency map of (a) E_{2g}^1 mode and (b) A_{1g} mode of a multi layered MoS_2 flake [162].

Optical microscopy is the most commonly adopted technique for identifying the number of layers of large area coverage. In general, the material is exfoliated onto silicon dioxide on silicon (SiO_2/Si) substrates with a specific SiO_2 thickness (270 to 300 nm). Different layer thicknesses are then identified by comparing the optical color contrast to previously benchmarked thicknesses [209]. However, in certain cases the optical contrast between monolayer, bilayers and tri-layers tends to be ambiguous. Zhang et al. have reported an easier solution utilizing optical microscopy in combination with image analysis software [209]. Here, grayscale optical microscope images of multilayered flakes are obtained, and the color image is then split into three monochromic red (R), green (G), and blue (B) channels. Figures 2.10 (a) and (b) show an R-channel image of a multilayer large area MoS_2 flake and the corresponding Raman frequency mapping. The intensity difference between the MoS_2 layers and the substrate was observed to be increasing with the number of layers [209].

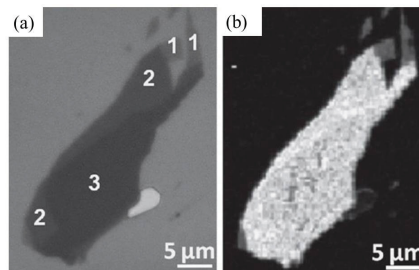


Figure 2.10: (a) Monochromic red channel optical microscope image of a few layer MoS_2 and (b) its corresponding Raman peak frequency mapping for comparison [209].

2.4 Tuning the MoS₂ properties via thermal or plasma treatment

Recently, studies were conducted on the possibility to modify and control the properties of MoS₂ through plasma treatment or thermal treatment, with the aim of being able to use this material in many fields and applications. The controlled changes, on 2D materials offer a means to regulate the electronic, optical, chemical and catalytic properties [210]. Kang et al. and Islam et al. have carried out various studies on the changes of optical [211] and electrical properties [212] through the use of treatment in oxygen plasma, forming defects which alter the optical and electrical properties of MoS₂. Kang et al. Have demonstrated the presence of molybdenum trioxide (MoO₃) coming from exposure to oxygen plasma. With increasing plasma exposure time, the photoluminescence (PL) evolves from very high intensity to complete quenching, accompanied by gradual reduction and broadening of MoS₂ Raman modes, indicative of distortion of the MoS₂ lattice after oxygen bombardment (as shown in Fig. 2.11).

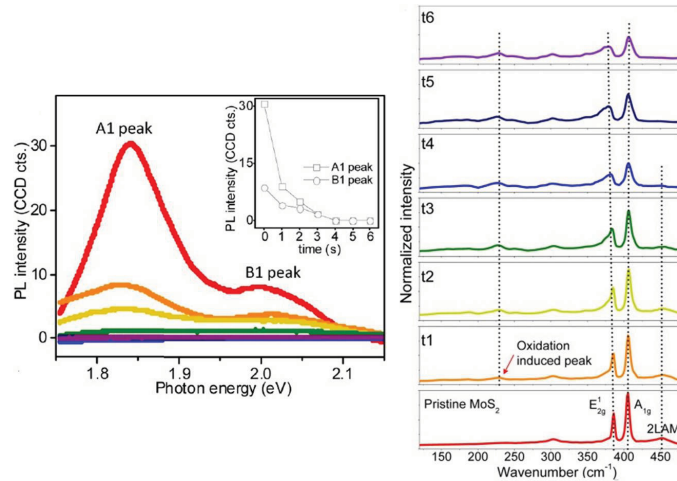


Figure 2.11: (left) Photoluminescence spectra (PL) at different times of a single-layer of MoS₂ untreated (red curve) and treated in oxygen plasma (other curves). The inset shows the PL intensity of the peaks A₁ and B₁ as a function of plasma exposure time. (right) Raman spectra of single-layer pristine MoS₂ and plasma-treated MoS₂ as a function of plasma exposure time. Adapted from [211].

The studies of Islam et al, show that the electrical properties of single-layer MoS_2 can be significantly tuned from the semiconducting to the insulating regime via controlled exposure to oxygen plasma. The mobility, on-current and resistance of single-layer MoS_2 devices were varied by up to four orders of magnitude by controlling the plasma exposure time (as shown in Fig. 2.12). Also in this case, the variation of electronic properties is caused by the creation of insulating MoO_3 -rich disordered domains in the MoS_2 sheet upon oxygen plasma exposure, leading to an exponential variation of resistance and mobility as a function of plasma exposure time.

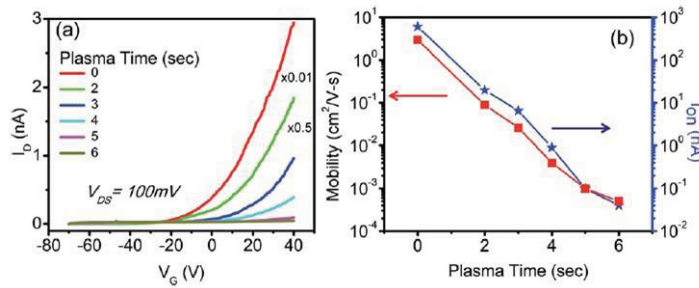


Figure 2.12: (a) Characterization I_D - V_G before and after different plasma exposure times. The curve corresponds to the plasma exposure time of 0, 2, 3, 4, 5, and 6 s respectively. (b) Effect of plasma exposure on the on-current (at $V_G = 40$ V) and mobility of the singlelayer MoS_2 device [212].

As well as under the plasma treatments of O_2 it is possible to modify the properties of MoS_2 even with heat treatment in a controlled atmosphere of oxygen in a range of temperatures between 300 and 400°C. Yamamoto et al. have shown that with thermal treatment in oxygen atmosphere to temperatures of about 200°C, it is not possible to detect a shift of the typical Raman bands of MoS_2 to indicate a p-type doping, up to the achievement of the oxidation, and then the conversion into MoO_3 for higher temperature is detected [210] (as shown in Fig. 2.13).

These results, together with those previously reported for thermal treatments in controlled atmosphere of graphene, show the relevance of the study of the effects of treatments with opportune gas and temperature of 2D materials to induce doping and obtain 2D-systems

adapted for electronic applications.

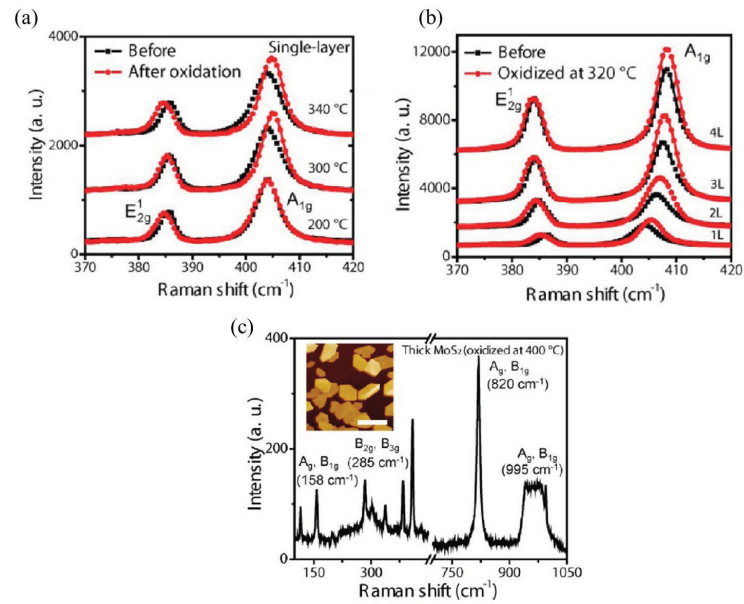


Figure 2.13: (a) Raman E_{2g}^1 and A_{1g} modes of single-layer MoS₂ before (black) and after (red) oxidation at 200, 300, and 340 °C for 2 h. (b) Raman E_{2g}^1 and A_{1g} modes of 1L, 2L, 3L, and 4L MoS₂ after oxidation at 320 °C for 2 h. (c) Raman spectrum of thick MoS₂ oxidized at 400 °C for 10 min, showing MoO₃-related peaks. The inset is an AFM image of oxidized thick MoS₂ crystals at 400 °C. The scale bar is 1 μm. Adapted from [210]

Chapter 3

Experimental Techniques

This chapter will briefly introduce the physical concepts behind Raman spectroscopy, with some insight into the Raman microscopy (micro-Raman), and atomic force microscopy (AFM). Such techniques are widely used in the study of the graphene and molybdenum disulfide, and the changes induced by experiments carried out in this thesis.

3.1 Theoretical background of the employed experimental techniques

3.1.1 Raman spectroscopy

One of the most important aspects in the field of the interaction of radiation with matter is the study of vibrational and rotational modes of the isolated molecules or solid, liquid or gas systems. If we consider an electromagnetic wave, this consists of an electric and a magnetic fields component perpendicular to each other. The electric field (E), in particular, at a given instant of time (t) in a specific position of the space can be described by the expression [213]:

$$E = E_0 \cos(2\pi\nu \cdot t) \quad (3.1)$$

where E_0 is the amplitude of the electric field and ν is the frequency of the radiation.

The minimum spatial distance between two points having the same wave phase (or amplitude) is said wavelength, λ , and has the dimensions of a length. The time separation in a given spatial point between the field values of the same phase determines the wave period, T , and its frequency, $\nu = 1/T$. The connection between the previous quantities is

$$\nu = \frac{c}{\lambda} \quad (3.2)$$

where c is the speed of light in vacuum ($c \sim 3 \cdot 10^8 \text{ m/s}$). The frequency measurement unit is s^{-1} , also called Hertz. We can write:

$$\nu = \frac{c}{\lambda} = c\tilde{\nu} \quad (3.3)$$

where the wavenumber ($\tilde{\nu}$) has been introduced. The difference between $\tilde{\nu}$ and ν is obvious. While the unit of frequency is the Hertz, that of the wave number is conventionally in spectroscopy cm^{-1} . Despite ν and $\tilde{\nu}$ differ by a factor c , the word frequency for both quantities is commonly used in vibrational spectroscopy.

If a molecule interacts with the electromagnetic field, the energy transfer from the field to the molecule can usually occur if the condition is satisfied:

$$\Delta E = h\nu = h\frac{c}{\lambda} = hc\tilde{\nu} \quad (3.4)$$

where ΔE is the energy difference between two quantized states of the molecule, h is Planck's constant ($h = 6.62 \cdot 10^{-34} \text{ J} \cdot \text{s}$). Thus the wave number, $\tilde{\nu}$, is directly proportional to the energy of transition. Suppose that $\Delta E = E_2 - E_1$ where E_2 and E_1 are respectively the energy of the excited state and the ground state. The molecules absorb ΔE when they undergo the transition $E_1 \rightarrow E_2$ and emit ΔE for the reverse transition, $E_2 \rightarrow E_1$, as schematically shown in Fig. 3.1

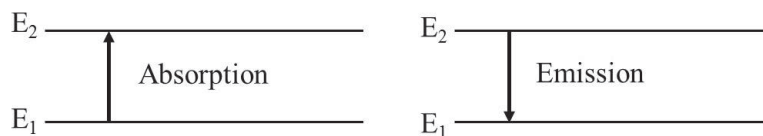


Figure 3.1: Schematic representation of absorption and emission processes between two energy levels of a molecular system.

We can write, so

$$\Delta E = E_2 - E_1 = hc\tilde{\nu} \quad (3.5)$$

In Fig. 3.2 the scales relative to $\tilde{\nu}(cm^{-1})$, $\lambda(cm)$ and $\nu(Hz)$ schematically appear grouped by types of experiments of interaction of radiation with matter, and a table is reported where it emerges that the amplitude of ΔE , expressed in cm^{-1} , depends on the origin of the physical process.

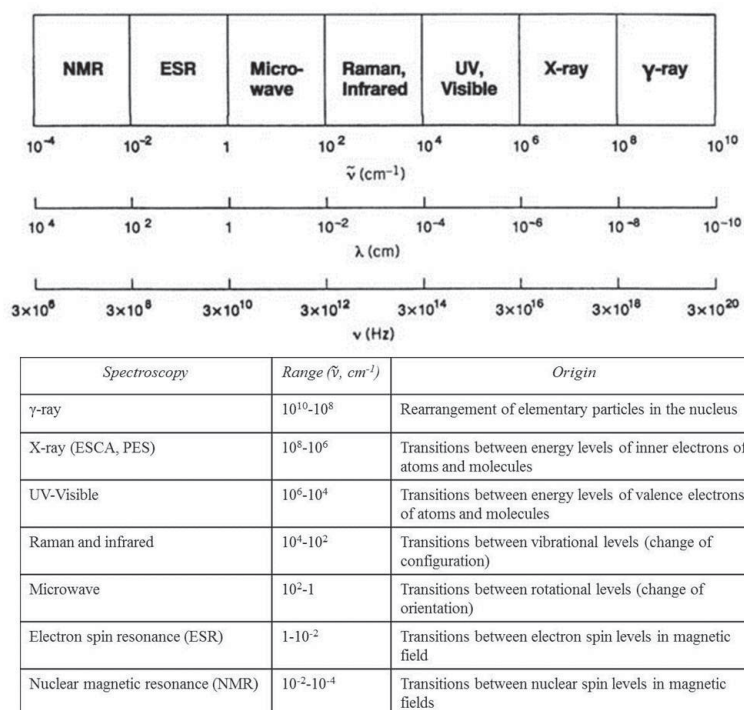


Figure 3.2: Scheme of the spectral ranges of interaction processes between radiation and matter for some spectroscopic techniques and summary table of induced processes [213]

Fig. 3.3, illustrates three types of molecular transitions of interest in spectroscopy. In particular, the purely electronic, vibrational and rotational transitions are shown.

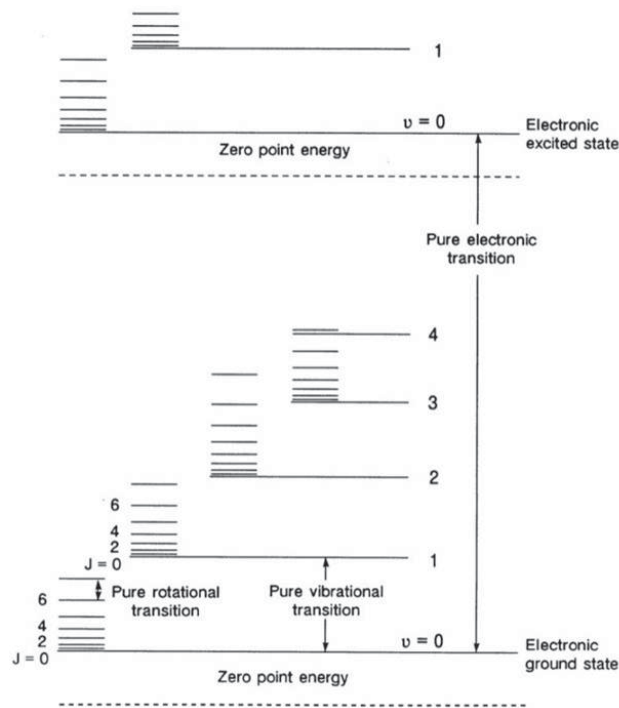


Figure 3.3: Schematization of the electronic, vibrational and rotational energy levels of a molecule and some processes of transition between the corresponding states [213].

The vibrational transitions can be observed both in the absorption spectra in the Infrared (IR) range and in Raman scattering processes. These transitions appear in the region ranging from 10^2cm^{-1} to 10^4cm^{-1} and originate from the nuclear vibration. In the first case, we measure the absorption of infrared light by the sample as a function of the frequency. The molecule absorbs $\Delta E = h\nu$ from the IR source for given molecular vibrations. The IR absorption intensity is governed by the law of Lambert-Beer:

$$I = I_0 e^{-\varepsilon c_0 d} \quad (3.6)$$

where I_0 and I indicate, respectively, the intensity of the incident and transmitted beam, as shown in Fig. 3.4, ε is the molar absorption coefficient, c_0 and d are the concentration and length of the sample,

respectively [213]. The absorbance is given by:

$$A = \log \frac{I_0}{I} = \varepsilon c_0 d \quad (3.7)$$

and gives information on the absorbing species for a given vibration frequency



Figure 3.4: Pictorial representation of an absorption experiment; I_0 indicates the radiation incident on a sample, I the transmitted radiation and ν its frequency [213].

The origin of the Raman spectra is different from that of the IR spectra. In particular, Raman effect is a scattering phenomenon and not an absorption process. In particular, it is useful to note that the Raman effect is a non-resonant phenomenon since, theoretically, it can be observed regardless of the frequency of the radiation used. The sample is usually irradiated in a Raman experiment with laser energy in the UV-Vis region (ν_0) and the scattered light is observed typically in a direction perpendicular to the incident beam, as shown in Fig. 3.5.

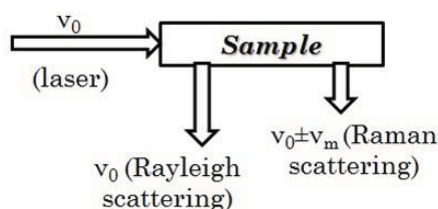


Figure 3.5: Schematic representation of an experiment of Raman scattering; ν_0 indicates the frequency of the incident radiation on a sample, $\nu_0 \pm \nu_m$ the frequency of the inelastically scattered radiation due to the Raman effect and ν_0 the elastically scattered light [213].

The light diffused by the sample contains three contributions: the first and most intense, called Rayleigh scattering, has the same frequency as the incident beam (ν_0), and the other two, called Raman scattering, weaker, with frequencies $\nu_0 \pm \nu_m$, where ν_m indicates the

vibrational frequency of the molecule [213]. Signals with $\nu_0 - \nu_m$ and $\nu_0 + \nu_m$ frequencies are called, respectively, Stokes and anti-Stokes. Thus, in Raman spectroscopy, it is possible to measure the vibrational frequency, ν_m , as the shift from the incident laser beam frequency (ν_0).

The frequency shift of the scattered radiation was observed for the first time by the Indian physicist C.V. Raman, in 1928 (Nobel Prize in 1931), as change in color of the scattered light [213]. Raman discovered that a small fraction of the radiation scattered by certain molecules had different and greater energy than that of the incident radiation, and that the difference in energy was related to the chemical structure of the molecules responsible for the diffusion.

According to the classical theory, Raman scattering can be explained as follows [213]. Consider the electric field (E) of a monochromatic electromagnetic wave in a given spatial position

$$E = E_0 \cos(2\pi\nu_0 t) \quad (3.8)$$

where E_0 is the field amplitude and ν_0 is the frequency of the laser.

If a diatomic molecule fixed in space is irradiated by this light, an electric dipole moment P is induced

$$P = \alpha E = \alpha E_0 \cos(2\pi\nu_0 t) \quad (3.9)$$

where α is the polarizability. In general, for E three components may be present

$$E \equiv (E_x; E_y; E_z) \quad (3.10)$$

furthermore, in a real molecule its polarization is affected by the direction of the chemical bond with respect to the electric field. As a result, the direction of the resultant dipole moment, in general, does not coincide with the direction of the applied field

$$\begin{pmatrix} P_x \\ P_y \\ P_z \end{pmatrix} = \begin{pmatrix} \alpha_{xx}; \alpha_{xy}; \alpha_{xz} \\ \alpha_{yx}; \alpha_{yy}; \alpha_{yz} \\ \alpha_{zx}; \alpha_{zy}; \alpha_{zz} \end{pmatrix} \begin{pmatrix} E_x \\ E_y \\ E_z \end{pmatrix} \quad (3.11)$$

$$P = \hat{\alpha} E \quad (3.12)$$

therefore, the polarizability is a tensor [213]. According to classical electromagnetic theory, an oscillating dipole with frequency ν emits

electromagnetic radiation of the same frequency with intensity [213].

$$I = \frac{16\pi^4\nu^4}{3c^2}|P|^2 \quad (3.13)$$

in this case $\nu = \nu_0$, and assuming, for simplicity, an isotropic polarizability, it can be obtained:

$$I = \frac{16\pi^4\nu_0^4}{3c^2}\alpha^2 E_0^2 \cos^2(2\pi\nu_0 t) \quad (3.14)$$

If we now consider that the molecule vibrates with ν_m frequency, the nuclear displacement from the equilibrium position, q , can be described as

$$q = q_0 \cos(2\pi\nu_m t) \quad (3.15)$$

where q_0 is the amplitude of the vibration. Generally, α is a not known function of q , but for small vibrational amplitudes it can be approximated by the following expression:

$$\alpha = \alpha_0 + \left(\frac{\partial\alpha}{\partial q}\right)_0 q + \dots \quad (3.16)$$

where α_0 is the polarizability in the equilibrium position, and $(\frac{\partial\alpha}{\partial q})_0$ the variation of α , evaluated at the equilibrium position. Combining the expression for P , Eq. 3.9, with the one for q , Eq. 3.15, and for α , Eq. 3.16, it can be obtained to the first order in the series expansion:

$$\begin{aligned} P &= \alpha E_0 \cos(2\pi\nu_0 t) = \alpha_0 E_0 \cos(2\pi\nu_0 t) + \\ &\quad + \left(\frac{\partial\alpha}{\partial q}\right)_0 q E_0 \cos(2\pi\nu_0 t) = \\ &\quad = \alpha_0 E_0 \cos(2\pi\nu_0 t) + \\ &\quad + \left(\frac{\partial\alpha}{\partial q}\right)_0 q_0 E_0 \cos(2\pi\nu_0 t) \cos(2\pi\nu_m t) = \\ &\quad = \alpha_0 E_0 \cos(2\pi\nu_0 t) + \\ &\quad + \frac{1}{2} \left(\frac{\partial\alpha}{\partial q}\right)_0 q_0 E_0 \{ \cos[2\pi(\nu_0 + \nu_m)t] + \\ &\quad \quad \quad + \cos[2\pi(\nu_0 - \nu_m)t] \} \quad (3.17) \end{aligned}$$

In accordance to the classical theory, the first term of Eq. 3.17 is an oscillating dipole that radiates light of frequency ν_0 (Rayleigh scattering), while the second and third terms correspond to the Raman

scattered light with frequencies $(\nu_0 + \nu_m)$ (anti-Stokes) and $(\nu_0 - \nu_m)$ (Stokes). If $(\partial\alpha/\partial q)_0$ is zero, the vibration is not Raman-active. The intensity of the scattered radiation, $I \propto |\ddot{p}|^2$, is

$$\begin{aligned}
 I = \frac{16\pi^4}{3c^2} E_0^2 \left\{ \nu_0^4 \alpha_0^2 \cos^2(2\pi\nu_0 t) + \right. \\
 + (\nu_0 + \nu_m)^4 \left[\left(\frac{\partial\alpha}{\partial q} \right)_0 \frac{q_0}{2} \right]^2 \cos^2[2\pi(\nu_0 + \nu_m)t] + \\
 + (\nu_0 - \nu_m)^4 \left[\left(\frac{\partial\alpha}{\partial q} \right)_0 \frac{q_0}{2} \right]^2 \cos^2[2\pi(\nu_0 - \nu_m)t] + \\
 \left. + \text{crossterm} \right\} \quad (3.18)
 \end{aligned}$$

the cross term may be neglected because the power they radiate will average to zero over long time intervals. So the classical theory predicts, correctly, the presence of the Stokes and anti-Stokes lines and also their dependence on the fourth power of the frequency, as shown in Eq. 3.18. However, it provides a wrong intensity ratio

$$\frac{I_{Stokes}}{I_{anti-Stokes}} = \left(\frac{\nu_0 - \nu_m}{\nu_0 + \nu_m} \right)^4 \quad (3.19)$$

According to the classical theory, therefore, the ratio $\frac{I_{Stokes}}{I_{anti-Stokes}}$ should be less than 1, while it is observed experimentally that the Stokes lines are more intense than the anti-Stokes lines, as shown for example in Fig. 3.6.

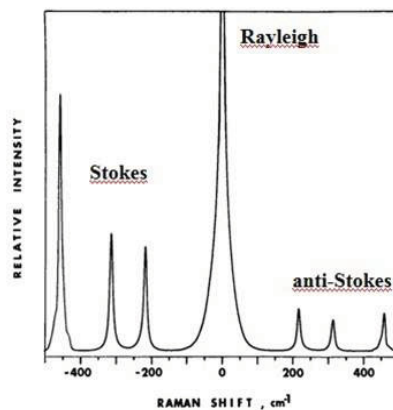


Figure 3.6: Raman spectrum of carbon tetrachloride (CCl_4) [213].

This inconsistency is eliminated by the quantum theory of Raman effect, as schematically shown in Fig. 3.7. A full discussion requires the second quantization of the electromagnetic field, however, a simplified qualitative treatment may be carried out by referring to the diagram of the energy levels of a molecular system [213].

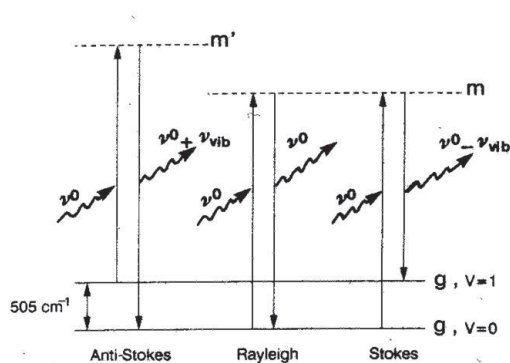


Figure 3.7: Schematic of the energy levels and transitions between molecular states induced by the quantum interpretation of Raman effect. The wavy arrows represent the photons, the dashed lines the virtual states and solid lines the real vibronic states [213].

In details, the process outlined in Fig. 3.7 can be described by the following basic steps [213]:

- In conditions of non-resonance the system undergoes a transition from the ground electronic state, g , and fundamental vibrational level, $\nu = 0$, to a virtual level m . The system quickly decays from the virtual level m to the electronic level g ($\nu = 0$), and the emitted radiation will have the same frequency ν_0 of the incident radiation (Rayleigh line). The system can also decay rapidly from the level m to the first vibrational level $\nu = 1$ of the ground electronic level g , and the emitted radiation will have frequency $\nu_0 - \nu_{vib}$ (Stokes Raman line).
- The system undergoes a transition from the ground electronic state, g , and vibrational excited level $\nu = 1$ to a virtual level m' . The system can decay rapidly from the level m' to the vibrational level $\nu = 0$ of the ground electronic level, g , and the emitted radiation will have frequency $\nu_0 + \nu_{vib}$ (anti-Stokes

Raman line).

From the spectrum shown in Fig. 3.6, it is possible to note that the Stokes lines are more intense than the anti-Stokes lines. This can be explained by considering the origin of these bands: for the Boltzmann distribution at thermal equilibrium the population in the vibrational state $\nu = 0$ prevails compared to that in the vibrational state $\nu = 1$ of the ground electronic level, g, then it is expected that the Stokes process, involving as starting state $\nu = 0$, is most probable than the anti-Stokes process.

Figure 3.8 illustrates Raman scattering in terms of a simple schematic energy levels distribution. In IR spectroscopy, we observe the $\nu = 0 \rightarrow 1$ transition at the electronic ground state. In normal Raman spectroscopy, the exciting line (ν_0) is chosen so that its energy is far below the first electronic excited state. The dotted line indicates a "virtual state" to distinguish it from the real excited state. As previously stated, the population of molecules at $\nu = 0$ is much larger than that at $\nu = 1$ (Maxwell-Boltzmann distribution law). Thus, the Stokes (S) lines are stronger than the anti-Stokes (A) lines under normal conditions.

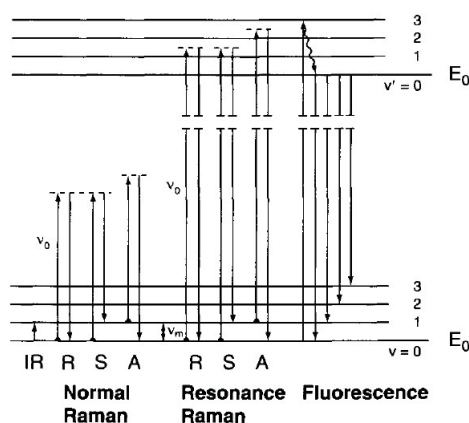


Figure 3.8: Comparison of energy transition for the normal Raman, resonance Raman, and fluorescence spectra[213].

Resonance Raman (RR) scattering occurs, as explained shortly later, when the exciting laser line is chosen so that its energy intercepts the manifold of an electronic excited state. The term "pre-resonance"

is used when the exciting line is close in energy to the electronic excited state. Resonance fluorescence (RF) occurs when the molecule is excited to a discrete level of the electronic excited state. Fluorescence spectra are observed when the excited state of the molecule decays to the lowest vibrational level via radiationless transitions and then the molecule emits radiation, as shown in Fig. 3.8 returning to the ground state. The lifetime of the excited state in RR is very short ($\sim 10^{-14}$ s), while that in RF is much longer ($\sim 10^{-8}$ to 10^{-5} s).

Resonance Raman (RR) scattering occurs when the sample is irradiated with an exciting laser line whose energy corresponds to that of the electronic transition of a particular chromophoric group in a molecule. Under these conditions, the intensities of Raman bands originating in this chromophore are selectively enhanced by a factor of 10^3 to 10^5 . This selectivity is important not only for identifying vibrations of this particular chromophore in a complex spectrum, but also for locating its electronic transitions in an absorption spectrum. Theoretically, the intensity of a Raman band observed at $\nu_0 - \nu_{mn}$ is given by [213]:

$$I_{mn} = \text{constant} \cdot I_0 \cdot (\nu_0 - \nu_{mn})^4 \sum_{p\sigma} |(\alpha_{p\sigma})_{mn}|^2 \quad (3.20)$$

where m and n denote the initial and final states, respectively, of the electronic ground state. Although not explicit in Eq. 3.20, e represents an electronic excited state (Fig. 3.9) involved in Raman scattering. I_0 is the intensity of the incident laser beam of frequency ν_0 .

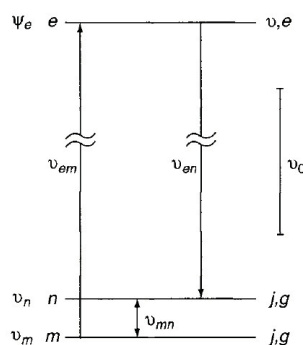


Figure 3.9: Energy level diagram for resonance Raman transition [213].

Finally $(\alpha_{p\sigma})_{mn}$ represents the change in polarizability α caused by the $m \rightarrow e \rightarrow n$ transition, and ρ and σ are x, y and z components of the polarizability tensor. This term can be rewritten as:

$$(\alpha_{p\sigma})_{mn} = \frac{1}{h} \sum_e \left(\frac{M_{me}M_{en}}{\nu_{em} - \nu_0 + i\Gamma_e} + \frac{M_{me}M_{en}}{\nu_{en} + \nu_0 + i\Gamma_e} \right) \quad (3.21)$$

where ν_{em} and ν_{en} are the frequencies corresponding to the energy differences between the states subscribed and h is Planck's constant. M_{me} , etc., are the electric transition moments, such as

$$M_{me} = \int \Psi_m^* \mu_\sigma \Psi_e d\tau \quad (3.22)$$

Here, Ψ_m and Ψ_e are total wavefunctions of the m and e states, respectively, and μ_σ is the σ component of the electric dipole moment. Γ_e is the band width of the e th state, and the $i\Gamma_e$ term is called the damping constant. In normal Raman scattering, ν_0 is chosen so that $\nu_0 \ll \nu_{em}$. Namely, the energy of the incident beam is much smaller than that of an electronic transition. Under these conditions, the Raman intensity is proportional to $(\nu_0 - \nu_{mn})^4$. As ν_0 approaches ν_{em} , the denominator of the first term in the brackets of Eq. 3.21 becomes very small. Hence, this term ("resonance term") becomes so large that the intensity of the Raman band at $\nu_0 - \nu_{mn}$ increases enormously. This phenomenon is called *resonance Raman (RR) scattering*.

The information that the Raman spectrum of a molecule can give derives almost exclusively from Stokes lines. The Rayleigh radiation does not provide any information as it has the same energy in each sample; the anti-Stokes lines are generally of too low intensity to be revealed. The Stokes lines, however, are utilized for analytical purposes to identify compounds in the sample through their vibration modes [213].

In general, it is useful to observe that in a Raman spectrum in ordinate it is reported a quantity proportional to the intensity of light diffused by the sample, in arbitrary units, and in the abscissa, the absolute frequency in cm^{-1} , or, more commonly, the Raman shift, i.e. the difference in wave numbers between the observed radiation and the incident radiation.

Normally, the part of the spectrum with the Stokes signals, the most informative, is shown.

To obtain the Raman spectrum of a sample it is common to use a monochromatic source with a wavelength in the near UV, in the visible or near infrared (NIR). Currently laser sources are used. The laser radiation is focused on the sample; the scattered radiation from the sample is collected, revealed by the detector and displayed in the form of spectrum. Importantly, the Raman shift, for a given bond and a given mode of vibration, is independent of excitation λ , that is from the laser wavelength, but depends only on the energy difference between two vibrational states. However, it is generally possible that the use of different lasers on a single sample generates Raman signals in the same positions but with different intensity, because of the proportionality to the fourth power of the laser frequency, as shown by Eq. 3.18. In terms of the sampling depth, the analysis made with a Raman spectrometer on opaque and solid samples is surface type: the information comes from a thick layer some μm below the surface. Some instruments have the ability to vary the depth of sampling by means of a technique known as confocal, that allows to receive the information from different depth regions of the sample, on condition that this is transparent to the laser radiation.

3.1.2 Raman microscopy

Over the years various combinations of Raman spectrometers equipped with optical microscope have been developed in order to carry out also measurements on the micrometer scale, obtaining a high spatial resolution as well as a spectral one. This technique is known as Raman microscopy or micro-Raman spectroscopy [214]. Raman microscopy was developed around the 1970 [213]. Delhaye, in 1975, made the first micro-Raman measurement. At the same time, Rosasco designed a micro-Raman probe at the National Bureau of Standards (now NIST). These early works affirmed the usefulness of Raman spectroscopy for microanalysis [213].

In the Raman spectrometers equipped with microscopes the area of analysis may be from few up to several hundred μm^2 , depending on the used laser and lens. The normally used lenses have magnification of 10x, 20x, 50x, 80x and 100x. Given this spatial resolution capability, it is required to know exactly where you are on the sample to avoid gross errors; for this reason the Raman microscopes are equipped with

a coaxial camera with the laser, which allows you to view the area on which you are pointing the laser for analysis.

In Fig. 3.10, a typical configuration of a micro-Raman equipment is shown.

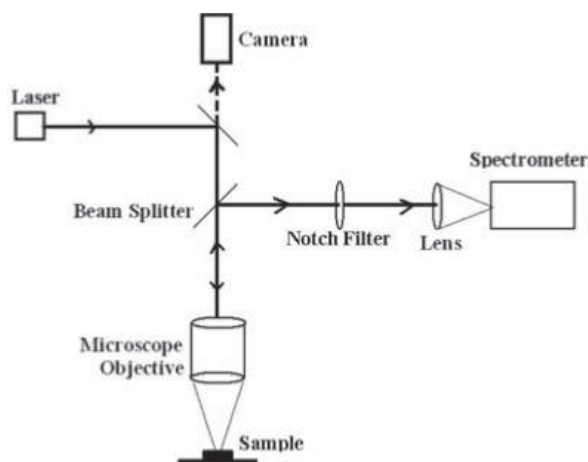


Figure 3.10: Scheme of a Micro-Raman spectrometer [213].

The laser beam runs through the microscope objective, and is focused on the sample. The light scattered from the sample in the opposite direction to the incident one is collected with the same objective and focused on the entrance slit of the monochromator. To eliminate the Rayleigh radiation, usually much more intense than Raman, a notch filter is introduced, that attenuates the intensity at the frequency of the laser radiation [213].

In general, Raman spectroscopy is a non-destructive technique and the spectrum can be obtained from materials in solid, liquid or gaseous phases. Using a Raman microscope, the measurement of spectra from a single sample zone defined by the optical spatial resolution limit of the microscope can be carried out. In addition, a mapping at multiple points of the sample in order to detect and compare with each other the spectra recorded can be done. Raman spectroscopy allows to view, in a non-invasive way, chemical heterogeneity through the use of microscopy; it has proved itself, therefore, a useful technique for the characterization of the materials and the recognition of substances and provides information useful in the manufacture of new materials, the

evaluation of the performance of existing materials and the control of product quality. Because of these properties is a technique used in various technical and scientific fields [214].

3.1.3 Atomic Force Microscopy (AFM)

The invention of scanning probe microscopy is considered one of the major advances in materials science since 1950 [215, 216]. A large family of microscopy methods are included in scanning probe microscopy they share two operational procedures: one uses a sharp probe (tip) and the other a feedback mechanism. The feedback loop is based on keeping a constant value of an interaction parameter while the probe is passed across the sample surface. Scanning probe microscopy began on 1982 after the invention of the scanning tunneling microscope (STM) by Gerd Binnig and Heinrich Rohrer [215, 216]. STM is based on detection of the current that flows between a metallic tip situated a few angstroms above a conductive surface when an external voltage is applied. The limits to obtain images of poorly conducting materials, such as biomolecules, pushed Binnig, Quate, and Gerber to invent the atomic force microscope (AFM) in 1986 [215, 216]. The first AFM operated by measuring the static deflection of the probe. This procedure is actually named contact mode AFM. After one year the dynamic procedure in force microscopy was developed by Martin, Williams, and Wickramasinghe [215, 216]. By this upgrading the AFM started to be used to measure long range forces over a distance range of 3÷15 nm. These researches noticed changes in the amplitude of the tip's oscillation by varying the tip surface distance, and attributed them to the gradient of the tip surface force. Basing of these results Martin and coworkers proposed to use the amplitude in a feedback loop to get an image of the surface.

The principal forces of relevance in force microscopy belong to the electromagnetic field. Nevertheless, interactions with different distance and geometrical dependencies arise from various intermolecular, surface, and macroscopic effects. Van der Waals interactions, short range repulsive interactions, adhesion and capillary forces dominate in air in the absence of external fields. A more complex scenario occurs in liquids, where the solid liquid interfaces together with the presence of ions and electrolytes give rise to additional forces such as the electric

double layer and the solvation forces. The above forces could be separated into attractive and repulsive. In the following the description of forces of relevance for AFM measurements will be described.

As above reported, the force between the samples and the tip is used in AFM to measure the proximity of the tip to the sample. Both long and short-range forces act on the tip sample interaction. The forces are repulsive at close range and attractive at long-range, Fig 3.11.

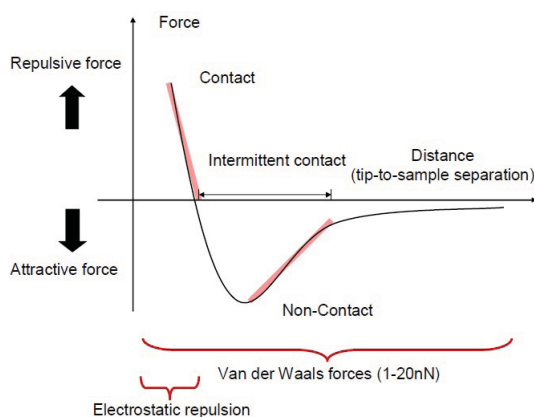


Figure 3.11: Contact mode AFM exploits the repulsive forces at close distance. Non-contact mode AFM is operated in the regime of attractive force. Adapted from [215].

Van der Waals Forces

Force microscopy experiments usually deal with ensembles of atoms or molecules. In these systems van der Waals forces originate from electric dipole interactions between atoms and/or molecules. These could be characterized by either permanent dipole or either induced by another permanent dipole or by thermal fluctuations. Three possible dipole potentials: dipole dipole, dipole induced dipole, or induced dipole induced dipole, characterize the interaction and overall scale as $1/r^6$, where r is the distance between atoms or molecules. These potentials add to give the net van der Waals force between tip and surface atoms [215, 216]. Two approximations are commonly used to describe an AFM interface: the sphere flat and the conical tip sphere

flat geometries (Figure 3.12). The van der Waals force in the sphere flat geometry, is given by

$$F_{vdW} = \frac{HR}{6d^2} \quad (3.23)$$

where H is the Hamaker constant, R the tip radius, and d is the instantaneous tip surface distance. Equation 3.23 has a singularity for $d \rightarrow 0$. When the tip surface distance d is smaller than the intermolecular distance a_0 , to avoid this divergence the resulting van der Waals force is identified with the adhesion force derived from contact mechanics models. A reference value for the intermolecular distance is $a_0 = 0.165\text{nm}$ [215]. The physical properties of materials such as atomic polarizability and the density of the tip, the sample and the neighbouring medium determine the Hamaker constant. Typical values of H are in the 10^{-20} J range.

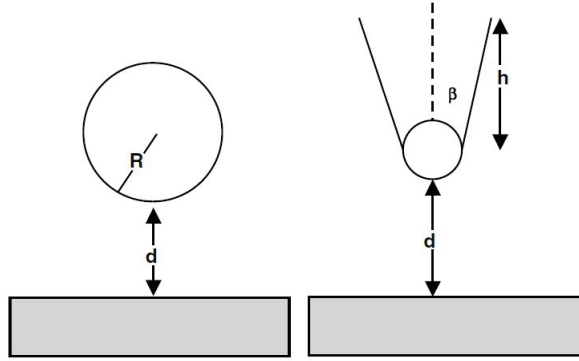


Figure 3.12: Models of the tip surface geometry: sphere flat and conical shaft capped with a half sphere flat [215].

When the tip geometry is a conical mesoscopic that ends in a half sphere [215], the force is described by

$$F_{vdW} = -\frac{H}{6} \left(\frac{R}{d^2} + \frac{\tan^2 \beta}{d + R_\beta} \frac{R_\beta}{d(d + R_\beta)} \right) \quad (3.24)$$

where β is the half angle of the cone and $R_\beta = R(1 - \sin \beta)$. For $d < R$, the half sphere cap determines the van der Waals force and the Equation 3.24 can be approximated by Equation 3.23.

Regarding the sample surface it is necessary to consider its profile. In the case when the sample surface roughness can be approximated

by a succession of half spheres, it is possible to apply the sphere approximation to estimate the van der Waals force,

$$F_{vdW} = \frac{H}{6d^2} \frac{R_t R_s}{R_t + R_s} \quad (3.25)$$

where R_t is the radius of the tip and R_s is the effective radius of the surface below the tip.

Usually, the van der Waals force is attractive, however it is worth to summarize some cases that could often occur. The van der Waals force is always attractive between two identical materials in a medium. The van der Waals force is also attractive for two different materials in air or in vacuum. In the case of two different materials in liquids the van der Waals force could be either attractive or repulsive depending on the values of the dielectric constants and the refractive indexes of the interface [215, 216]. In a heterogeneous interface, consisting of layers of different materials such as a rigid metallic substrate and a thin monolayer on top, the van der Waals force at large distances could still bear the influence of the underlying substrate [215, 216].

Capillary Force

In normal ambient conditions, the presence of moisture is of relevance for AFM measurements. In fact, water spontaneously condenses from vapor into the cracks or pores of hydrophilic surfaces. The effect of capillary condensation is a thermodynamic process that links the vapor pressure of a liquid to its curvature in the condensed form [215]. This feature can be described using the Kelvin equation,

$$R_g T \log \frac{P}{P_0} = \frac{\gamma_L V_m}{r_K} \quad (3.26)$$

where R_g is the gas constant, γ_L is the liquid surface tension, P is the actual vapor pressure, P_0 is the saturation vapor pressure and V_m is the molar liquid volume. For water condensation, P/P_0 is the relative humidity. The Kelvin radius r_K determines the size of the meniscus,

$$\frac{1}{r_K} = \frac{1}{r_1} + \frac{1}{r_2} \quad (3.27)$$

where r_1 and r_2 are the principal curvature radii of the meniscus. The Kelvin equation shows that in equilibrium the vapor pressure determines the size of the capillary where condensation occurs. This

property leads to capillary condensation and capillary adhesion forces in the presence of asperities. Due to this feature at a relative humidity below 100% condensation occurs for curved surfaces.

In the case of AFM measurements, when the tip-sample distance is comparable to the Kelvin radius a water meniscus could be formed (Figure 3.13).

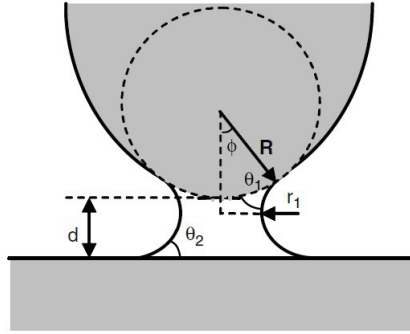


Figure 3.13: Definition of angles and distances needed to calculate the capillary force in AFM. [215].

The formation of the meniscus gives rise to adhesion forces. In particular, inside the meniscus, the pressure is larger than outside and the Young Laplace equation gives the pressure difference across the meniscus interface

$$\Delta P = \gamma_L \left(\frac{1}{r_1} + \frac{1}{r_2} \right) \quad (3.28)$$

The capillary force can be determined by the Young Laplace equation and depends on the interface geometry. As a consequence it is necessary to determine the contact angles between the surfaces and the liquid. In general, for a tip of arbitrary shape and a flat sample, only the numerical solution of the above equation can be used. Nonetheless, several analytical or semianalytical expressions have been proposed to evaluate the force for a spherical tip [215, 216]. Following Israelachvili, the capillary force between a sphere and a flat surface [215] could be estimated by

$$F_{cap} = \frac{4\pi R \gamma_L \cos \theta}{1 + d/d_0} \quad (3.29)$$

The force is attractive and has a maximum value when $d=0$,

$$F_{cap} = 4\pi R\gamma_L \cos\theta \quad (3.30)$$

It is worth to note that capillary condensation is an activated process depending on the relative humidity. The formation of a water meniscus is often observed in AFM experiments performed at ambient conditions, and from an imaging point of view, it should always be avoided, by opportune fluxing dry gas. Furthermore, capillary forces could disrupt the observed objects and should be avoided. Finally, Equation 3.29 shows that capillary forces could reach values in the $1\div 100\text{nN}$ range, and they could dominate all other tip surface interactions.

Electrostatic Forces

Among the forces of relevance for microscopy measurements is the electrostatic force between stationary objects bearing electric charge. This force is repulsive for charges of the same sign; if they are of opposite signs, the force is attractive. The Coulomb's law determines the strength of the force:

$$F = k_e \frac{q_1 q_2}{r^2} \quad (3.31)$$

where r is the separation distance and k_e is the Coulomb constant ($k_e \simeq 8.99 \cdot 10^9 \text{ Nm}^2\text{C}^{-2}$), and q_1 and q_2 are the point charges. The Coulomb interaction gives a long range force nearly always present but not always immediately notable due to dominating short-range repulsive forces. Since over a large distance the decay is exponential the Coulomb interactions between charged surface and particles are significant at short distances.

Nonconservative Forces

All of the above forces are conservative and in many experiments it is rather common to find also nonconservative forces. These latter gives rise to dissipation that depend on both the material properties and the environment. For example, dissipation is involved in force induced atomic or molecular reorientations, interdigitation, and formation and rupture of liquid menisci, or whenever there is an exchange of

atoms and molecules between the tip and the sample [215]. Two major mechanisms can be identified for dissipation at the nanoscale: surface adhesion hysteresis and velocity dependent processes such as viscoelasticity. The first one could consist of long range interactions and short range atomic and molecular interactions. Figure 3.14 schematizes a tip surface force with both short and long adhesion range hysteresis.

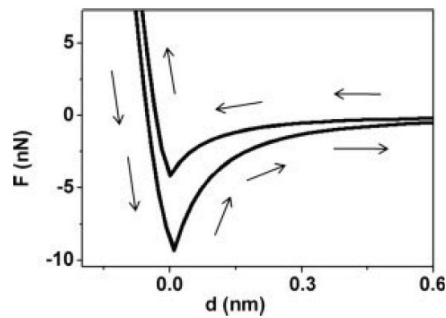


Figure 3.14: Example of a tip surface force that includes surface adhesion hysteresis. The arrows indicate the approach and retraction parts of the oscillation cycle [215].

3.1.4 Amplitude Modulation AFM

For applications, of large interest is the dynamic mode AFM, characterized by tip oscillation to measure the tip-surface interaction through the oscillation amplitude measurements. Typically, the cantilever and tip are solid macroscopic objects in this kind of measurements and it is possible to describe the interaction, using theoretical and computational approaches [215]. In fact, simple equations of motion based on point mass models are widely used.

The cantilever tip system geometry is approximated by a point mass spring that is driven by an external force in the presence of the tip surface forces (Figure 3.15).

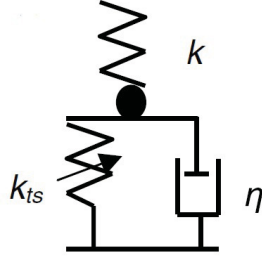


Figure 3.15: Point mass model representation of the cantilever tip surface interface. The arrow over k_{ts} indicates a "nonlinear" spring. Adapted from [215].

The mass-spring system is subject to different forces:

- Driving force;
- Viscous damping, η ;
- External force, F_{ts} .

The relevant equation of motion is:

$$m\ddot{z} = -kz - \eta\dot{z} + F_0\cos(\omega t) + F_{ts}(d) \quad (3.32)$$

or, expliciting η :

$$m\ddot{z} = -kz - \frac{m\omega_0}{Q}\dot{z} + F_0\cos(\omega t) + F_{ts}(d) \quad (3.33)$$

where F_0 and ω are the amplitude and angular frequency of the driving force, respectively; m , Q , ω_0 , and k are, respectively, the effective mass, quality factor, angular natural frequency (undamped), and force constant of the free cantilever. It is worth to note that $m \approx 0.25m_c$, where m_c is the total cantilever mass.

In a typical amplitude modulation AFM (AM AFM) measurement, the driving force is with frequency at the first natural resonance of the cantilever or very close to it. The first resonance is sometimes called the fundamental resonance or mode. Basing on the harmonic oscillator model the force constant and the resonant frequency are linked by:

$$\omega_0 = \sqrt{\frac{k}{m}} \quad (3.34)$$

A solution of Equation 3.33, can be found after explicit definition of tip surface forces. Typically, analytical solutions of the equation are prevented by the nonlinear character of the forces. The above reason together with the similarities observed between the equation of motion of AM AFM and a forced damped harmonic oscillator has led to adoption of the harmonic oscillator model to understand dynamic AFM.

In particular, the tip motion in the proximity of a surface has many similarities with the motion of a driven harmonic oscillator with damping. Basing of this, Equation 3.33, in the absence of tip surface forces ($F_{ts} = 0$), becomes the equation of a forced harmonic oscillator with damping

$$m\ddot{z} = -kz - \frac{m\omega_0}{Q}\dot{z} + F_0\cos(\omega t) \quad (3.35)$$

Similarly to a driven damped harmonic oscillator many of the definitions and concepts can be used to describe the dynamic AFM. In particular, the dependence of the oscillation amplitude as a function of the excitation frequency can be qualitatively described. At low driving frequencies with respect to ω_0 , the response is controlled by the stiffness of the spring. The oscillator moves in phase with the driving force and amplitude close to F_0/k . At frequencies very large with respect to the natural frequency, the term kz is small respect to d^2z/dt^2 and the response is controlled by inertia. In this case, small oscillation amplitude is expected with a phase shift of 180° . In analogy to the driven harmonic oscillator with damping three different regimes for the AM AFM amplitude dynamics are found. The relevant regime for most dynamic AFM experiments is the underdamped regime where $1/2Q < 1$. In this regime the solution is characterized by a transient term and a steady motion

$$z = Be^{-\frac{\alpha}{2}t}\cos(\omega_r t - \beta) + A\cos(\omega t - \phi) \quad (3.36)$$

with $\alpha = \omega_0/Q$. Both terms are relevant at the beginning of motion; and after a time $2Q/\omega_0$, the transient term is reduced by a factor $1/e$. The transient term oscillates with a frequency ω_r that should be considered the new resonant frequency. Elapsed the transient time, a steady sinusoidal motion is established that oscillates with the excitation frequency ω and a phase lag with respect to the excitation force. The damping α modifies the resonant frequency of the harmonic

oscillator. The new resonant frequency is related to the natural resonance frequency by

$$\omega_r = \omega_0 \left(1 - \frac{1}{4Q^2} \right)^{1/2} \quad (3.37)$$

The cantilever quality factor determines the overall dynamics of motion. For low quality factors ($Q < 5$), Equation 3.37 shows substantial differences between the actual and the natural resonant frequencies, otherwise, $\omega_r \approx \omega_0$. The solution for the amplitude of oscillation dependence on the excitation frequency has a Lorentzian expression

$$A(\omega) = \frac{F_0/m}{[(\omega_0^2 - \omega^2)^2 + (\omega\omega_0/Q)^2]^{1/2}} \quad (3.38)$$

and the phase shift can be calculated by

$$\tan \phi = \frac{\omega\omega_0/Q}{\omega_0^2 - \omega^2} \quad (3.39)$$

where ϕ is the phase angle between the driving force and the displacement.

The dependence of the amplitude and the phase shift as a function of the driving frequency are reported in Figure 3.16 for two different values of Q .

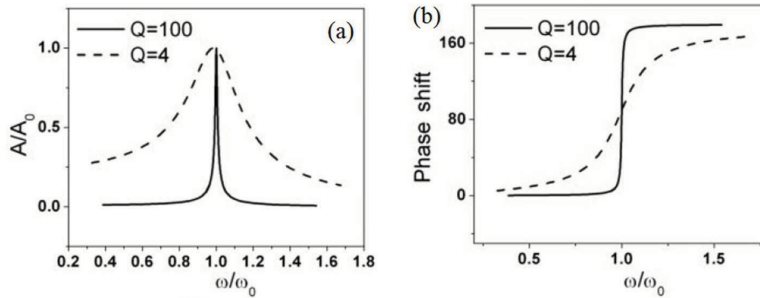


Figure 3.16: Dependence of the amplitude (a) and the phase shift (b) as a function of the excitation frequency for a forced harmonic oscillator with damping. The curves are plotted for two different Q values. The phase shift is in degrees. Adapted from [215].

In the presence of damping, the excitation frequencies at which the maxima of the amplitude and the energy absorbed by the harmonic

oscillator occur do not coincide. The maximum in the amplitude is found for

$$\omega_m = \omega_0 \left(1 - \frac{1}{2Q^2}\right)^{1/2} \quad (3.40)$$

and takes the value

$$A_m = \frac{QF_0}{k} \frac{1}{(1 - (1/4Q^2))^{1/2}} \quad (3.41)$$

By equation 3.39 it is found that the phase shift is exactly 90° at $\omega = \omega_0$ independently on Q . This aspect is of relevance to emphasize the special role of the natural frequency. For example, Equation 3.38 is simplified by exciting the oscillator at its natural frequency ω_0

$$A_0 = QF_0/k \quad (3.42)$$

In the case of interaction with surface forces we need to consider that the point mass cantilever tip is oscillating under the influence of the surface. Under this scheme, the total force acting on the tip includes the elastic response $k(z - z_0)$, the hydrodynamic damping, and the interaction force F_{ts} . In the case of small displacements from the equilibrium position ($z = 0$), the tip surface force can be expressed by a linear approximation

$$F_{ts}(z) = F_{ts}(0) + (dF_{ts}/dz)_0 z \quad (3.43)$$

In this case the gradient of the force influences the tip motion, and the interaction can be characterized by an effective spring constant k_{ts}

$$k_{ts} = (dF_{ts}/dz)_0 \quad (3.44)$$

Taking into account this approximations from Equation 3.33, we find the equation of a forced damped harmonic oscillator

$$m\ddot{z} = -(k + k_{ts})z - \frac{m\omega}{Q}\dot{z} + F_0\cos(\omega t) + F_{ts}(0) \quad (3.45)$$

where the effective spring constant k_{eff} can be introduced

$$k_{eff} = k - (dF_{ts}/dz)_0 \quad (3.46)$$

By solving this equation, a new effective resonant frequency is found

$$\omega_{eff} = \sqrt{\frac{k_{eff}}{m}} \quad (3.47)$$

and the difference $\Delta\omega = \omega_{eff} - \omega_0$ can be approximated by

$$\Delta\omega \approx (\omega_0 k_{ts}/2k) \quad (3.48)$$

The above equations show that by the linear approximation of the interaction force the amplitude modulation AFM behaves like a harmonic oscillator with the resonant frequency depending on the gradient of the interaction. The dependence of the amplitude on the excitation and effective resonant frequencies explain the dependence of the oscillation amplitude on the strength of the interaction force, and on the tip surface separation. Schematically, if the tip is excited at its natural frequency, approaching the tip to the surface will modify the resonant frequency and, as a consequence, the oscillation amplitude will be modified (Equation 3.38). The actual oscillation amplitude will be given by the value of the new resonance curve at the excitation frequency of the oscillator. As a consequence, the new oscillation amplitude would be smaller than the free amplitude (Figure 3.17). However, if the excitation frequency is just off resonance to the left, the oscillation amplitude could decrease or increase depending on the position of the new resonant frequency with respect to the natural frequency. This mechanism is called the detuning effect.

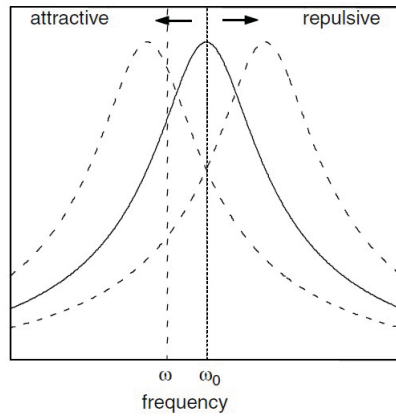


Figure 3.17: Detuning in a weakly perturbed harmonic oscillator. The gradient of the tip surface forces shifts the resonance curve to lower frequencies (attractive force) or to higher frequencies (repulsive force) [215].

Even if the approaches based on the harmonic oscillator model enable to understand amplitude modulation AFM, in many cases,

they might fail to provide agreement with the experiments. The limitations of harmonic models to describe dynamic AFM derive to approximations used to obtain Equations 3.43-3.48. First, it was assumed that the tip surface force induces a frequency shift and not energy transfer. Second, the force gradient was assumed independent of the separation. Third, the force gradient was smaller than the cantilever force constant $k_{ts} \ll k$. Many experiments imply oscillation amplitudes above 1nm violating one or more of the above assumptions.

3.1.5 AFM Image Modes

AFM can be operated in several different modes [215, 216]. In general the image modes are divided into the static mode and the dynamic mode. Static AFM modes include contact mode and friction force microscopy (FFM, or lateral force microscopy, LEM). Dynamic AFM modes include 1. tapping mode, Non-contact mode; 2. force modulation mode (FMM), atomic force acoustic microscopy (AFAM) mode; 3. torsional resonance (TR) mode; 4. Lateral excitation (LE) mode. In this thesis, I will focus on contact mode, tapping mode and non-contact mode.

Contact Mode

The contact mode can be run in two different modes which are the constant height or the constant force. The laser beam measures the deflection of the cantilever, and imaging is collected on the basis of feedback to a piezoelectric scanner that keeps the force constant. Low spring constant AFM probes are used for contact mode imaging. The force applied between the tip and a surface in contact is given by Hooke's law.

$$F = -k_c d \quad (3.49)$$

where F is the force, k_c is the force constant of the cantilever and d the deflection distance. Forces between the tip and samples can be studied by using different tip materials and surfaces. The hardness/elasticity of the surface can be analyzed by varying the force at each point, which is commonly measured for biological samples in air or in liquid. Contact mode is used for high resolution imaging. However, this mode has some limitations: 1. Tip contamination caused by attachment of

particles on a surface; 2 it is easy to damage the surface when a strong force is applied to scanning soft samples.

Tapping Mode

Tapping mode is dynamic and intermittent contact imaging in which the tip senses the surface with only minimal contact to the surface at a given amplitude. The tip oscillates with an amplitude of several nm. The typical frequency of the tip is 50-400 kHz. A resonant oscillation frequency is given by the equation:

$$\omega = \sqrt{\frac{k_{eff}}{m}} \quad (3.50)$$

where k_{eff} is the effective force constant and m the effective cantilever mass.

Non-Contact Mode

Similar to the tapping mode, the non-contact mode brings the cantilever into oscillation slightly higher than the resonance frequency but the tip does not actually touch the sample surface, remaining 5-10 nm from the surface. The tip oscillates with the amplitude of several nm. The typical frequency of the tip is 50-400 kHz. This operation mode is suitable for "soft" materials such as bacteria and proteins.

The following table shows the comparison between these modes of measurements.

Operation Mode	Contact Mode	Non-Contact Mode	Tapping Mode
Contact with sample surface	Yes	No	Periodical
Manipulation of sample	Yes	No	Yes
Contamination of AFM tip	Yes	No	Yes
Advantages	High scan speeds. "Atomic resolution" is possible. Easier scanning of rough samples with extreme changes in vertical topography.	Low force is exerted on the sample surface and no damage is caused to soft samples	Higher lateral resolution (1 nm to 5 nm). Lower forces and less damage to soft samples in air. Almost no lateral forces.
Disadvantages	Lateral forces can distort the image. Capillary forces from a fluid layer can cause large forces normal to the tip-sample interaction. Combination of these forces reduces spatial resolution and can cause damage to soft samples.	Lower lateral resolution, limited by tip-sample separation. Slower scan speed to avoid contact with fluid layer. Usually only applicable to extremely hydrophobic samples with a minimal fluid layer.	Slower scan speed than in contact mode.

Table 3.1: Comparison of three common modes of AFM acquisition.

3.2 Experimental Set-up

This section summarizes the properties of the different instruments used in the thesis. Deep study will be dedicated to Micro-Raman (μ -Raman) and atomic force microscopy, as these are the main measurement techniques employed.

3.2.1 μ -Raman spectrometer

The instrument used for Raman measurements is a microRaman Bruker SENTERRA model, which combines a Raman spectrometer and a confocal microscope to perform the analysis [217] of samples. The instrument allows, therefore, both the optical observation of the sample, using the optical microscopy capacity, and the execution of Raman measurements of micrometric portions of the investigated materials. The visual observation reveals the morphological details of a sample (for example, optical contrast, size, shape), while the spectroscopic measurement gives general information about the vibrational properties, on the molecular structure and the chemical composition of a sample [213, 217]. The apparatus is connected to a computer, equipped with OPUS software, able to acquire both the visual images of the sample and the Raman spectra, obtainable at low and high spectral resolution. For the video or Raman mode the light sources, which radiates the sample, are different: an incandescent lamp (for images) and a laser (for Raman) that emits radiation in the visible (532 nm) with maximum power of 20 mW. As can be see in Fig. 3.18, the instrument consists of two modules: the module of the microscope and the spectrometer module.

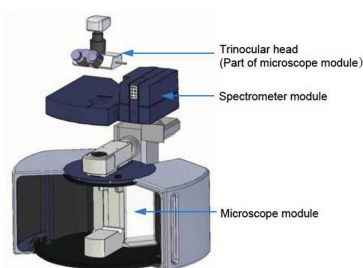


Figure 3.18: Representation of micro Raman spectrometer Bruker SENTERRA [217]

The microscope module is based on the optical microscope OLYMPUS, model BX51 and is constituted by: a trinocular head, consisting of a binocular eyepiece and a third eye in which is mounted a video camera, Infinity1; two objectives, one having magnification 20x, numerical aperture of 0.40 and a working distance 1.3 mm, and the other having magnification 50x, numerical aperture of 0.75 and a working distance 0.38 mm [217].

The spectrometer module is located between the illumination system and the trinocular head of the microscope. The spectrometer consists of [217]:

- a detector, constituted by a CCD matrix 1024x256 pixels thermoelectrically cooled to $-55^{\circ}C$, with operator selectable exposure time to radiation (integration time) and number of repetitions (co-additions);
- two gratings, 400 and 1200 lines/mm, in order to vary the resolution and spectral range (for high resolution, $3 - 5cm^{-1}$, it has a range of $53 - 3700cm^{-1}$; while in the case of low-resolution measurements, $9 - 15cm^{-1}$, the investigated range is $50 - 4478cm^{-1}$);
- a notch filter, positioned before the spectrometer reduces the Rayleigh component of the radiation, leaving unchanged the intensity of light with Stokes-shift exceeding $150cm^{-1}$;
- some slides with opening $25 \times 1000 \mu m^2$ and $50 \times 1000 \mu m^2$ for measurement in non-confocal mode and pinholes $25 \mu m$ and $50 \mu m$ in diameter for measurements in confocal mode.

The sample is placed on a mobile support with a motorized movement controlled by software (Accurate to $1 \mu m$ along the x, y and z), to focus on it optically. This position coincides with the optimization for the collection of Raman signal.

The Fig. 3.19. shows the block diagram of the instrument with the path that the laser radiation performs, in the Raman mode, from the sample to the detector. It can be observed, on the left, that the laser radiation, through neutral density filters (ND Filter), is attenuated before reaching the sample through a sequence of mirrors and a shutter. The radiation then passes through a lens that allows

the focusing at the position of interest. The scattered radiation from the sample, in the opposite direction to the excitation radiation, is collected by the same objective and, through a system of mirrors, is directed towards the spectrograph, passing through a notch filter (F1, in the Fig. 3.19). At the entrance of the spectrograph there is the pinhole/slit which allows the spatial selection of the collected radiation. This system, in particular, allows the confocal detection, and provides the spatial resolution in the direction perpendicular to the plane of the stage on which the sample is positioned. Subsequently, the radiation is dispersed by one of the instrument gratings (located on the Grating turret), selected by the operator, and is detected by the CCD system to record the Raman spectrum.

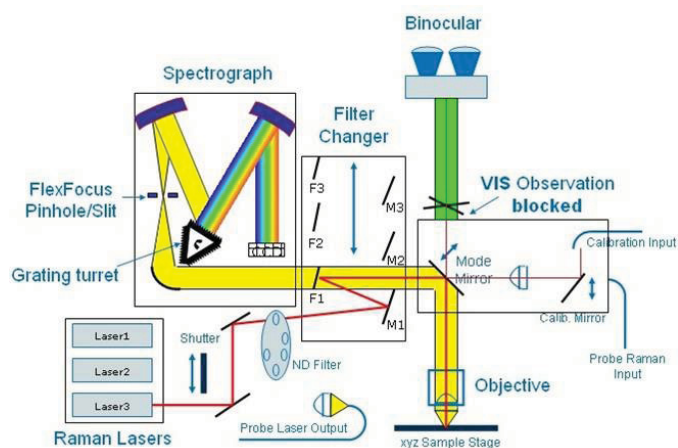


Figure 3.19: Block diagram of the μ - Raman instrumentation with in yellow the path covered by the radiation to reach the detector and in red the excitation laser path [217].

Finally, the instrumental parameters that can be adjusted are listed:

- Laser power (0.2 mW, 2 mW, 5 mW, 10 mW, 20 mW);
- Microscope lens (20x, 50x);
- High Resolution: $5 - 3\text{cm}^{-1}$; Spectral range: 53 to 3700cm^{-1} ;
- Low resolution: $9 - 15\text{cm}^{-1}$; Spectral range: 50 to 4478cm^{-1} ;

- Integration Time;
- Co-additions;
- Aperture ($50 \times 1000 \mu m^2$; $25 \times 1000 \mu m^2$; $50 \mu m$; $25 \mu m$)

Furthermore, additional in-situ -Raman measurements (with the sample inserted inside a Linkam THMS600PS cell with temperature and pressure controlled, see Chapters 4 and 5) were carried out by a Horiba LabRam HR-Evolution spectrometer equipped with a 532 nm excitation laser and spectrometer spectral resolution of 7 cm^{-1} (600 gratings per mm).

3.2.2 Atomic Force Microscope

The microscope for atomic scale resolution used is a Veeco Dimension 3100 (DI3100) atomic force microscope with Nanoscope V controller working in tapping mode and using a commercial silicon probe with spring constant $k = 20 \div 80 \text{ Nm}^{-1}$ and oscillation frequency in the range 332-375 kHz. The Dimension 3100 Scanning Probe Microscope (SPM) produces high-resolution, three dimensional images by scanning a sharp tip over the sample surface. The tip is part of a flexible cantilever mounted on one end of a cylindrical piezoelectric tube mounted near the top of the microscope. Voltages applied to the X and Y electrodes on the piezoelectric tube deflect the tube horizontally to produce a precise raster scan over the sample surface. A voltage applied to the Z electrode on the piezo tube controls the vertical height of the tip. A stepper motor coupled to a lead screw translates a slide with the sample attached [218]. A separate motor drive controls the height of the microscope and tip relative to the sample surface (as shown schematically in Fig. 3.20(a)). The Dimension SPM head provides accurate imaging of a stationary sample while scanning the integrated detector probe assembly above the sample. The Dimension SPM head allows optical correction of the laser beam path to track the movement of the probe while scanning under the fixed laser beam assembly [218]. The Fig. 3.20(b) shows the optical path of the laser beam inside a Dimension SPM head. The Dimension SPM head places a corrective, tracking lens within the scanner tube to stabilize the laser beam focal point atop the scanning cantilever.

This patented technology sharply reduces bowing and attenuation artifacts due to cantilever scanning across the laser beam's otherwise stationary focal plane [218].

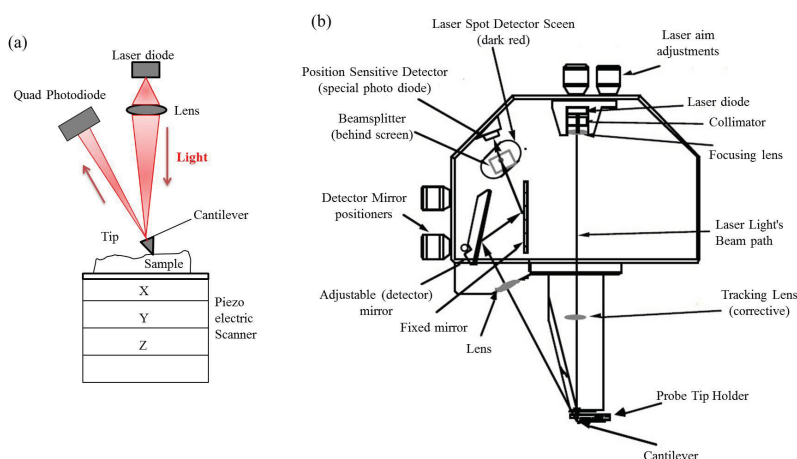


Figure 3.20: (a) Diagram of the light path in an AFM and the main components. (b) Scheme of Dimension SPM 3100D Head [218].

The Dimension SPM head scans the tip and generates the cantilever deflection or probe feedback signal for the different imaging modes. A quad photodetector detects the beam emitted by the laser diode (1.0 mW max at 670nm) as it reflects off the cantilever. The integrated scanner head consists of the following subassemblies [218]:

Preamp Board: The preamp board is located inside the Dimension 3100 SPM microscope head. The preamp board contains a preamplifier circuit for both photodetector signals, a laser diode power supply circuit that regulates the output of the laser, and ± 12 volt regulators for the preamp circuit. The voltage regulators include current limiting to protect the circuit. The preamp board is in turn connected to a 21-pin male connector cable plugged into the socket on the front of the stage control electronics box.

Laser Diode Stage: A kinematic tilt stage positions the laser beam on the cantilever. The tilt stage consists of the laser diode, collimator, focusing lens, base plate, and the X and Y laser diode adjustment knobs. The X laser diode adjustment knob moves the beam parallel to the major axis of the cantilever substrate. The Y

laser diode adjustment knob moves the beam perpendicular to the major axis of the cantilever substrate.

Adjustable Detector Mirror: An adjustable mirror positions the reflected laser spot relative to the four photodetector elements using a kinematic mount and the photodetector mirror adjustment knobs. The photodetector mirror adjustment knobs assist the user in adjusting the position of the mirror to maximize the SUM signal and set the deflection signals.

Photodetector: The four elements of the quad photodetector combine to provide different information depending on the operating mode. In all modes the four elements combine to form the SUM signal. The amplified differential signal between the top two elements and the two bottom elements provides a measure of the deflection of the cantilever. This differential signal is used in Contact AFM mode. The differential signal feeds into an RMS converter (or phase module if attached) for TappingMode operation. Similarly, the amplified differential signal between the sum of the two left photodiodes and the sum of the two right photodiodes provides a measure of the torsion in the cantilever (often used in Lateral Force Microscopy).

Beamsplitter and Laser Spot Detector Screen: The beamsplitter diverts some of the laser light directed towards the photodetector toward the Laser Spot Detector Screen. This screen provides visual indication of the condition of the reflected spot and its orientation relative to the photodetector.

Chapter 4

Materials and Treatments

This chapter is devoted to describe the materials employed in this thesis and the treatments to which the samples were subjected. The principal details are reported to individuate those parameters relevant for the discussion of the experimental results.

4.1 Materials

As reported in Chapters 1 and 2 of this thesis, the materials used are part of the 2D materials category and they are graphene (Gr) and molybdenum disulfide (MoS_2).

As discussed in Chapter 1, the graphene can be produced in different ways. In this thesis we have used graphene samples epitaxially grown on the C-face of the 4H-SiC; graphene samples grown by CVD on Cu and then transferred on SiO_2 substrates on Si (SiO_2/Si); and graphene samples grown by CVD on Cu and then transferred on Al_2O_3 substrates on Si ($\text{Al}_2\text{O}_3/\text{Si}$). As regards the samples of MoS_2 , as we saw in chapter 2 they also can be produced in different ways; we used samples of MoS_2 mechanically exfoliated from a bulk sample and transferred on SiO_2 substrates on Si (SiO_2/Si). In the following paragraphs we go further into the details of the samples preparation.

4.1.1 Gr on C-face of 4H-SiC

As mentioned in Chapter 1, to date, most of the studies on Gr grown on SiC have been carried out on the two polar faces of the hexagonal SiC polytypes (4H and 6H), i.e. the Si-face (0001) and the C-face (000 $\bar{1}$). The structural and electrical properties of Gr have been found to strongly depend on the SiC orientation, due to different growth mechanisms on the two faces. Gr growth on the Si-face starts from the formation of a $(6\sqrt{3} \times 6\sqrt{3})R30^\circ$ surface reconstruction (the so called "carbon buffer layer"), which exhibits a mixed sp^2 - sp^3 hybridization, due to the partial covalent bonding to the Si-face [78, 219]. It proceeds with the conversion of the buffer layer into a Gr layer after the formation of a new interfacial buffer layer due to Si sublimation from the underlying SiC substrate [220]. As a result, Gr layers grown on the Si-face exhibit a very precise alignment with respect to the substrate and are stacked each other according to a Bernal sequence (ABAB). Furthermore, Si sublimation rate from the (0001) face can be precisely controlled to achieve single layer coverage on wafer scale. From the electrical point of view Gr exhibits a high n-type doping ($\sim 10^{13} \text{ cm}^{-2}$) and a relatively poor mobility ($\sim 10^3 \text{ cm}^2\text{V}^{-1}\text{s}^{-1}$) due to a large density of charged Si dangling bonds between the buffer layer and (0001) face [221, 222].

Conversely, Gr growth on the C face of SiC is much more difficult to be controlled, and typically multilayers are obtained under similar growth conditions used for the Si-face. This is in part a consequence of the faster sublimation rate of Si from the (000 $\bar{1}$) face. Differently than for the Si-face, the growth mechanisms of Gr on the C-face as well as the structure of the Gr/SiC interface are still object of debate. No buffer layer formation has been observed and this can explain the rotational (turbostratic) misorientation typically reported between stacked Gr layers [77]. Due to the turbostratic stacking, Gr layers are electronically decoupled each other, and this is at the origin of the excellent electron mobility ($> 10^4 \text{ cm}^2\text{V}^{-1}\text{s}^{-1}$ at 300 K) measured on the C-face [223]. In spite of these very attractive electronic properties, the use of Gr on SiC(000 $\bar{1}$) for field effect transistors has been hindered by the difficulty of efficiently modulating carrier density in multilayers by a gate bias due to mutual electrostatic screening of different layers. Under this point of view, it is highly desirable to achieve the growth

of few layers or even a single layer also on the C-face.

To deepen the understanding of Gr grown on SiC, in this PhD thesis work, the growth conditions (temperature and pressure) have been specifically tailored to achieve the growth of few layers of Gr on 4H-SiC (000 $\bar{1}$). The samples were grown at the University of Linköping; in details, Gr samples were grown on 4H-SiC (000 $\bar{1}$) by thermal treatments at 1850°C, 1900°C and 1950°C in Ar ambient at 900 mbar and, as reported in the following chapters, they have been fully characterized.

4.1.2 Gr on SiO₂/Si and Gr on Al₂O₃/Si

As discussed in Chapter 1, the recent interest in graphene electronic properties has stimulated the development of advanced methods for large-area Gr growth on different kinds of substrates [74, 87, 224]. The most promising low cost and very accessible method for Gr production is the chemical vapor deposition (CVD) on metal substrates (such as Cu, Ni), since with this approach high quality samples can be obtained [87]. The Gr film is grown directly on the substrate surface that acts as a catalyst in the process. In the case of Cu substrates, the resulting film is predominantly composed by single layer Gr domains [225]. For applicative aims the Gr film grown on metal is then transferred on another insulator substrate, such as silica (amorphous SiO₂) or alumina (Al₂O₃), through a transfer procedure consisting first in covering the surface of Gr by a polymer, usually PMMA (poly(methyl methacrylate)), in a successive chemical etching to remove the metal substrate and in the final transfer on the end substrate chosen [8, 225]. Transparent insulating substrates, such as amorphous silica, SiO₂, or alumina, Al₂O₃, are among the most employed substrates for Gr applications in electronics (e.g., as channel material for field effect transistors or interconnects) [226] and optoelectronics (e.g, as transparent conductive electrode) [29].

In the present PhD thesis work, Gr samples were produced by the CVD technique growing them on copper (Cu) foil. Successive transfer on a 300 nm thick SiO₂ layer on Si ((sample hereafter named Gr/SiO₂/Si), or on a 100 nm thick Al₂O₃ layer on Si (sample hereafter named Gr/Al₂O₃/Si) was done by the sequence PMMA deposition,

sample transfer and PMMA removal (as it has been described in Fig. 1.18).

4.1.3 MoS₂ on SiO₂/Si

The isolation of graphene, the single atomic layer of sp² carbon, by exfoliation of graphite represented the first experimental demonstration that two dimensional (2D) materials can be stable under ambient conditions after separation from the bulk crystal [6]. This opened also the way to the investigation of an entire class of layered materials occurring in nature, which are composed by the vertical stacking of 2D sheets bond by van der Waals interaction [7]. In particular, transition metal dichalcogenides(TMD), whose generalized formula is MX₂, where M is a transition metal of groups *IV – X* and X is a chalcogen (S,Se,...), attracted significant interest in the last years [143]. Some of them(in particular MoS₂) are naturally abundant and very stable after exfoliation. Furthermore, MoS₂, MoSe₂, WS₂, WSe₂ have been shown to be semiconductors with sizable bandgaps [143]. The semiconducting properties make TMD very attractive for electronics and optoelectronics fields.

In this work, MoS₂ samples were obtained by mechanical exfoliation of natural bulk molybdenite crystals, purchased by SPI [227]. The exfoliation technique was based on the use of a thermal release tape and thermocompression printing [228] on a SiO₂(300 nm)/Si substrate.

4.2 Treatments

In this section we report details about the treatments employed in this thesis, in particular, the treatments in O₂ plasma and the thermal treatments in vacuum, in air and in a controlled atmosphere (O₂, CO₂, N₂, H₂O) for Gr and MoS₂ samples.

4.2.1 Thermal treatments in muffle oven

The thermal treatments in controlled atmosphere are one of the main experimental procedures used in this thesis. The apparatus schematically shown in Fig.4.1 has been used. It consists of a blind

cylindrical stainless steel pipe of 1 cm internal diameter and length of 1 m. This pipe is connected to a vacuum pump (B) to evacuate the ambient gas, and to a gas bottle (G) to inflate, if needed, high purity gas (<3 part per million mol water, only impurity content) inside the pipe. Valves and manometer are inserted in the system to check the pressure and isolate the different parts. To make thermal treatments on the samples of Gr/SiO₂/Si and Gr/Al₂O₃/Si, in vacuum and in a controlled atmosphere we used the following procedure: the sample was placed inside the stainless steel pipe (A, in Fig.4.1, internal volume ~ 0.08 L); subsequently the air inside the pipe was removed by the vacuum pump (B) in about 2 minutes until inside the tube the pressure value $\sim 10^{-4}$ bar, read via the pressure gauge (D1), was reached.

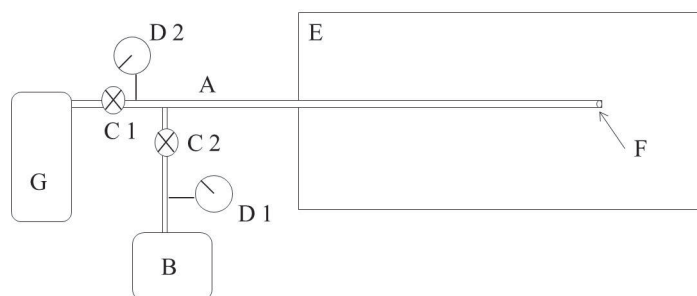


Figure 4.1: Schematic draft of the apparatus used to perform the thermal treatments under vacuum, O₂, CO₂, N₂. The system consists of: (A) a cylindrical stainless steel blind pipe; (B) a vacuum pump; (C1 and C2) two valves; (D1 and D2) manometers; (E) a muffle oven; (G) gas bottles containing O₂, N₂ or CO₂. The samples (F) are put at the end of the blind pipe.

For the vacuum treatment, once the pressure of $\sim 10^{-4}$ bar was reached, it was maintained by keeping the vacuum pump turned on. The pipe was then inserted inside the oven (E) previously heated, at the thermal treatment temperature, and kept there till the time of treatment was elapsed. Afterward, the pipe was extracted from the oven and was cooled in water at room temperature.

For treatments in other atmospheres (O₂, CO₂, N₂), instead, once the pressure of $\sim 10^{-4}$ bar was reached, the valve (C2), in the figure 4.1 was closed, and the gas was injected from the gas bottle ((G) in figure 4.1) at a given pressure in the range 0.5÷10 bar, checked via

the pressure gauge (D2). Thereafter the pipe was inserted inside the oven (E) and the same procedure of treatment above described for vacuum was applied.

For the thermal treatments the temperature was fixed in the $140\div 350^{\circ}\text{C}$ range and was stabilized within $\pm 1^{\circ}\text{C}$. The temperature was checked by a thermocouple inside the oven.

Two kinds of thermal treatments have been carried out isochronous treatments: at fixed treatment time on varying temperature or pressure; and isothermal treatments: at fixed temperature on varying treatment time.

4.2.2 Thermal treatments in situ

Thermal treatments in air and some treatments in O_2 , on samples of $\text{Gr}/\text{SiO}_2/\text{Si}$ and $\text{MoS}_2/\text{SiO}_2/\text{Si}$, were carried out in-situ during Raman measurements, with the aim to clarify certain aspects which we will explain in the next chapter. The sample in these treatments was inserted inside a Linkam THMS600PS cell with temperature and pressure controlled (AtenCenter, CHAB; <http://www.chab.center/home>). During the measurements the temperature was fixed up to 350°C and the pressure up to 2 bar. Heating ramp was selected to $100^{\circ}\text{C}/\text{min}$, whereas cooling to room temperature was obtained within 25 min. Temperature ramp and monitoring were executed by the software station of the Linkam cell.

4.2.3 Thermal treatments in PARR reactor

To apply thermal treatments in water controlled ambient a PARR reactor model 4651 with purging valves (shown in Figure 4.2) was used.

The PARR reactor consists of a stainless steel cylindrical vessel (A), with an internal volume of 250 ml, where the sample is placed during the thermal treatment in controlled atmosphere. The sample is opportunely suspended in a stainless steel sample holder to avoid to soak it into water at room temperature, during water treatments. The vessel is closed by a steel cover (B) with two valves (I and O) for the input and output of the gas used in the thermal treatment. The cover is coupled to the container by means of two steel rings (H) and closed

with bolts.

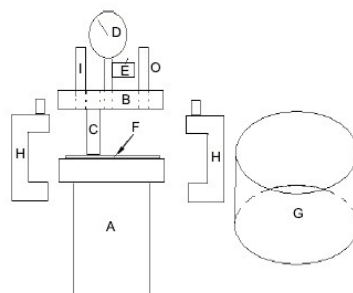


Figure 4.2: Block diagram of the PARR reactor, used to perform the thermal treatments in water gas. The system consists of: (A) stainless steel container; (B) container cover; (C) a well in which a thermocouple is positioned; (D) analogue pressure gauge and (E) digital pressure transducer; (F) gasket; (G) stainless steel sealing ring and (H) two closing mesh rings in stainless steel; (I and O) input and output gas valves, respectively.

Between the lid and the container there is a graphite gasket (F) which serves to avoid the gas release from the system. A thermocouple (C), which is in contact with the bottom of the closure cap, is used with the aim to measure the vessel temperature. Finally, the whole vessel is placed inside a steel ring (G). The pressure is measured by an analog pressure gauge and a digital transducer (D and E respectively). The closed reactor is placed in an electric heater equipped with a temperature control system that stabilizes within 1°C .

The 250 ml T316 stainless steel chamber was filled with 40 ml of liquid distilled water and, after closure, the chamber was repeatedly purged with 50 bar He gas to remove ambient air, and a final He pressure of 7 bar was fixed. The temperature was then raised up to 150°C within 1 hour and a mixture of He (10 bar) and H_2O steam (2 bar) was obtained. The experiment time at 150°C of 2 hours was fixed, afterwards the equipment was returned to room temperature within 10 hours preserving the He- H_2O gas mixture.

Chapter 5

Experimental Results

In this chapter the experimental results obtained in this thesis work are collected. First the properties of multilayers graphene obtained by high temperature treatments on SiC are considered to evaluate the production and quality of graphene as well as its doping. Then monolayers of Graphene on SiO₂ and Al₂O₃ are investigated to elucidate the effectiveness and weaknesses of doping by thermal treatments in controlled atmosphere. Finally, in view of extension to 2D materials, the effects of thermal treatments, similar to those used for graphene, are investigated on multilayers MoS₂ exfoliated from bulk and transferred on SiO₂.

5.1 Graphene on C-face of SiC

As described in the previous chapter, Gr samples were grown on C-face of 4H-SiC (000 $\bar{1}$) by thermal treatments at 1850°C, 1900°C and 1950°C in Ar ambient at a pressure of 900 mbar. As grown Gr samples were preliminarily characterized by optical microscopy (OM) and by atomic force microscopy (AFM) operated in tapping mode. Fig. 5.1 shows three representative OM images of Gr grown at 1850°C (a), 1900°C (b) and 1950°C (c).

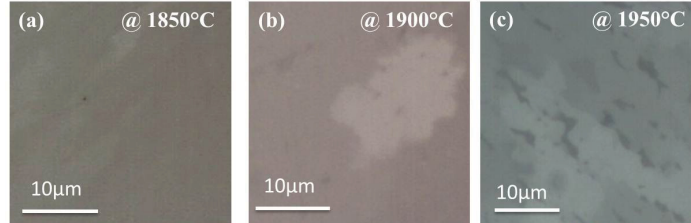


Figure 5.1: Optical images by the microscope of the Raman Senterra instrument of the Gr grown on the C face of SiC at 1850° C (a), 1900° C (b) and 1950° C (c). The different optical contrast indicates a different amount of graphene layers. The scale is in μm . Adapted from [229].

Fig. 5.2(a) reports representative Raman spectra measured on the virgin SiC ($000\bar{1}$) and on as-grown few layers of Gr at 1900°C. To isolate the Raman bands of Gr, a subtraction of the two spectra was carried out after normalization to the intensity of the main peak of SiC Raman signal [230]. The characteristic G and 2D bands of graphitic carbon are observed in the spectral range from 1300 to 2900 cm^{-1} . Furthermore, the absence of the defects-related D band (at ~ 1350 cm^{-1}) demonstrates the high crystalline quality of the few layers of Gr.

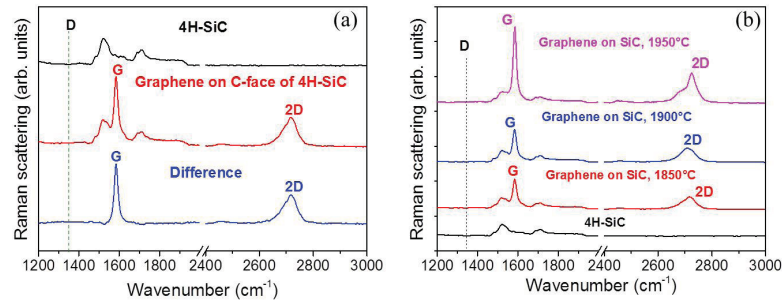


Figure 5.2: (a) Raman spectra of virgin 4H-SiC (black) and of Gr grown on 4H-SiC($000\bar{1}$) at 1900° C (red). The two spectra are normalized to the SiC signal and the blue spectrum is the difference between the red and black ones. (b) Comparison between the normalized Raman spectra of Gr grown at 1850° C, 1900° C and 1950° C and of virgin 4H-SiC [229].

The presence of bright and dark contrast regions in Fig. 5.1 sug-

gests a not uniform Gr coverage at all the investigated temperatures. Representative AFM morphology and phase images for the sample grown at 1900°C are reported in Fig. 5.3(a) and (b), respectively. The morphology shows that Gr grows on a stepped SiC substrate (see also the linescan in Fig. 5.3(c)). Furthermore, peculiar nanometer high corrugations of the Gr membrane (wrinkles) can be observed in the morphology (see the linescan in Fig. 5.3(d)). Such corrugations originate from the compressive strain experienced by Gr in the cooling down step of the growth process, as a result of the different thermal expansion coefficients of SiC and Gr [231].

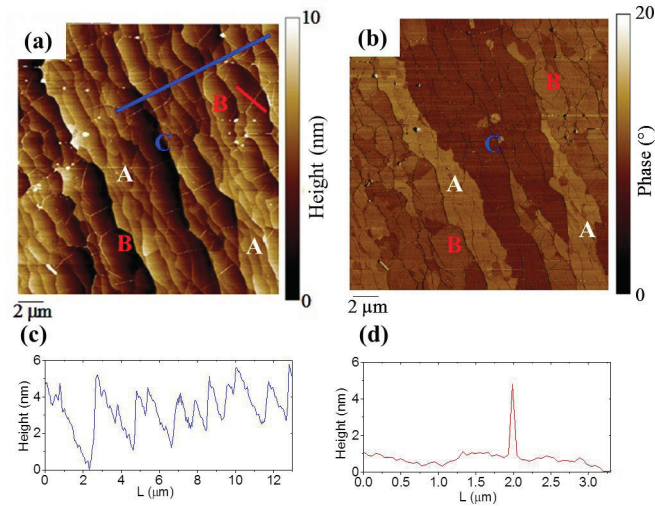


Figure 5.3: AFM morphology (a) and phase (b) images of Gr grown at 1900°C. Representative linescans of SiC steps (c) and of a Gr wrinkle (d) corresponding to the lines highlighted regions in panel (a) [229].

The presence of compressive strain is also confirmed by μ -Raman measurements, as discussed in the following. The phase contrast (Fig. 5.3(b)), originating from the electrostatic interaction between tip and surface, indicates the presence of regions with different surface potentials (indicated with A, B, and C in the map) associated with changes in the number of Gr layers [231].

Atomic resolution STEM¹ measurements (Fig. 5.4) on the cross-

¹Scanning Transmission Electron Microscopy; The measurements were carried out in collaboration with Dr. G. Nicotra and Dr. C. Bongiorno of the National

section of the same sample confirm that regions without Gr and regions with few (1-7) layers are present at different surface positions. Interestingly, an amorphous Si/C interfacial region with almost fixed thickness (1.3-1.5 nm) is evidenced both on the bare and Gr covered regions, almost independently on the number of Gr layers. This amorphous can work as a precursor for Gr growth on C face in the employed growth conditions.

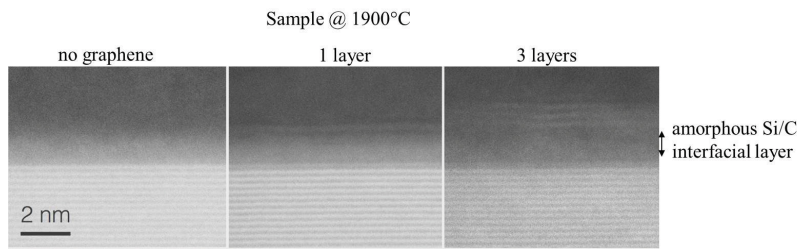


Figure 5.4: STEM images in dark field on three areas of the sample prepared at 1900°C; from left: no graphene, 1 layer of graphene, 3 layers of graphene, the presence of a layer of amorphous SiC is highlighted by the black arrow. Adapted from [229].

Representative Raman spectra measured on the samples grown at 1850°C, 1900°C and 1950°C are reported in Fig.5.2(b). For consistency all the measurements were performed in the samples regions with brighter optical contrast. The presence of the interfacial Si/C amorphous layer, shown in Fig. 5.4, does not introduce any specific features in the Raman spectral region where the signals of SiC and graphene appear. For comparison, all the spectra were normalized to the intensity of the main peak of SiC Raman signal.

Clearly, the G and 2D peaks intensity increases with the growth temperature, consistently with an increase in the number of layers. Furthermore, the 2D peak becomes more asymmetric with increasing temperature. Noteworthy, a symmetric 2D Raman peak indicates the presence of a monolayer of Gr (for $\text{FWHM}(2\text{D}) \sim 30\text{-}40 \text{ cm}^{-1}$) or few layers of Gr with turbostratic stacking (for $\text{FWHM}(2\text{D}) > 40 \text{ cm}^{-1}$). On the other hand, an asymmetric 2D peak can be an indication of a stacking order between different Gr layers [230]. The occurrence

of stacking order also on the SiC(000 $\bar{1}$) is peculiar of the few layers of Gr grown under these conditions and is typically not reported for multilayers. From the analysis, point by point, of the Raman spectra measured at different positions on the three samples (i.e. in the dark and bright areas) a series of information can be deduced. The spectral characteristics of the Raman measurements, in particular the amplitude ratio I_{2D}/I_G and the 2D band shape, enable to distinguish areas in which there is the presence of a monolayer of graphene or a few layers of Gr with turbostratic stacking or with Bernal stacking. In Figure 5.5 examples of Raman experimental spectra for the sample grown at 1850°C are reported.

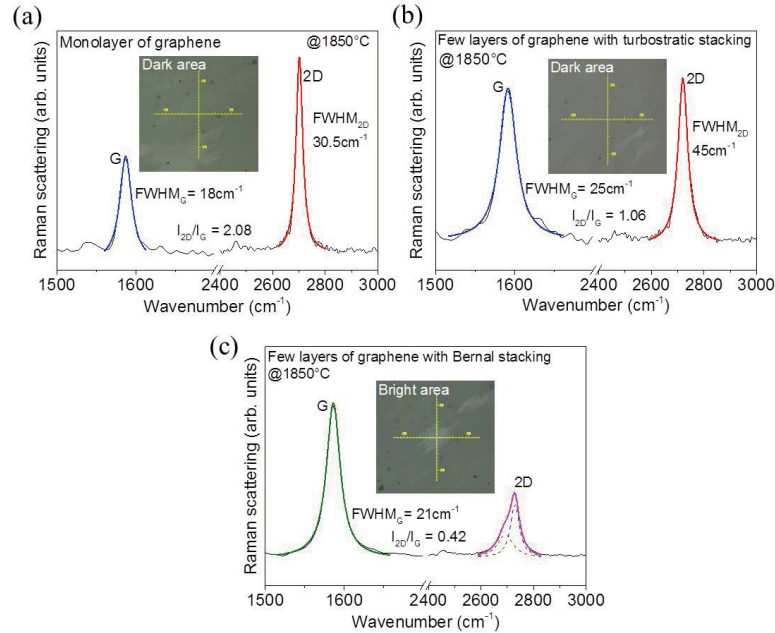


Figure 5.5: μ -Raman spectra of graphene sample grown on the C-face of SiC at 1850°C respectively in dark areas (a) and (b) and bright areas (c), after subtraction of the SiC Raman spectrum. The spectra are focused in the spectral region of the typical bands of graphene and normalized to the G band amplitude. The G and 2D band best fit curves with lorentzian line shapes are superimposed to the spectra. Each of the inset shows the point where the spectrum was acquired.

In this sample there is the presence of dark areas in the optical im-

age that show the spectral characteristics of a monolayer (Fig. 5.5(a)) or of a few layers of Gr with turbostratic stacking (Fig. 5.5(b)); the spectral features namely show a ratio $I_{2D}/I_G > 0.7$ and $30 \text{ cm}^{-1} < \text{FWHM}_{2D} < 50 \text{ cm}^{-1}$. Furthermore, the 2D band has a symmetrical shape and can be interpolated with a single Lorentzian curve. In Figure 5.5(c) an example of the Raman spectrum recorded in the bright areas of this sample is shown. In this case it is immediately evident that $I_{2D}/I_G < 0.7$ and the FWHM of the 2D band is $> 50 \text{ cm}^{-1}$. Furthermore, the 2D band is asymmetrical. These characteristics are attributable to the presence of few layers of Gr with Bernal stacking. In Figure 5.6 the Raman spectra for the sample grown at 1900°C are reported. In this case the bright areas of the sample prevail (compared to the sample grown at 1850°C), attributable to regions with few layers of Gr with Bernal stacking.

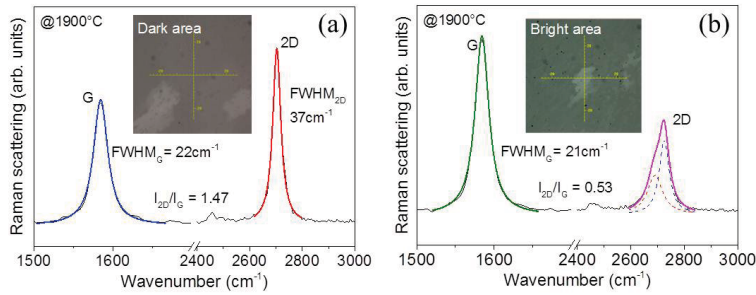


Figure 5.6: μ -Raman spectra of graphene sample grown on the C-face of SiC at 1900°C respectively in dark areas (a) and bright areas (b), after subtraction of the SiC Raman spectrum. The spectra are focused in the spectral region of the typical bands of graphene and normalized to the G band. The G and 2D band best fit curves with Lorentzian line shapes are superimposed to the spectra. Each of the insets shows the point where the spectra were acquired.

Figure 5.7 finally shows the Raman spectra for the Gr sample grown at 1950°C . In this sample, also the measurements made in darker areas, exhibit spectral features that are not typical of monolayers (Fig. 5.7(a)). The I_G/I_{2D} ratio is about 1 and the 2D band is slightly asymmetrical.

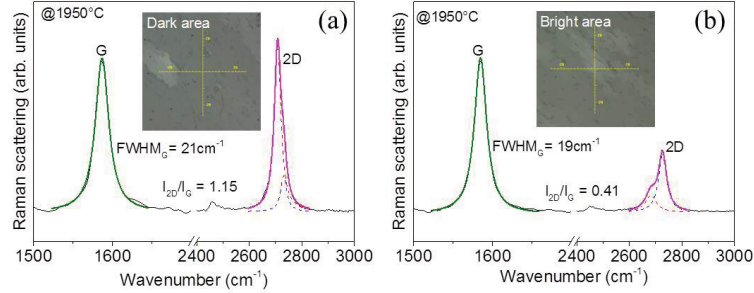


Figure 5.7: μ -Raman spectra of graphene sample grown on the C-face of SiC at 1950°C respectively in dark areas (a) and bright areas (b). The spectra are focused in the spectral region of the typical bands of graphene and normalized to the G band. The G and 2D band best fit curves with Lorentzian line shapes are superimposed to the spectra. Each of the inset shows the point where the spectrum was acquired.

As summarized in Fig. 5.8(a), in the sample grown at 1850°C, that features a prevalence of dark areas with respect to bright areas, the 2D band in dark areas can be fitted by a single Lorentzian curve of FWHM in the range from 30 to 50 cm^{-1} . The regions with $\text{FWHM}(2D) \sim 30 \text{ cm}^{-1}$ are associated to Gr monolayers. The regions with $\text{FWHM}(2D)$ between 40 and 50 cm^{-1} are associated to few layers of Gr with turbostratic stacking [232]. It is also seen that the dark areas are distinguished from bright ones by the I_{2D}/I_G ratio. In combination with the $\text{FWHM}(2D)$, this parameter allows to discriminate areas with single or few layers of Gr ($I_{2D}/I_G > 0.7$) from areas with a larger number of layers ($I_{2D}/I_G < 0.7$) [230]. In particular, it is found that in the bright regions, showing $I_{2D}/I_G < 0.7$, a $\text{FWHM}(2D) > 50 \text{ cm}^{-1}$ is systematically found, and the 2D band also becomes composite and asymmetric. The asymmetric peak has been fitted with two Lorentzian components, associated to Bernal stacking between Gr layers [230]. Almost the same can be said for the sample prepared at 1900°C, as shown in Fig. 5.8(b), where, however, bright areas dominate, indicating an increase in the average number of layers. For the sample prepared at 1950°C a further increase in the average layer number is found. Interestingly, in this sample the Raman spectrum in the dark areas shows a slightly asymmetric 2D band with a shoulder at high wavenumbers, that cannot be fitted with the same components

associated to Bernal stacking. It is also found that the ratio I_{2D}/I_G has maximum values near to 1, indicating a larger number of Gr layers (see Fig. 5.8(c)).

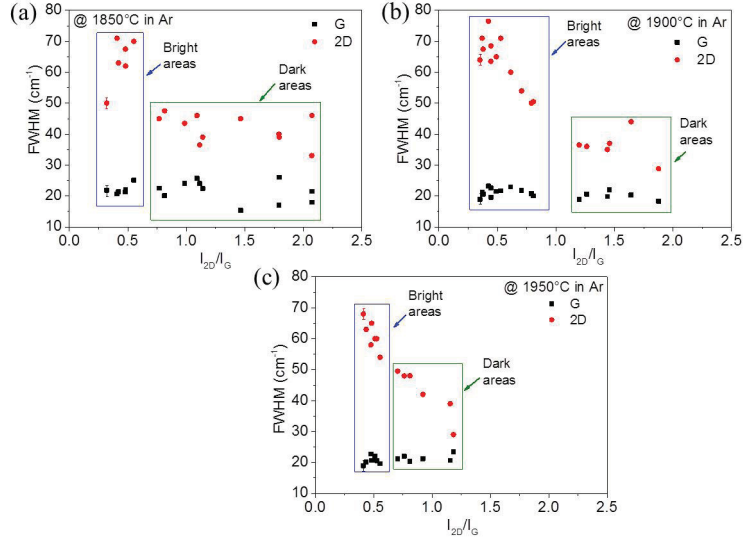


Figure 5.8: FWHM of G and 2D Raman bands as a function of the I_{2D}/I_G ratio for Gr grown at 1850° C (a), 1900° C (b) and 1950° C (c). Different optical contrast of sample regions are marked. Adapted from [229].

From the positions of the G and 2D bands maxima as a function of the I_{2D}/I_G ratio (see Fig. 5.9), no significant variation of the G band position with I_{2D}/I_G is found for the three growth temperatures, indicating a uniform doping level in each sample, independently on the lateral variations in the number of layers [133]. By contrast, a red-shift of the 2D band with increasing the I_{2D}/I_G ratio (i.e. with the number of Gr layers) is found, which is an indication of an increasing compressive strain with larger Gr thickness [233]. This is consistent with the observation of wrinkles in AFM maps.

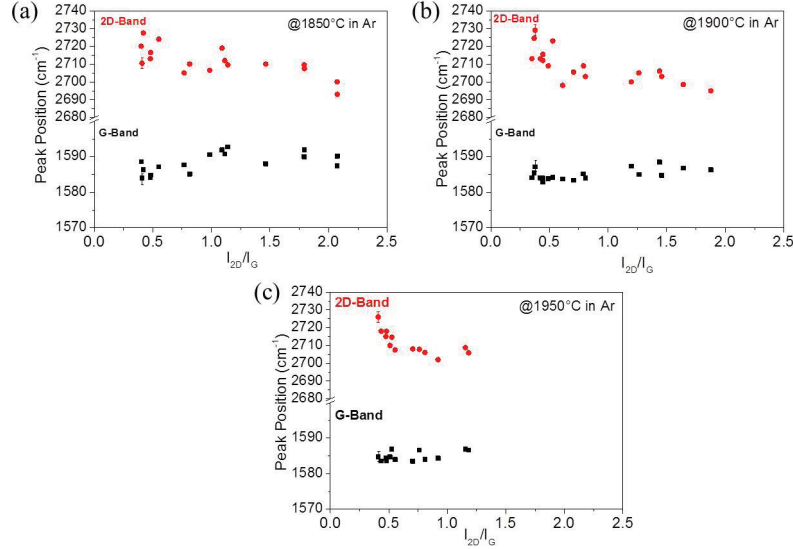


Figure 5.9: Peak positions of G and 2D Raman bands as a function of the I_{2D}/I_G ratio for Gr grown at 1850° C (a), 1900° C (b) and 1950° C (c). Adapted from [229].

In conclusion, optimized growth conditions have been adopted to obtain few layers of Gr on SiC (000 $\bar{1}$). For all the growth temperatures from 1850° C to 1950° C, Gr layers were defects-free and their coverage onto SiC was inhomogeneous. The average number of layers was found to increase with the annealing temperature. Interestingly, in addition to Gr areas with turbostratic misorientation, also Bernal stacked areas were observed. Gr doping was found to be uniform. Layers are compressively strained, with strain increasing with the layer number.

5.2 Graphene on SiO₂/Si

As mentioned in the previous chapter, Gr samples consisting of single crystalline monolayer domains were grown on copper (Cu) by chemical vapor deposition (CVD) and were transferred on a 300 nm thick SiO₂ layer on Si by using the PMMA procedure (as schematically shown in figure 1.18)

As seen in Chapter 1, one of the most promising applications of

large area and high quality graphene grown by CVD is as transparent conducting electrode for touch screens as well as for new generation photovoltaic cells [28]. In these fields graphene could compete with commonly used transparent conductive oxides (such as indium tin oxide, ITO), thanks to its high optical transparency ($\sim 97.7\%$ for a single layer) in a wide wavelength range and to its mechanical robustness and flexibility (opening the way to flexible devices applications). In this context, the main limitation of graphene with respect to ITO is represented by the relatively high sheet resistance (on the order of a few hundred ohms) of unintentionally doped single layers grown by CVD. Several strategies are currently under consideration to reduce the sheet resistance either by substitutional doping of donor or acceptor species during CVD growth [99] or by postdeposition treatments, including adsorption or physical bonding of specific atoms and molecules on Gr [234, 235, 236, 237]. In this context, it is known that p-type doping of Gr can be obtained by thermal treatments in oxygen. Notwithstanding the doping by thermal treatments is challenging because the Gr could be damaged by the high temperature annealing, and the doping effects could be unstable [95, 96, 238, 239, 240].

5.2.1 Effects of thermal treatment in an Oxygen atmosphere

In this section an experimental study on the effects of thermal treatments in molecular oxygen controlled atmosphere at temperatures lower than 350°C is reported. The study as a function of the treatment time enabled to evaluate the kinetics of the doping mechanisms and to clarify the stability by opportune thermal treatments in a vacuum. The experiments allowed to determine a stable thermally activated positive doping of $\sim 10^{13}\text{cm}^{-2}$ and to estimate a limit value for the binding energy of O_2 .

As-transferred Gr samples were preliminarily characterized by optical microscopy (OM), μ -Raman spectroscopy, and AFM operated in tapping mode (Figure 5.10). The representative OM image of Gr on SiO_2/Si reported in Figure 5.10a shows, by optical contrast, the presence of many flakes of Gr on the substrate easily distinguishable from each other for the successive point by point Raman analysis. AFM measurements of surface morphology, reported in Figure 5.10b, con-

firm the presence of flakes. Their typical size is a few microns, whereas the height changes from flake to flake as reported in the illustrative histogram of 10 regions in Figure 5.10c. By μ -Raman measurements, carried out on many representative flakes, the bands of Gr, above 1000 cm^{-1} , and those typical of silicon, below 1000 cm^{-1} , can be clearly distinguished, as reported in Figure 5.10d.

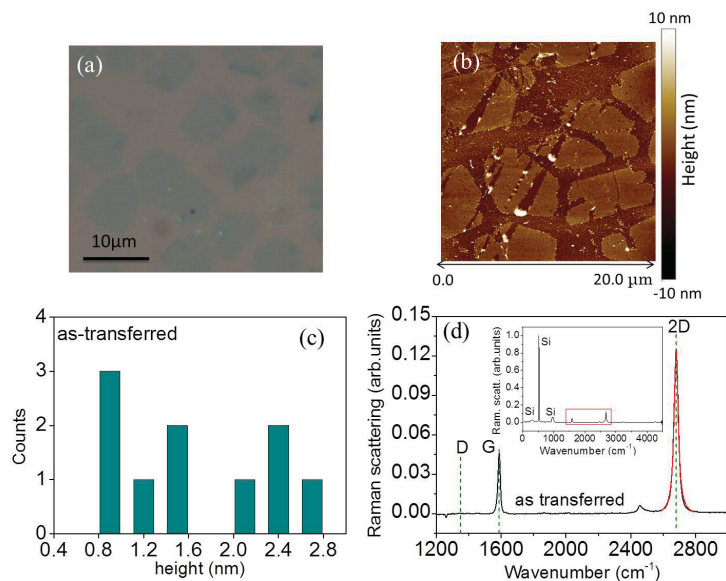


Figure 5.10: As-transferred Gr on SiO_2/Si optical image (a), AFM morphology image (b), and histogram with height of flakes statistics (c). (d) μ -Raman spectrum of Gr on SiO_2/Si focused in the spectral region of the graphene typical bands; the 2D band best fit curve with Lorentzian line shape with full width at half-maximum of $31.0 \pm 0.2\text{ cm}^{-1}$ is superimposed to the spectrum by a red line. The inset shows the complete -Raman spectrum with the Gr related bands region highlighted [241].

The G and 2D bands of Gr are located at $1584 \pm 1\text{ cm}^{-1}$ and $2679 \pm 1\text{ cm}^{-1}$, respectively. It is evident the absence of the D-band, at about 1350 cm^{-1} , indicating the high quality of the graphene layers [129]. Furthermore, the intensity ratio $I_{2D}/I_G > 2.5$, and the width ($31.0 \pm 0.2\text{ cm}^{-1}$) and shape (Lorentzian) of the 2D band, well described by a single feature, evidence the monolayer nature of graphene flakes [129]. Based on these observations, it can be hypothesized that the distribution of flakes height reported in the

Figure 5.10c arises in part from the presence of impurities or of some residual PMMA on top of some flakes, as also evidenced by the white dots distributed all over the AFM image in Figure 5.10b.

Post growth Gr thermal treatments were made in controlled atmosphere, by placing the sample in a stainless steel controlled pressure chamber (as described in Fig. 4.1 in the chapter 4). This equipment enables to fix the treatment pressure from 0.4 mbar (dynamic) up to 70 bar (static). For the thermal treatments the temperature was fixed in the $140^{\circ}\text{C}\div 350^{\circ}\text{C}$ range and was stabilized within $\pm 1^{\circ}\text{C}$. In the experiments the sample was inserted in the chamber and set to vacuum at room temperature and then, if needed, oxygen was injected at the selected pressure between 0.5 bar and 70 bar, before heating the system at the established temperature. The heating time of 5 min was fixed. The treatment time was counted after this ramp-up time. A final cooling time of 2 min to room temperature was applied in the given atmosphere (vacuum or oxygen) before to carry out the measurements in air. The employed oxygen gas was high purity, featuring highest impurity content < 3 ppm molar of H_2O . Two kinds of treatments of the sample have been applied: at a particular temperature varying the treatment time or fixing time at different temperatures between 140°C and 350°C .

As reported in Figure 5.11, the effects of the sample thermal treatments 2h in oxygen at 10 bar and 300°C are immediately observable by AFM and μ -Raman spectroscopy. By comparison of the AFM images reported in Figures 5.10b and 5.11a, we find that the white dots are now concentrated on the edges of each flake. As shown in Figure 5.11b, we also find that the flakes height distribution converges toward lower values than before thermal treatments. By comparing Figure 5.11b with its inset, it is found that this latter distribution converges toward values lower than 1.4 nm compatible with those typically observed for single layers of Gr on SiO_2/Si [242, 243]. These findings suggest the removal of the impurities or of the residual PMMA from the flakes surfaces with the contemporary decrease of the recorded height of the flakes. Furthermore, it can be seen that the flakes are not destroyed. The Raman spectrum reported in Figure 5.11c shows a blue-shift of the G and 2D bands.

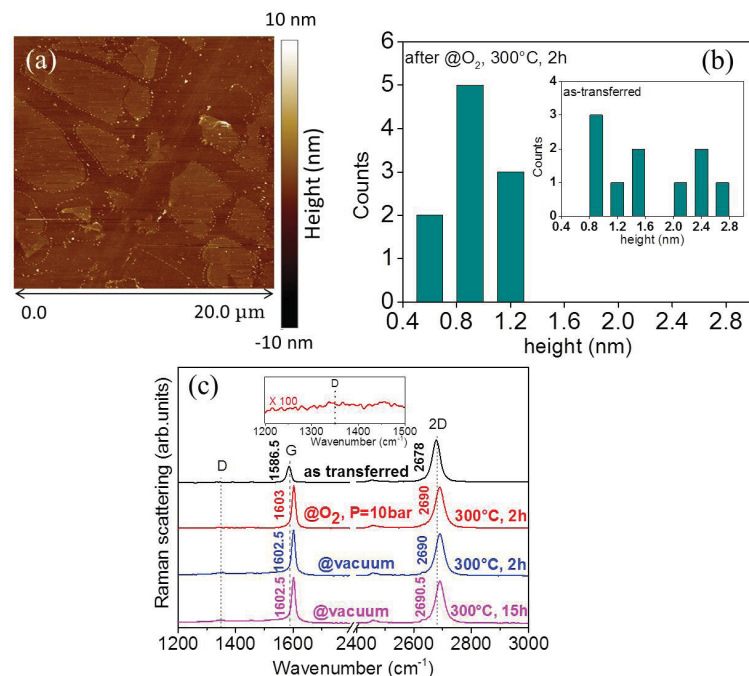


Figure 5.11: Gr on SiO₂/Si AFM morphology image (a) and histogram with height statistics of flakes (b) after 2h thermal treatment in O₂ at a pressure of 10 bar and 300° C; the inset reports the histogram with flakes height statistics of as transferred Gr on SiO₂/Si. (c) Comparison of the μ -Raman spectra of Gr on SiO₂/Si before and after 2h thermal treatment in O₂ at a pressure of 10 bar and 300° C and successively in a vacuum at 300° C for 2h and 15 h; the spectra are arbitrarily vertically shifted and are normalized at 2D band. The inset shows the magnified Raman spectrum of the O₂-treated sample to highlight the absence of the D-band even after the thermal treatment [241].

As shown in Figure 5.11, these shifts are $\sim 15^{-1}$ and ~ 10 cm⁻¹, respectively, with respect to the untreated sample; furthermore, a decrease in the ratio I_{2D}/I_G toward the value 1.1 ± 0.1 is observed. As shown in the inset of Figure 5.11c, the treatments carried out do not induce defects in the Gr as evidenced by the absence of the D-band. Comparing these results with literature data on the dependence of Gr Raman features on doping [133], and in particular the contemporary blue-shift of 2D and G bands and their intensity

ratio I_{2D}/I_G reduction, the conclusion that the treatment has induced a p-type doping of $\sim 10^{13} \text{ cm}^{-2}$ can be drawn. In details, as reported in Figures 3 and 4 of ref. [133], an I_{2D}/I_G value of about 1 is compatible with $\sim 10^{13} \text{ cm}^{-2}$ carriers concentration, and the blue-shifts of the G and 2D bands of ~ 15 and $\sim 10 \text{ cm}^{-1}$ are compatible with hole doping of the same value $\sim 10^{13} \text{ cm}^{-2}$. A successive thermal treatment in a vacuum at 300°C up to 2h, and successively up to 15h (Figure 5.11c), does not affect the changes induced by the thermal treatment in oxygen, indicating the stability of doping.

To further investigate the doping process features, we made a study of the effects of oxygen pressure. As reported in Figure 5.12, thermal treatments of a virgin sample in O_2 at 0.5 bar with the same duration and temperature as those carried out at 10 bar induce the same Raman spectral changes. In particular, as shown in Figure 5.12, measurements on different flakes of the sample show the same G and 2D bands blue-shift and bands intensity ratio (I_{2D}/I_G) decrease, proving the independence on the pressure in the investigated range.

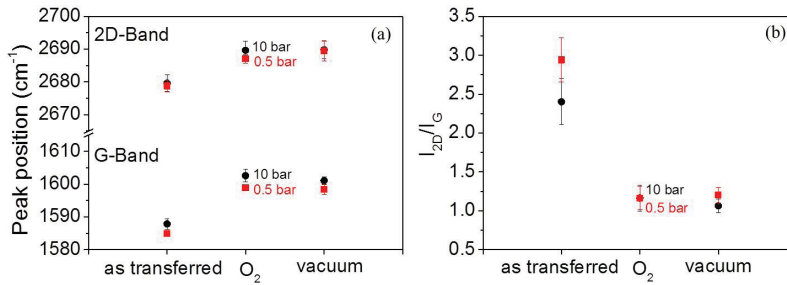


Figure 5.12: Peak positions of the G-band and 2D-band (a) and intensity ratio I_{2D}/I_G (b) of the pristine sample (as transferred), after thermal treatment of 2h at 300°C at 10 bar (circles) or at 0.5 bar (squares) of oxygen (O_2), and after successive treatment 2h in a vacuum at 300°C (vacuum). The error bars originate from a statistic of measurements on different flakes of graphene [241].

Moreover, even in this case we have checked that the induced changes are stable by applying a successive thermal treatment in vacuum at 300°C for 2h.

To determine the effectiveness of the doping process, the effect of the treatment temperature on a sample has been investigated by a

sequence of thermal treatments of 2h (isochronous) in O_2 pressure of 10 bar. As reported in Figure 5.13, the process is efficiently activated at $T > 140^\circ\text{C}$ and is completed at $T \approx 250^\circ\text{C}$.

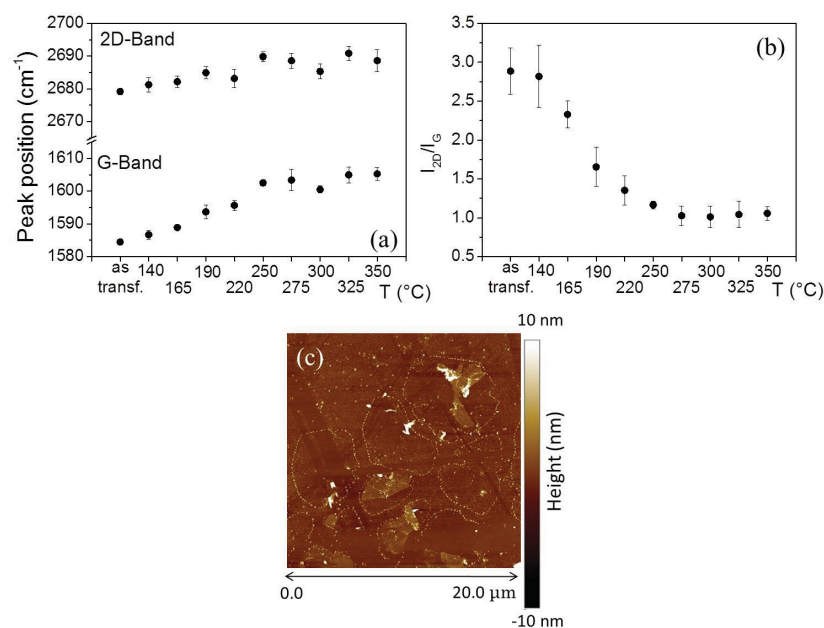


Figure 5.13: Peak positions (a) and intensity ratio (b) of the Gr μ -Raman characteristics spectral features after thermal treatments of 2h in oxygen pressure of 10 bar at various treatment temperatures. The error bars originate from a statistic of measurements on different flakes of graphene. (c) AFM morphology image after thermal treatment of 2h in oxygen pressure of 10 bar at 350°C [241].

Furthermore, the Raman bands changes for the G and 2D shifts and for their intensity ratio modification occur in a good correlated temperature range, suggesting that all these features reflect modification of Gr by the same process. The AFM analysis, reported in Figure 5.13c, shows that at $T > 300^\circ\text{C}$ Gr begins to deteriorate; indeed, the flakes recorded after 350°C treatment are smaller than the native ones and those recorded at 300°C (see Figure 5.11a) or are completely destroyed.

Once determined the temperature range of major effectiveness in the doping of graphene by treatment in fixed pressure of O_2 , the kinetics

of the process has been studied as a function of time. The temperature 250°C, when the process is completed, and 190°C, when the process is not completed, were chosen to compare these kinetics aspects and two different samples were directly treated at each temperature. As shown in Figure 5.14, for both temperatures, a blue-shift of G and 2D bands and a decrease of the I_{2D}/I_G ratio are found already after 30 min. After 1h of treatment no more changes can be observed by the Raman spectra for the given temperature, suggesting that the process arrives at thermodynamic equilibrium.

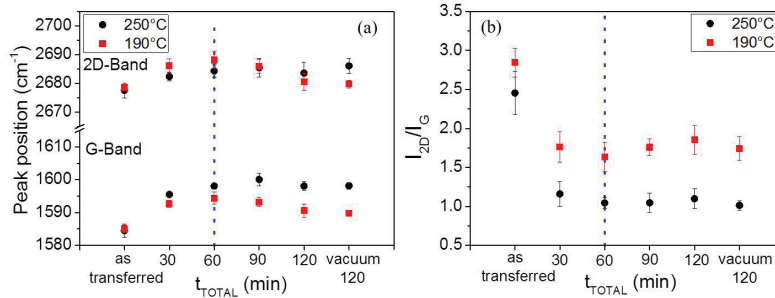


Figure 5.14: Evolution of the peak position (a) and of the intensity ratio (b) of the Gr-Raman spectral features induced by thermal treatments at two different temperatures (190°C, squares; 250°C, circles) in oxygen pressure of 10 bar by varying the treatment time. The dotted lines mark the equilibrium time. The error bars originate from a statistic of measurements on different flakes of graphene [241].

Furthermore, the changes of the spectral features differ for the different temperatures, suggesting different doping effects. It has been found, also in these cases, that the induced changes are stable by successive thermal treatments in a vacuum. These kinetics aspects enable to conclude that the data previously reported in Figure 5.13 are related to equilibrium states specific of each given temperature since each of those experiments were done in 2h, a time long enough to reach a stationary state, and that many different equilibrium states exist for oxygen doping. In details, no stable doping population is expected for treatments below 140°C nor increment of doping above 250°C, since at low temperature no spectral changes are induced, whereas at high temperature the process is completed and again no spectral changes occur. By contrast, some destroying occurs above

300°C, as above-reported by AFM. At the same time the maximum changes are observed at about 200°C, where it can be theorized that the maximum density of stable doping configurations is located. To schematize these features, a distribution of stable configurations as a function of configuration energy can be pictorially suggested as reported in Figure 5.15.

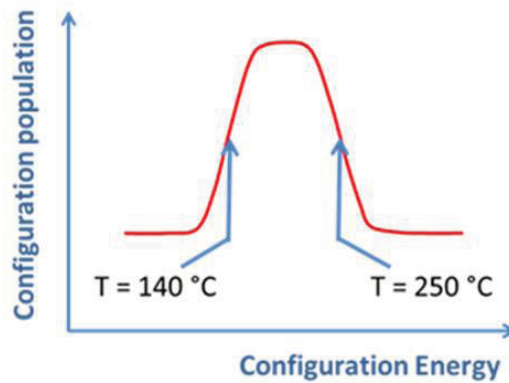


Figure 5.15: Schematic distribution of stable doping states population as a function of energy. The temperatures reported in the scheme represent the onset and completion process temperature determined experimentally. Adapted from [241].

This distribution can be explored by the thermal equilibrium population change. In details, below 140°C no stable states can be populated, at about 250°C the population density decreases and between these temperatures a maximum density is found. The temperature dependence of the process of doping reconstructed through the Raman measurements and reported in Figure 5.13 suggests that this is an energy activated process.

By the analysis of hole concentration versus temperature derived from the data reported in Figure 5.13, and using the doping concentration estimation from Raman features suggested in the literature [133], an Arrhenius plot can be constructed.

As reported in Figure 5.16, a quite good linear dependence of hole concentration on T^{-1} is found. From the best fit curve of these data an activation energy for the doping process $E_a = 56 \pm 8$ meV is found.

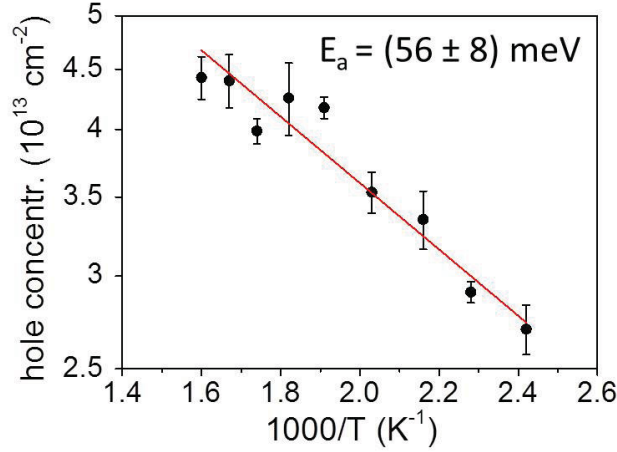


Figure 5.16: Arrhenius plot of the hole concentration estimated from the Raman features. The best fit line gives an activation energy for the doping process $E_a = 56 \pm 8$ meV [241].

5.2.2 Aging effect

Our intention, at this point, has been to evaluate the temporal stability of doping that, as noted in the literature and as previously described in Chapter 1, may not be extended in time. So we have prepared a sample by doping it in oxygen atmosphere and we have investigated it over time. As seen in figures 5.10 and 5.14, the as transferred monolayer Gr has been characterized by AFM and μ -Raman measurements and to induce changes in the native Gr a sample has been subjected to a thermal treatment at 250°C for 2h in O₂ at 10 bar that is able to modify its features. As shown in Fig. 5.17, it is observed that the 2D and G Raman bands have a blue shift of about 10 cm⁻¹ and 15 cm⁻¹, respectively, after the thermal treatment. In addition, the band amplitude ratio decreases to $I_{2D}/I_G = 1.1 \pm 0.1$. These features are compatible with a p-type doping of graphene [133]. The successive thermal treatment at 250°C in vacuum does not change the induced spectral modifications within the experimental errors, showing that the oxygen exposure stably modified the Gr properties.

By contrast, as shown in 5.17, keeping the sample in ambient atmosphere for a month induces a tendency to red shift the position of the 2D band and induces a clear red shift of about 10 cm⁻¹ of the G

band. Concurrently, the I_{2D}/I_G ratio increases towards 2 ± 0.1 with a tendency to recover the value observed before the treatments.

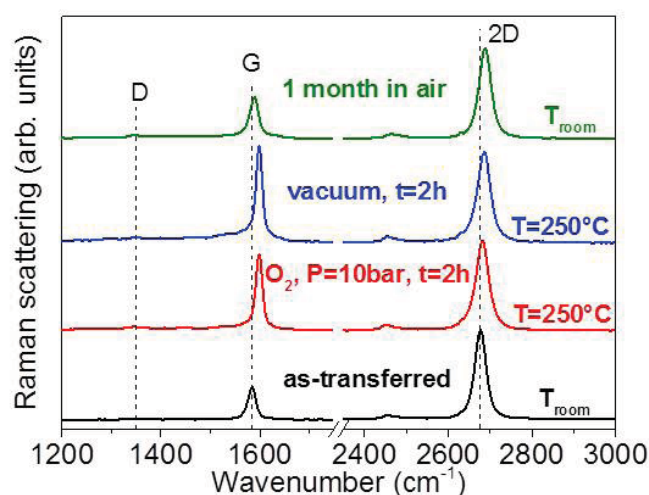


Figure 5.17: μ -Raman spectra of the as transferred graphene sample, after thermal treatments at 250°C in O_2 and successively in vacuum, and after 1 month in ambient atmosphere at room temperature. Spectra have been arbitrarily vertically shifted for clarity [244].

To further explore the stability of the oxygen-induced modifications, a sample has been thermally treated 2h at 300°C in O_2 at 10 bar. The spectra shown in Fig. 5.18 show that the 2D and G bands undergo a blue shift of about 10 cm^{-1} and 14 cm^{-1} , respectively, very similar to those obtained at 250°C , and the amplitude ratio is 1. The successive treatment in vacuum does not affect the changes, whereas the permanence of the sample 6 months in air gives rise to a red shift of about 10 cm^{-1} for the G band and of about 1 cm^{-1} for the 2D. At the same time the I_{2D}/I_G recovers the value 2.5.

These findings, together with the previous ones at 250°C , evidence that even if the oxygen molecules are trapped in sites from which they are not easily released, as they keep staying up to 300°C , the O_2 could react with species present in air or could be affected by their presence in the neighborhood.

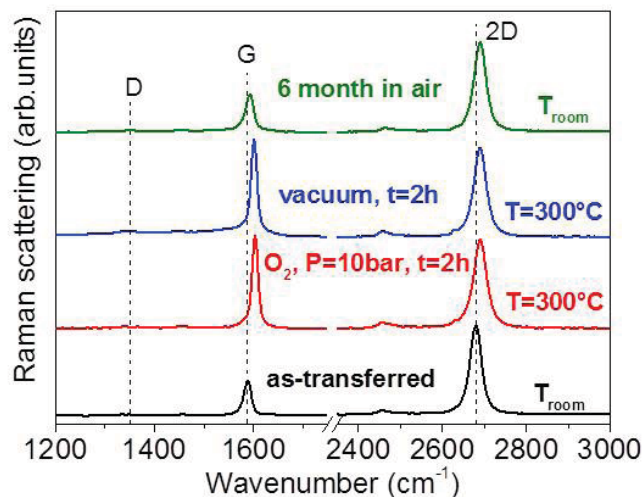


Figure 5.18: μ -Raman spectra of the as transferred graphene sample, after thermal treatments at 300°C in O_2 and successively in vacuum, and after 6 months in ambient atmosphere at room temperature. Spectra have been arbitrarily vertically shifted for clearness [244].

To differentiate between the role of molecular air gases and Gr morphological effects, as suggested in literature [98], a sample thermally treated in oxygen for 2 h at 300°C in O_2 at 10 bar was successively maintained under vacuum (0.7 mbar) for 1 month in a drier at room temperature. As shown in Fig. 5.19, the changes thermally induced in the Raman spectra are almost completely maintained, in particular for the bands spectral shifts, evidencing that, for the perturbation of the changes induced by the treatment in oxygen, a prominent role is played by gas molecules present in the air atmosphere and not by Gr morphology recovery induced at room temperature.

Finally, as shown in Fig. 5.20, an O_2 thermally treated sample also aged in air at room temperature has been successively thermally treated in O_2 for 2h at 320°C and 10 bar. It is found that a second treatment in oxygen induces the complete recovery of the effects of the first treatment in oxygen. In particular, the blue shifts of the 2D and G bands are confirmed as well as the amplitude ratio I_{2D}/I_G decrease.

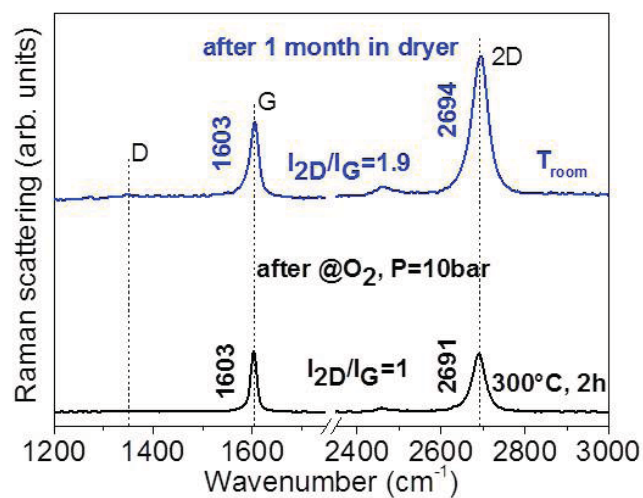


Figure 5.19: μ -Raman spectra of a graphene sample thermally treated at 300°C in O_2 for 2h at 10 bar and successively maintained in 0.7 mbar vacuum at room temperature for a month [244].

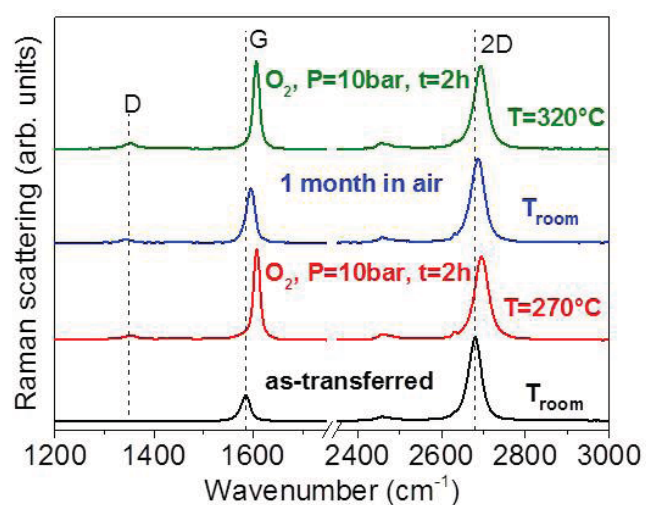


Figure 5.20: μ -Raman spectra of as transferred graphene sample, thermally treated at 270°C in O_2 for 2h at 10 bar, successively aged in air 1 month and finally thermally treated at 320°C in O_2 for 2h at 10 bar. Spectra have been arbitrarily vertically shifted for clearness. Adapted from [244]

These results show that air molecular gases perturb the sites where oxygen is trapped by the first thermal treatment, and a successive exposure to O₂ removes these molecules restoring the doping effect.

5.2.3 Effects of thermal treatment vs. Atmosphere

As we have just seen, in figures 5.17 and 5.20, the sample that was left in air for 1 month shows spectral characteristics much similar to those of the as-transferred sample. By contrast, the sample kept in vacuum for 1 month, as shown in Fig. 5.19, has G and 2D bands positions similar to those of the sample after the O₂ thermal treatment and features a partial recovery of the I_{2D}/I_G ratio. This comparison suggests a role of the atmosphere on the effect of doping release. To deepen the understanding of the role of the air atmosphere, thermal treatments on samples of Gr/SiO₂/Si have been carried out by varying the gas environment. In details, N₂ or CO₂ have been considered since they are among the main components of atmospheric air, apart from Ar and H₂O. A first thermal treatment was done in O₂ at a pressure of 2 bar for 1h at a temperature of 290°C. As reported in Fig. 5.21, and in Table 5.21, after this thermal treatment the G band blue shifts 19 cm⁻¹, the 2D band blue shifts 15 cm⁻¹, and their amplitude ratio decreases to 1.4. Overall these changes are compatible with a hole doping of ~10¹³ cm⁻² [133]. Additional thermal treatment in O₂ for 1h shows that doping equilibrium is reached just after the previous first hour of treatment since no further spectral modifications occur. The successive thermal treatment is done in N₂ at a pressure of 2 bar for 2h at 290°C. This treatment does not induce relevant changes in the G and 2D bands features suggesting that the effects obtained by doping are maintained. In the spectra analysis it is observed, nevertheless, the appearance of a shoulder of the G band on its low wavenumber side that does not affect the band amplitude relative to the 2D band after subtraction of an opportune background. As recently suggested, this feature can be attributed to defectiveness induced on Gr [245, 246].

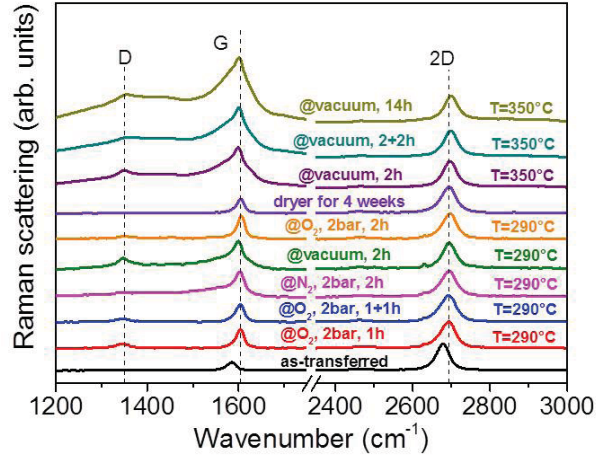


Figure 5.21: μ -Raman spectra of a Gr/SiO₂/Si sample that has undergone a sequence of thermal treatments at 290° C in O₂, N₂ and vacuum, a permanence at room temperature in vacuum inside a dryer and then another sequence of treatments at 350° C. For each treatment the gas, pressure, and duration time are shown. The spectra are normalized to the amplitude of the 2D band and are arbitrarily vertically shifted [247].

After this treatment, a vacuum treatment was done at 290° C that, as reported in Fig. 5.21, produces minor effects and some increase of the D band at 1350 cm⁻¹ and some widening of the G band, as reported in Table 5.1. On this same sample a treatment in O₂ at 2 bar for 2h at 290° C is then executed. The effect of this treatment is the recovery of the spectral features towards the p-type doped sample spectral features.

In particular, as shown in Fig. 5.21, and reported in Table 5.1, the G and 2D bands positions and their relative amplitudes are very similar to those obtained after the first treatment in O₂, supporting the recovery of doping and suggesting that O₂ could remove defectiveness introduced by N₂ and vacuum treatments. As recently reported [246], it can be suggested that defective sites, which are more unstable than sp² graphene sites, are more efficient in reaction with oxygen and then they are removed in presence of O₂ giving rise to further doping.

Treatment	G-Band position cm^{-1}	FWHM G-Band cm^{-1}	2D-Band position cm^{-1}	FWHM 2D-Band cm^{-1}	I_{2D}/I_G
As-transferred	1585.0 ± 1.0	22.7 ± 0.3	2678.0 ± 1.0	39.4 ± 0.2	3.2 ± 0.1
@O ₂ 2 bar, 1h, 290°C	1604.0 ± 1.0	20.8 ± 0.2	2693.0 ± 1.0	47.5 ± 0.4	1.4 ± 0.1
@O ₂ 2 bar, 1h+1h, 290°C	1604.0 ± 1.0	23.0 ± 0.3	2692.5 ± 1.0	50.4 ± 0.4	1.5 ± 0.1
@N ₂ 2 bar, 2h, 290°C	1602.5 ± 1.0	23.3 ± 0.3	2694.0 ± 1.0	47.4 ± 0.3	1.4 ± 0.1
@vacuum, 2h, 290°C	1600.0 ± 1.0	29.4 ± 0.6	2694.5 ± 1.0	39.6 ± 0.2	1.3 ± 0.1
@O ₂ 2 bar, 2h, 290°C	1606.0 ± 1.0	19.0 ± 0.2	2696.5 ± 1.0	43.8 ± 0.3	1.1 ± 0.1
Dryer for 4 weeks	1604.5 ± 1.0	20.3 ± 0.3	2695.0 ± 1.0	45.4 ± 0.2	2.0 ± 0.1
@vacuum 2h, 350°C	1599.5 ± 1.0	37.7 ± 1.0	2696.5 ± 1.0	40.9 ± 0.2	1.0 ± 0.1
@vacuum 2h+2h, 350°C	1601.0 ± 1.0	34.1 ± 0.5	2698.5 ± 1.0	40.7 ± 0.2	1.0 ± 0.1
@vacuum 14h, 350°C	1602.0 ± 1.0	47.7 ± 0.9	2700.0 ± 1.0	40.9 ± 0.3	0.6 ± 0.1

Table 5.1: Fitting parameters of the Raman spectra reported in Fig. 5.21. Adapted from [247].

The same sample of Gr/SiO₂/Si was then kept 1 month in vacuum (inside a dryer pumped twice a day down to $7 \cdot 10^{-1}$ mbar) at room temperature and subsequently was subjected to thermal treatments in vacuum ($5 \cdot 10^{-8}$ bar) at higher temperature ($T = 350^\circ\text{C}$). The Raman spectra, reported in Fig. 5.21, show that the vacuum is able to maintain the doping effect also after cyclic exposure of the sample to different gases, whereas the high temperature treatment in vacuum causes defectiveness in the sample, without strongly destroying it, since the flakes are still clearly detected by Raman microscope [245, 246]. These overall results suggest that O₂ treatment is able to induce doping of Gr and this latter is not affected by nitrogen nor by vacuum at room temperature and up to about 300°C. Higher temperature

starts to modify the morphology of Gr inducing defective structures and overwhelming the doping estimation by Raman measurements. It is worth to underline that all the tests reported have been done at high temperature in order to accelerate or favour any reactive process that could happen at room temperature.

To better clarify the instability in air at room temperature of the oxygen induced doping of Gr, a sample of Gr/SiO₂/Si, was treated in CO₂ at 2 bar for 2 h at 290°C after carrying out a thermal treatment in O₂ at 2 bar for 2 h at 290°C. Comparison of the Raman spectra of this sample is shown in Fig.5.22.

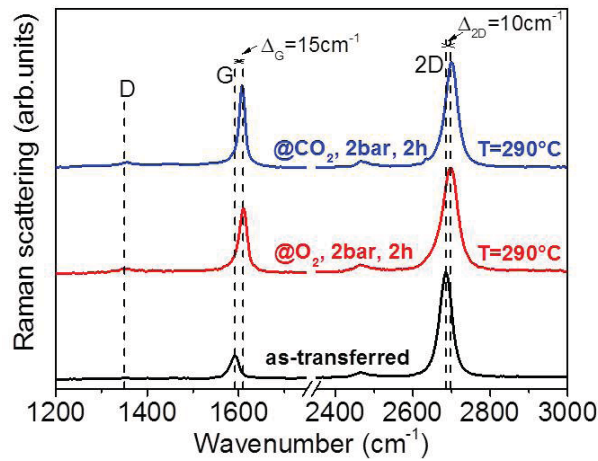


Figure 5.22: μ -Raman spectra of an as grown sample of Gr/SiO₂/Si and of samples thermally treated first in O₂ at a pressure of 2 bar and $T = 290^\circ\text{C}$ (red curve) and then in CO₂ at a pressure of 2 bar and $T = 290^\circ\text{C}$ (blue curve). The spectra have been vertically shifted after normalization with respect to the 2D band [247].

It is noted that the effect of doping obtained in O₂ is not affected by the successive treatment in CO₂. This result and the previous one related to N₂ treatment enable us to suggest that the instability at room temperature of the O₂ induced doping is mainly due to atmospheric water. In particular, since a treatment up to about 300°C in vacuum does not change the doping effect it can be hypothesized that oxygen is physically trapped and is not easily released. The successive exposure to water at room temperature could induce a reaction of

the oxygen trapped nearby Gr modifying this latter molecule doping efficiency.

As a further experiment we considered the possibility to separate the effect of strain from doping in graphene treated at high temperature, as suggested in literature [98, 140]. To this aim selective thermal treatments in vacuum, or N_2 , or CO_2 , or O_2 have been carried out in different samples of Gr/SiO₂/Si at the temperature 290°C, when high efficiency of doping is suggested by the previous experiments. As reported in Fig. 5.23, and summarized in Table 5.2, the treatments of a sample in vacuum, induce some blue shift of the 2D and G bands and also a decrease of the I_{2D}/I_G amplitude ratio as compared to the as transferred sample.

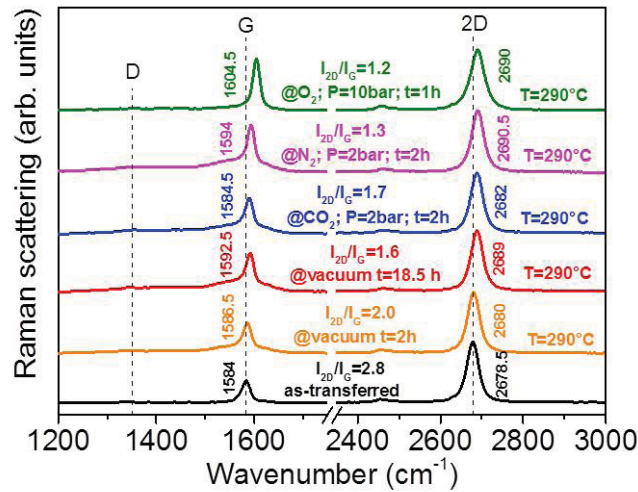


Figure 5.23: μ -Raman spectra of an as grown sample of Gr/SiO₂/Si and of samples thermally treated selectively in vacuum, or in N_2 , or in CO_2 or in O_2 at $T = 290^\circ C$. The spectra have been vertically shifted after normalization with respect to the 2D band [247].

Furthermore, these treatments induce the appearance of a shoulder to the G band on its low wavenumber side. Similar results are found for treatments in N_2 or in CO_2 .

Treatment	G-Band position cm^{-1}	FWHM G-Band cm^{-1}	2D-Band position cm^{-1}	FWHM 2D-Band cm^{-1}	I_{2D}/I_G
As-transferred	1584.0 ± 1.0	20.4 ± 0.1	2979.0 ± 1.0	33.0 ± 0.2	2.8 ± 0.1
@vacuum, 2h, 290°C	1586.5 ± 1.0	18.9 ± 0.1	2680.0 ± 1.0	33.5 ± 0.2	2.5 ± 0.1
@vacuum, 15.5h, 290°C	1591.5 ± 1.0	17.2 ± 0.2	2689.0 ± 1.0	33.7 ± 0.2	2.2 ± 0.1
@CO ₂ 2 bar, 2h, 290°C	1590.0 ± 1.0	18.6 ± 0.1	2688.5 ± 1.0	34.6 ± 0.2	2.2 ± 0.1
@N ₂ 2 bar, 2h, 290°C	1594.0 ± 1.0	16.6 ± 0.1	2690.0 ± 1.0	34.3 ± 0.1	1.7 ± 0.1
@O ₂ 10 bar, 1h, 290°C	1604.5 ± 1.0	16.5 ± 0.2	2690.0 ± 1.0	40.3 ± 0.2	1.2 ± 0.1

Table 5.2: Fitting parameters of the Raman spectra reported in Fig. 5.23. Adapted from [247]

At variance, in the case of the O₂ treatment the Raman bands shift towards the blue is maximum as well as the decrease of the I_{2D}/I_G ratio without any presence of the shoulder to the G band. These effects could overall be related to induced strain and defectiveness of the Gr layer arising from the interaction with the substrate due to differences in their thermal expansion coefficients that in the case of oxygen treatment are mitigated and overwhelmed by the doping effect, probably driven by the same Gr/ substrate interaction. To further strengthen this qualitative evaluation a correlation map between 2D and G band peak positions is obtained [98, 140, 248]. In particular, the same slopes of 2D peak position (POS(2D)) vs G peak position (POS(G)) introduced in Ref. [98] have been used to identify strain and doping lines in the map, and in details the slopes are: 2.45 and 0.7, respectively. As reported in Fig. 5.24, all the samples apart from the O₂ treated one stay near to the strain line obtained for 2.33 eV Raman laser in the Pos(G)-Pos(2D) space [98].

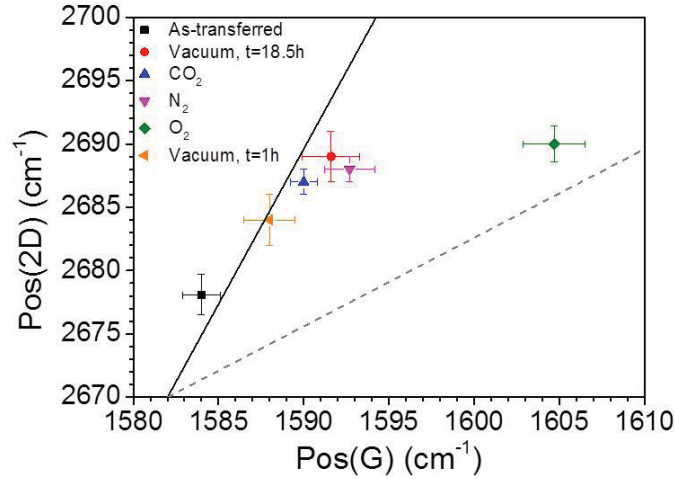


Figure 5.24: Correlation map of the 2D and G peak positions in the Gr/SiO₂/Si samples as transferred and thermally treated selectively in vacuum, or in N₂, or in CO₂ or in O₂ at T = 290° C. The black solid line marks the strain limit (slope 2.45) and the grey dashed line the doping limit (slope 0.7), as reported in Ref. [98]. Adapted from [247].

By contrast the O₂ treated sample is very near to the doping line supporting the drawn conclusion of p-doping effect by this treatment. To quantitatively estimate strain and doping levels we applied the same procedure reported in Ref. [98]. In particular, the shift of the G band position with respect to the strain line has been used to evaluate the doping level, whereas the shift of the 2D band position with respect to the doping line has been used to evaluate the strain. Furthermore, as suggested in Ref. [98], we corrected the G band position shift by the same third order polynomial to compensate the extra anharmonic phonon contribution to the shift before to evaluate the final doping or strain. The maximum 2D shift of 12 cm⁻¹ has been found, and the maximum G shift of 14.5 cm⁻¹, giving a compressive strain of 0.15% and a p-doping of 10¹³ cm⁻². It is worth to notice that this latter value is in agreement with that estimated basing on 2D and G bands shift and their amplitude values ratio using Ref. [133] and previously reported and, as can be expected basing on general considerations, on band shift induced by different charges nearby Gr [135]. Furthermore, the strain is of the same order of magnitude as those found by the

2D, G bands shifts, 0.3%, 0.2%, respectively, using the Grüneisen parameters reported in Ref. [141] and the points on the strain line of Fig. 5.24.

These results enable to conclude that the thermal treatment in oxygen atmosphere is an efficient route to produce p-doped graphene layers on SiO₂. In addition, the effect reported in Ref. [249] on the substrate role could in part be the origin of the here reported findings, notwithstanding it is worth to observe that treatments in vacuum, N₂, CO₂, as reported in Fig. 5.23, are not effective in inducing blue shifts of G, 2D bands and decrease of I_{2D}/I_G as large as in the case of oxygen. This latter molecule gives the largest shifts and the largest amplitude ratio decrease of 2D, G bands.

To deepen the understanding of possible changes induced on Gr/SiO₂/Si by the thermal treatments carried out, XPS² measurements have been executed on an as-transferred sample, on a sample thermally treated 2h at 290°C in dynamic vacuum of $5 \cdot 10^{-8}$ bar and on a sample thermally treated 2h in 2 bar of O₂ at 290°C. The Raman measurements give the same results reported in Figs. 5.21 and 5.23 for the same kind of treatments. As shown in Fig. 5.25, many characteristic XPS peaks are found. The spectral features at 45° incidence reported in Fig. 5.25(a) are in agreement with a graphene C1s spectrum (284.1 ± 0.1 eV, asymmetric; main plasmon resonance at 289.6 ± 0.1 eV) overlapping with carbon atoms in PMMA or other C–O/C=O groups at 284.8 ± 0.1 eV, 285.7 ± 0.1 eV, 286.4 ± 0.1 eV, 288.9 ± 0.1 eV [246, 250]. The measurements in Fig. 5.25(a) evidence that the as-transferred Gr/SiO₂/Si features residual PMMA, in agreement with AFM measurements above reported. By vacuum thermal treatment at 290°C a partial removal of PMMA can be observed, without strong modification of sp² C, as already reported [246]. By contrast, the thermal treatment in O₂ strongly affects the PMMA bands, almost completely removing them and recovering the largest contribution to sp² C. This result is also in agreement with AFM measurements, and evidences a role of O₂.

²X-ray Photoelectron Spectroscopy. The measurements were carried out in collaboration with Prof. B. Pignataro and Dr. M. Scopelliti at University of Palermo

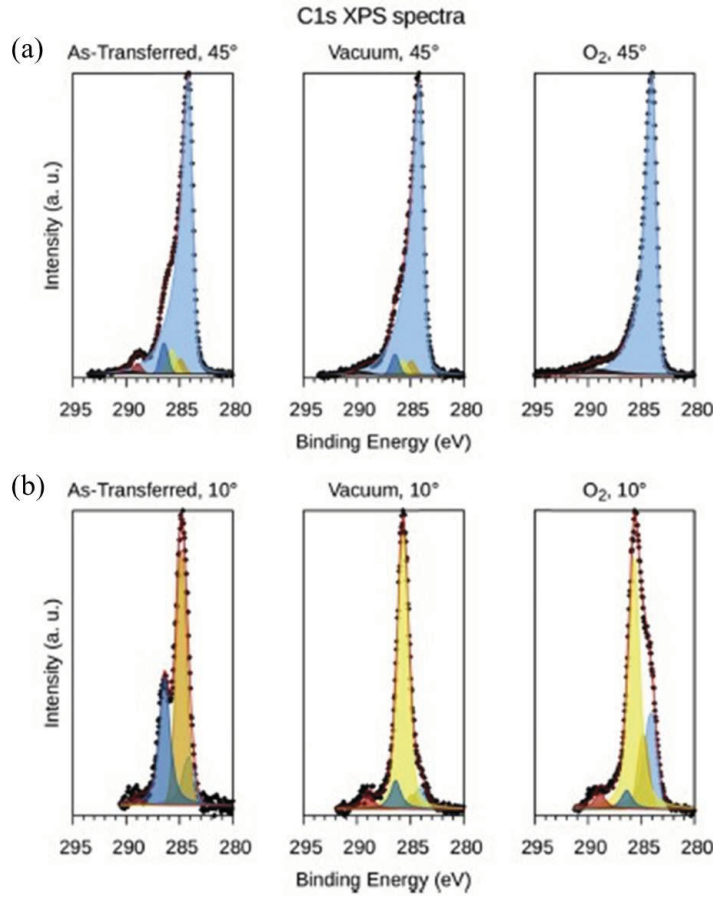


Figure 5.25: XPS spectra at 45° (a) and 10° (b) take off angle of C1s core level of the as transferred Gr/SiO₂/Si (As-Transferred), of Gr/SiO₂/Si thermally treated 2h in vacuum at T = 290° C (vacuum), and Gr/SiO₂/Si thermally treated 2h in 2 bar O₂ at T = 290° C (O₂). The shadowed curves are best fit peaks, red line is their sum and circles are experimental points. Best fit peaks are located at 284.1 ± 0.1 eV (asymmetric lineshape, Gr); 284.8 ± 0.1 eV (C-C/C-H); 285.7 ± 0.1 eV and 286.4 ± 0.1 eV (C-O); 288.9 ± 0.1 eV (C=O); 289.6 ± 0.1 eV (graphene plasmon resonance) [246, 250]. Adapted from [247].

The concomitant changes in the Raman spectra above reported, giving maximum blue shift of G, 2D bands and the decrease of I_{2D}/I_G ratio for O₂ treatments testify the doping induced by this treatment.

At variance, the XPS spectra after vacuum show that minor effects are induced on residual PMMA suggesting that the changes found by Raman could be attributed to strain as above shown. By the measurements at 10° take off reported in Fig. 5.25(b), sampling a shallower portion of the Gr/SiO₂/Si system, it is found that the as-transferred sample features a strong band system attributable to C–C/C–H, C–O and C=O bonds, almost completely covering the Gr signal (and thus, as expected, no plasmon resonance was observable). Vacuum treatment enhances the non-Gr signals, while the O₂ treatment reduces this superficial contamination of Gr. As expected, combining these results with measurements at 45° take off angle it could be guessed that the native sample is characterized by groups other than Gr dispersed on the overall sample surface and more evident by shallower measurements (10° take off angle measurements). These results together with Raman measurements enable to conclude the effectiveness of O₂ process and that it does not affect the lattice structure of Gr, but accelerates the removal of spurious contributions and accelerates doping.

Finally, to deepen the understanding of the instability in ambient atmosphere at room temperature of O₂ Gr p-doping and the hypothesis that water molecules present in air cause this instability since, as above reported, nor N₂ nor CO₂ induce the ambient observed changes, a specific treatment in water was carried out. In details, a Gr/SiO₂/Si was preliminarily treated at 290°C in O₂ at 2 bar for 2h to get doping, afterwards the sample was treated in a mixture of He and H₂O steam in a Parr reactor at 150°C for 2h (as described in the previous chapter), this temperature being chosen since it gives minor strain/doping effects as previously reported. As shown in Fig. 5.26, the treatment in oxygen gives the Raman spectral changes attributed to doping: 2D, G bands maximum blue shift and I_{2D}/I_G ratio decrease down to 1.2. By contrast, the successive treatment in H₂O gives an almost complete recovery of the as grown sample Raman features.

These findings strongly support the attribution to water molecules contained in air of the responsibility to contrast the doping induced by O₂, further studies are needed to clarify the microscopic features of this effect and its dynamics, useful aspects to tune the oxygen doping.

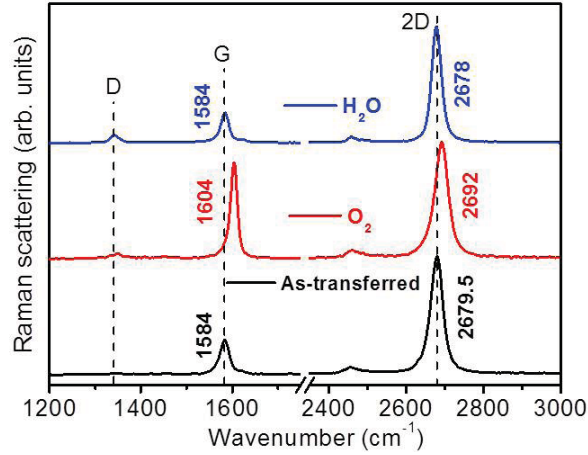


Figure 5.26: μ -Raman spectra of an as transferred sample of Gr/SiO₂/Si and of a sample thermally treated in 2 bar O₂ at $T = 290^\circ\text{C}$ for 2h (O₂), and successively in 2 bar of H₂O steam at 150 $^\circ\text{C}$ for 2h. The spectra have been vertically shifted after normalization with respect to the 2D band [247].

5.2.4 In situ study of thermal effects on Gr

To try to better understand the doping and strain processes occurring by thermal treatments a dedicated in-situ experiment has been carried out. As we discussed in Chapter 4, the in situ treatment consists in performing heat treatments and do the Raman measurements simultaneously. As reported in Fig. 5.27a, AFM measurements show that the used samples are characterized by Gr flakes of dimension $>10\ \mu\text{m}$. The as-transferred Gr has been characterized by μ -Raman measurements. As shown in Fig. 5.27b, the 2D band at $(2677\pm 1)\ \text{cm}^{-1}$ and the G band at $(1585\pm 1)\ \text{cm}^{-1}$ can be recorded with an amplitude ratio $I_{2D}/I_G \sim 3.2$. Furthermore, no detectable D band is found in the spectral region at about $1350\ \text{cm}^{-1}$. In addition, the full width at half maximum (FWHM) of the 2D band is $(35\pm 1)\ \text{cm}^{-1}$. Both the AFM and the Raman measurements evidence the mono-layer properties of the employed Gr and its low defect content [129].

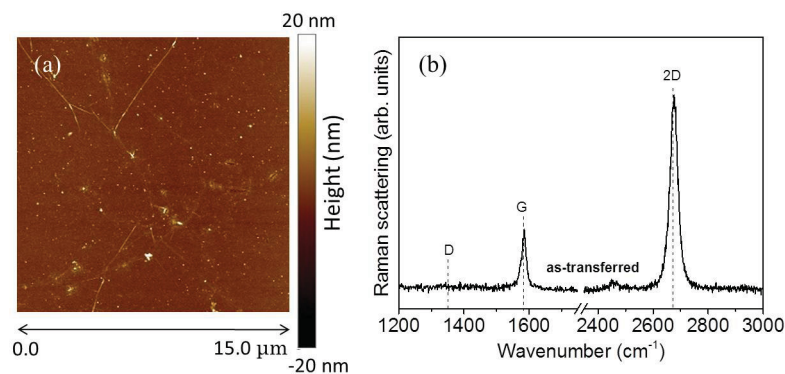


Figure 5.27: (a) AFM morphology image and (b) μ -Raman spectra of the as transferred graphene on SiO_2 substrate on Si.

To evaluate the effects of temperature and try to follow the changes in the Raman spectrum during thermal treatments, we made two experiments with in-situ measurements. The first experiment was done in air varying the temperature in 50°C steps from 100°C up to 300°C and maintaining each single temperature for 30 minutes during Raman measurements, executed every 5 minutes. As shown in Fig. 5.28, we can see a clear increase in the FWHM of the 2D band with increasing temperature (attributable to thermal effect). In details, the FWHM features a stable increased value up to 200°C , and a further increase at 250°C , the FWHM returning to be like that of the as-transferred sample on returning to room temperature. It is also observed that there is not any evident shift of the 2D band peak position, and a small blue shift of the G band. In addition, we found the appearance of a shoulder on the low wavenumber side near the G-band above 200°C . Furthermore, starting from 150°C we observed a change in the amplitude ratio of the 2D and G bands, I_{2D}/I_G , with a tendency to decrease. After cooling the sample to room temperature (top spectrum in Fig. 5.28) a permanent blue shift of the G (13 cm^{-1}) and of the 2D (13 cm^{-1}) bands, and a decrease of their ratio from 3.4 down to 1.4 is found.

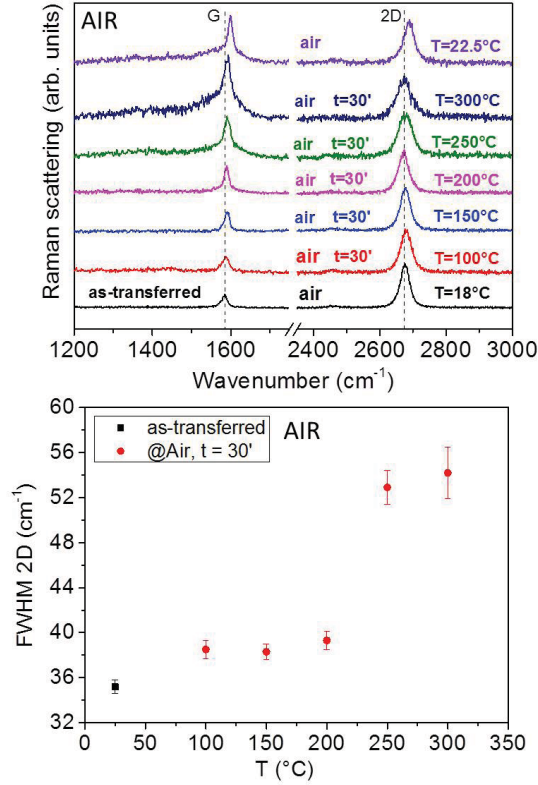


Figure 5.28: (Top) Comparison of the in-situ Raman spectra of a Gr sample as-transferred and subsequently treated in air, the temperature varies from 100° C up to 300° C. The reported time is the elapsed time from the treatment beginning at the given temperature, the top spectrum is acquired after decreasing the temperature. Spectra have been arbitrarily vertically shifted for clearness. (Bottom) Trend of the FWHM of the 2D band as a function of temperature.

The second experiment with in-situ measurements was made by thermal treatments in 2 bar of oxygen atmosphere at 300° C, up to one hour and, successively, at 350° C for an additional hour. This choice is determined by the above reported temperature value inducing major observable spectral changes and by the previously reported study about the doping effects as a function of temperature in similar samples, showing a larger effectiveness of doping at these temperatures. As shown in Fig. 5.29, also in this case we see the thermal effect with

a larger increase in the FWHM of the 2D band, compared to that observed in the air, without its shift in-situ. Again a decrease of the I_{2D}/I_G bands amplitude ratio down to 1.1 is observed in-situ. Also in this case, cooling the sample to room temperature (top spectrum in Fig. 5.29) a blue shift of the G and 2D bands (of 20.5 and 18 cm^{-1} , respectively) is detected, and this latter band FWHM returns to be like that recorded for the as-transferred sample.

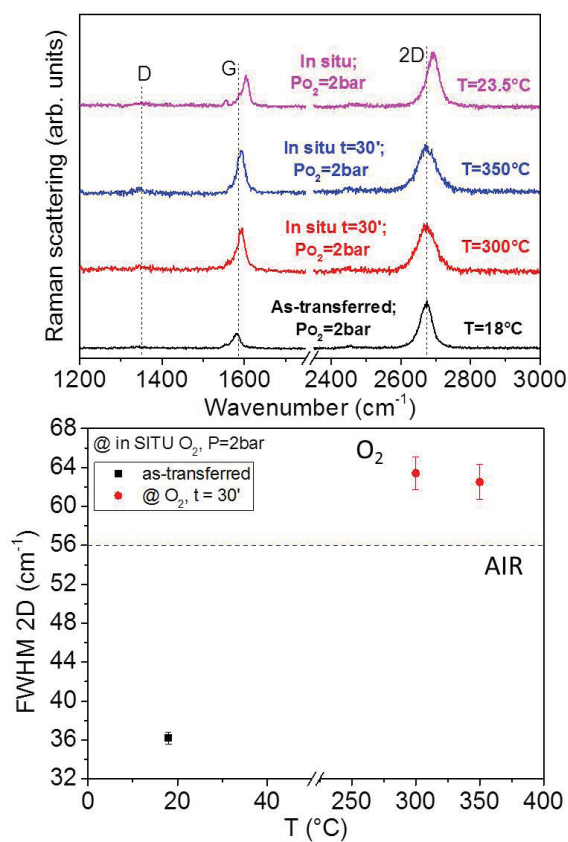


Figure 5.29: (Top) Comparison of the in-situ Raman spectra of a Gr sample as-transferred and subsequently treated in O_2 , at a pressure of 2 bar and at the temperatures of 300°C and 350°C . The reported time is the elapsed time from the treatment beginning at the given temperature. Spectra have been arbitrarily vertically shifted for clearness. (Bottom) Trend of the FWHM of the 2D band as a function of temperature. The dashed line indicates the maximum value of the FWHM of the 2D band obtained by the treatment in air (see Fig. 5.28).

By a comparison of the treatment in O_2 with the sample treated in air, we note a greater shift of the G and 2D bands, indicating an additional doping effect induced by the exposure to only oxygen [133]. Furthermore, on returning to room temperature we observed an increase of the ratio I_{2D}/I_G probably caused by the high temperature reached, that could induce more changes in the graphene properties as its deterioration. Similarly to what is found in the literature [98] and as we have done previously, we report, in Fig. 5.30, a map of the 2D band position as a function of the G band position to evidence doping and stress effects. As shown in the figure, the sample which has undergone a treatment in oxygen is closer to the line of doping than to the strain line, obtained by a Raman laser with 2.33eV energy, supporting the conclusion made on the doping of p-type obtained by treatment in O_2 .

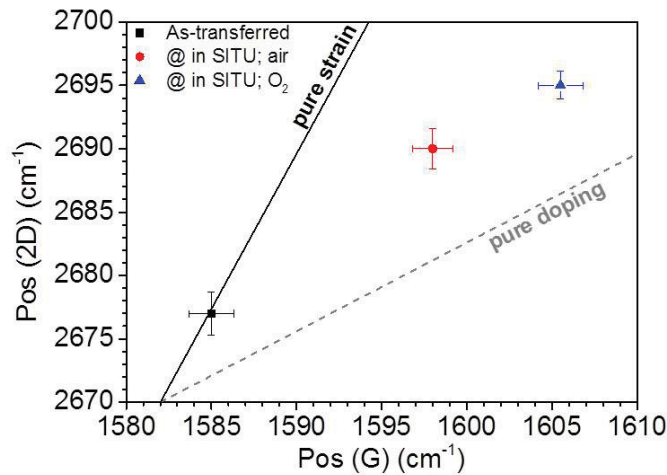


Figure 5.30: Correlation map of the 2D and G peak positions measured at room temperature in the Gr/SiO₂/Si samples as transferred and thermally treated selectively in air and in O₂. The full line marks the stress limit and the dashed line the doping limit as reported in [98]

It has been recently reported that temperature increase induces a red shift both of G and 2D bands as well as line broadening and the appearance of a shoulder to the G band due to thermal strain [251]. These features are compatible to the here reported results.

In particular, the absence of blue shift during in-situ measurements and exposure to oxygen can be interpreted as a competition between temperature induced red shift and doping induced blue shift. This effect gives rise to a balancing and needs to be further investigated to be fully clarified and to disentangle mechanical and doping effects, for example by changing gas during thermal treatments.

5.2.5 Electrical characterization of doping effect induced by oxygen

In order to further evaluate the impact of the O₂ thermal treatments on the doping of the Gr/SiO₂/Si samples, Raman analyses were complemented by electrical measurements on a transmission line model (TLM) test patterns fabricated on an untreated Gr/SiO₂/Si reference sample and on a sample that was subjected to an O₂ treatment in the Linkam cell at 300°C in 2 bar O₂.

A schematic representation of a TLM structure is depicted in Fig. 5.31(a). Gr rectangular stripes were defined by laser writing optical lithography and O₂ plasma etching. Afterwards, metal contacts with identical area and different spacing d were fabricated on the Gr stripes by deposition of a Ni (50 nm)/Au (100 nm) bilayer and lift-off. An optical microscopy of a TLM device is reported in Fig. 5.31(b), where the dashed line indicates the area of the Gr rectangular stripe. Current-voltage (I-V) measurements between different pairs of adjacent metal pads were carried out using a Karl Suss Microtec probe station equipped with a HP 4156B parameter analyzer. As illustrated schematically in Fig. 5.31(a), I-V measurements have been performed between pairs of adjacent pads. All the I-V characteristics exhibit a linear behaviour, indicating that Ohmic contacts are formed between the Ni/Au electrodes and Gr. Hence, the resistance R between each couple of pads is readily obtained as the inverse of the slope of the I-V curves. A plot of R as a function of the pads spacing d is reported in Fig. 5.31(c) for the reference and the O₂ treated samples. Each experimental point in this plot is the average value of the resistances measured between pads with identical spacing in 12 different TLM structures fabricated on the same sample. The error bars were evaluated as the standard deviations of the resistance values for identical contact spacing on the different TLM devices.

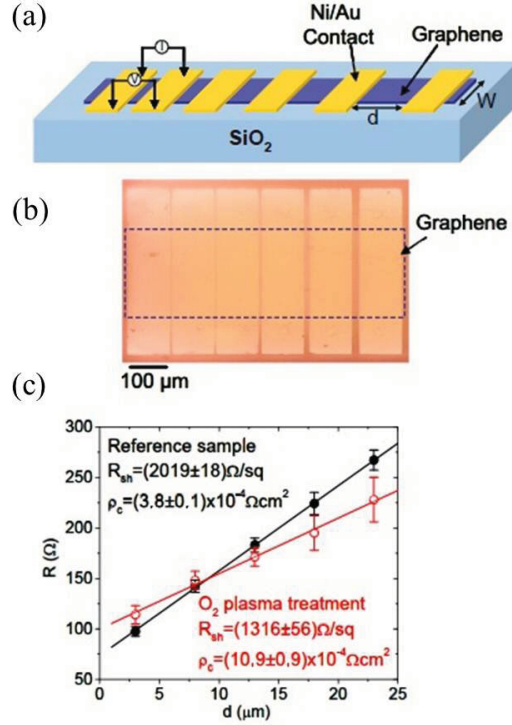


Figure 5.31: Schematic (a) and optical microscopy image (b) of a TLM test structure fabricated on Gr on SiO₂. (c) Plot of the resistance measured between pairs of adjacent contacts on TLM fabricated on a reference (untreated, black filled symbols) sample and a sample treated in O₂ (red open symbols). Each experimental point is the average of the resistances measured between pads with identical spacing in 12 different TLM structures fabricated on the same sample. The error bars are the standard deviations of these resistance values. From the linear fit of the two sets of data, the values of the Gr sheet resistance and of the specific contact resistances have been evaluated. Adapted from [247].

It is evident that for both samples, R grows linearly with d , but with a lower slope in the case of the O₂ treated sample. According to the TLM theory [252], the resistance between two adjacent pads can be expressed as $R = 2R_c + (R_{sh}/W)d$, where R_c is the contact resistance, R_{sh} the Gr sheet resistance and $W = 240$ nm is the width of the Gr stripe. By linear fitting of the two sets of data, the sheet resistance of the Gr reference sample, $R_{sh} = (2019 \pm 18)$

Ω/sq , and of the O₂ treated sample, $R_{sh} = (1316 \pm 56) \Omega / \text{sq}$, were evaluated. This $\sim 35\%$ decrease in the sheet resistance value is fully consistent with the enhanced p-type doping of Gr after the O₂ treatment. The specific contact resistance $\rho_c = R_c W L_T$ of the two samples has been also evaluated, being L_T the transfer length under the contact, obtained from the intercept of the linear fit with the horizontal axis [252]. Almost a factor of 3 increase of ρ_c can be observed going from the reference to the O₂ treated sample. Overall these results show that the O₂ treatment is compatible with doping and with the enhancement of the charge carrier density. Further studies are however needed to better clarify the change in the contact resistance in view of applications.

5.3 Graphene on Al₂O₃/Si

As mentioned in the previous chapter, Gr samples consisting of single crystalline monolayer domains were grown on copper (Cu) by chemical vapor deposition (CVD) and were transferred on a 100 nm thick Al₂O₃ layer on Si by using the PMMA procedure (as schematically shown in figure 1.18). As reported in Fig. 5.32(a) and (b), the presence of Gr on employed Al₂O₃ and SiO₂ substrates and its morphological features have been primarily checked by AFM measurements. As shown in the figures, the samples are characterized by flakes with extension of the order of $\sim 10 \mu\text{m}$ and height varying from flake to flake. The analysis of flakes height is summarized in Fig. 5.32(c). It is found that as-transferred Gr on Al₂O₃ has typical thickness below 2.2 nm, lower than the value 2.8 nm found in the case of Gr transferred on SiO₂, as also shown in Fig. 5.10(c).

These thickness values, higher than expected for single layer of Gr for both samples, can originate in part from the presence of impurities or of some residual PMMA on top of some flakes of Gr, and in part from the substrate roughness, and the presence of a trapped water layer between the substrate and Gr [245, 246].

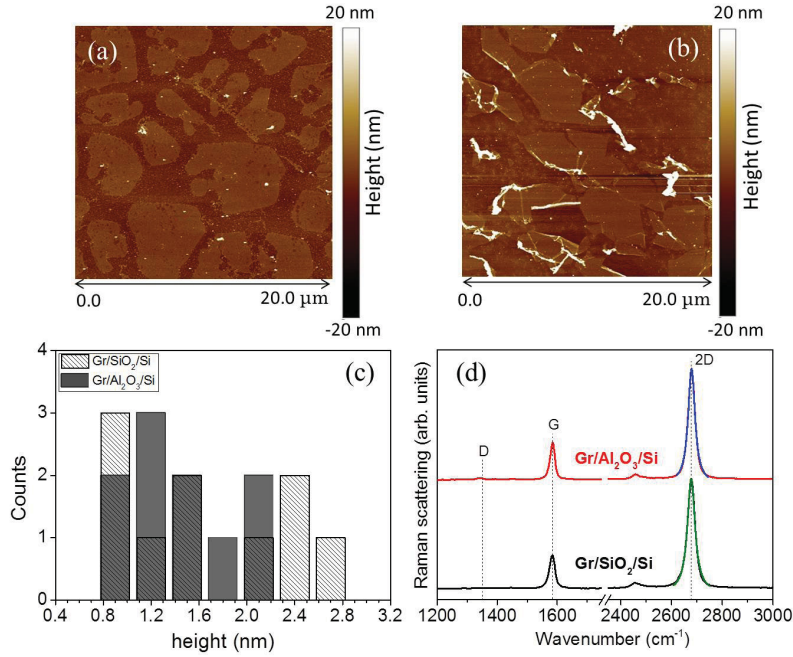


Figure 5.32: As-transferred Gr on SiO₂/Si substrate AFM morphology image (a); as-transferred Gr on Al₂O₃/Si substrate AFM morphology image (b); histograms with height of flakes statistics (c). Comparison of the μ -Raman spectra of the samples of graphene on SiO₂ and graphene on Al₂O₃, focused in the spectral region of the graphene typical bands (d); the 2D band best fit curves with Lorentzian lineshape with full width at half maximum of $(36.5 \pm 0.3) \text{ cm}^{-1}$ for Gr/SiO₂/Si and $(32.0 \pm 0.2) \text{ cm}^{-1}$ for Gr/Al₂O₃/Si are superimposed to the spectra. Adapted from [247].

AFM analyses carried out on bare SiO₂ and Al₂O₃ substrates show similar roughness values in the two cases. On the other hand, by water contact angle measurements, it is evidenced a larger hydrophobicity of Al₂O₃, featuring 80° contact angle, than SiO₂, having 40° contact angle. These experimental results suggest that the different measured Gr thickness values originate from reduced water trapping on Al₂O₃ resulting in a better adhesion between Gr and this type of substrate [249]. The identification of monolayer Gr is specifically carried out by μ -Raman measurements. The results for the sample of Gr/Al₂O₃/Si are reported in Fig. 5.32(d). It can be observed that the typical spectral features of Gr are recorded on the flakes (targeted by contrast

optical image of the microscope of the Raman setup). In details, the G and 2D bands of Gr are identified and are located at $1585 \pm 1 \text{ cm}^{-1}$ and $2680 \pm 1 \text{ cm}^{-1}$, respectively. It is also observed the absence of the D-band, at about 1350 cm^{-1} , indicating the good quality of the Gr. Furthermore, the intensity ratio $I_{2D}/I_G > 2.5$, and the full width at half maximum ($32.0 \pm 0.2 \text{ cm}^{-1}$) and shape (Lorentzian) of the 2D band, quite compatible with literature data $\sim 30 \text{ cm}^{-1}$ [129, 245, 253], evidence the monolayer nature of Gr flakes on $\text{Al}_2\text{O}_3/\text{Si}$. These features are comparable to those found for the other used Gr transferred on SiO_2/Si , as seen previously, and reported in Fig. 5.32(d), and enable to compare the two kinds of samples and conclude that they essentially consist in monolayers of Gr deposited on two different substrates.

5.3.1 Effects of thermal treatment in an Oxygen atmosphere

As we have seen in the previous section, to induce p-type doping of the Gr/ SiO_2/Si sample a thermal treatment of 2h in O_2 at 10 bar and 290°C has been carried out. The main observed effects are the blue shift of the G and 2D bands and the decrease of the I_{2D}/I_G ratio. As previously shown these features indicate a p-type doping and a successive thermal treatment in vacuum at 300°C up to 2h does not affect the changes induced by previous thermal treatment in oxygen, indicating the stability of doping. To clarify the oxygen location as well as to extend the investigation on the efficiency of doping of Gr by this molecule we changed the substrate and seek if the effects of doping observed after the treatment in O_2 are active on a sample of Gr with substrate different from SiO_2 . The sample of Gr/ $\text{Al}_2\text{O}_3/\text{Si}$ has been used. As above reported its flakes of Gr are similar to those observed on SiO_2/Si and, in particular, they are monolayers of few μm size. As shown in Fig. 5.33, a thermal treatment at 10 bar of O_2 for 2h at 290°C is not able to induce any change in the Raman features, evidencing no doping effect in contrast to results reported for Gr on SiO_2 . The treatment of Gr/ $\text{Al}_2\text{O}_3/\text{Si}$ in O_2 has been then repeated for a longer time ($t = 16 \text{ h}$) to clarify any kinetics criticism. Even after this thermal treatment no relevant variations in the Raman spectrum are observed.

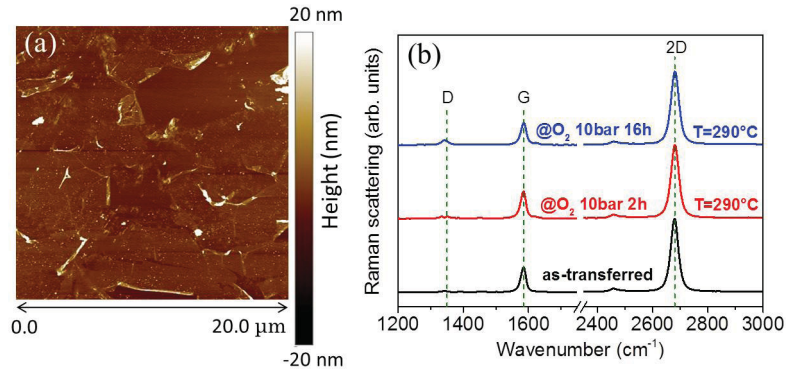


Figure 5.33: Gr on $\text{Al}_2\text{O}_3/\text{Si}$ AFM morphology image after 16h thermal treatment in O_2 at a pressure of 10 bar and 290°C (a). Comparison of the μ -Raman spectra of as transferred Gr/ $\text{Al}_2\text{O}_3/\text{Si}$ and of Gr/ $\text{Al}_2\text{O}_3/\text{Si}$ thermally treated at $T = 290^\circ\text{C}$ with O_2 at a pressure of 10 bar first for 2h (red curve) and then for 16h (blue curve) (b). All the spectra are normalized to the 2D band amplitude and are arbitrarily vertically shifted. Adapted from [247].

As reported in Fig. 5.33(a), the treatments do not affect the flakes properties. Basing on these results, and observing the great analogy of Gr samples transferred on Al_2O_3 and on SiO_2 , it is hypothesized that a prominent role to obtain p-type doping by oxygen treatment is played by the substrate. In particular, if oxygen was bonded on top of graphene it should be equally effective in doping Gr on Al_2O_3 and on SiO_2 but this is not the case as shown by the above reported results. As a consequence, it can be stated that the molecule is trapped in the interface between the flake and the substrate, as schematically shown in Fig. 5.34.

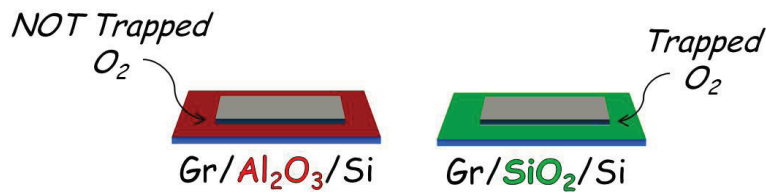


Figure 5.34: Schematic explanation of the positioning of the oxygen during the doping step [247].

The different effectiveness in doping Gr on Al₂O₃ and on SiO₂ suggests that this latter substrate has a larger O₂ adsorption efficiency than the former. This aspect is of particular concern for applications and the possibility to tune this feature, by specifically modifying the SiO₂ surface, for example, could be of relevance. Probably, the most hydrophobic nature of Al₂O₃, as shown by the larger water contact angle of 80°, compared to that of SiO₂, having a contact angle 40°, creates a better interaction and, therefore, a greater proximity between Gr and the substrate inhibiting oxygen allocation. It is worth to note that differences of behaviour of Gr related to the dielectric constant of SiO₂ and Al₂O₃ substrates have been highlighted in literature showing that the two substrates could affect the doping efficiency [249].

5.4 MoS₂ on SiO₂/Si

As mentioned in chapter 4, MoS₂ samples have been obtained by mechanical exfoliation of bulk molybdenite crystals purchased by SPI. The exfoliation technique was based on the use of a thermal release tape with typical release temperature of 130°C and thermo-compression printing [228]. After printing on the SiO₂(300nm)/Si target substrate, the sample surface was carefully cleaned by using solvents in an ultrasonic bath. MoS₂ flakes of different lateral size and variable thickness (from single layer to multilayers) were obtained on SiO₂ by this approach.

Preliminary inspection of MoS₂ flakes was performed by optical microscopy (OM). The variable flakes thickness produces a variable contrast in OM images, due to the light interference effect generated by the MoS₂ thin film with the 300 nm SiO₂ layer thermally grown on Si.

Tapping mode atomic force microscopy (AFM) with a DI3100 AFM was employed for precise determination of flakes thickness. Similarly to previous works with graphene on SiO₂ [242], by systematically comparing optical contrast with thickness measurements by AFM, we have developed a calibration procedure allowing a fast estimation of the flakes thickness and uniformity by OM inspection. Representative OM images on MoS₂ flakes of different sizes and thickness uniformity

are reported in Fig. 5.35 (a) and (b), whereas AFM images of selected areas in these samples are reported in Fig. 5.35 (c) and (d), respectively. Finally, Fig. 5.35 (e) and (f) show the line-scans of MoS₂ film step height with respect to SiO₂ surface and the MoS₂ thickness variations within not uniform samples. The OM images in Fig. 5.35 (a) and (b) have been acquired by the camera integrated with the AFM system using identical illumination conditions with white light. This allows to make a direct comparison between the optical contrast with the film thickness estimated by AFM.

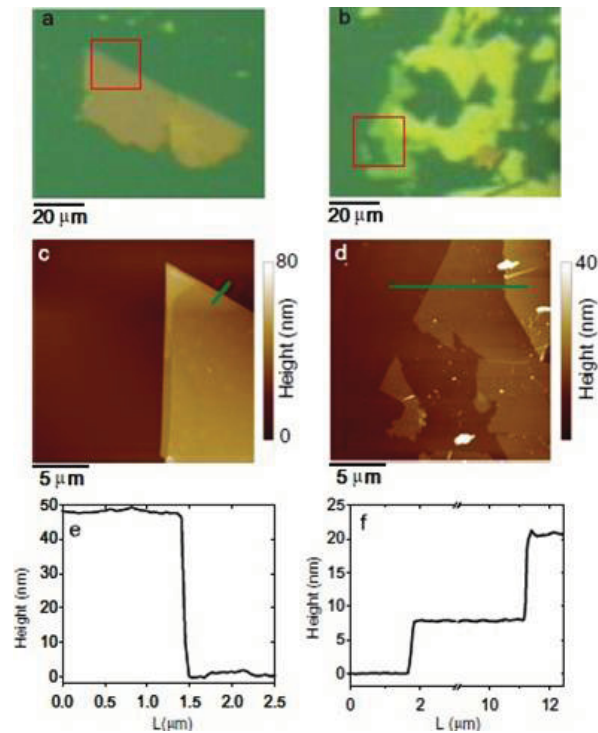


Figure 5.35: (a, b) Representative OM images on MoS₂ flakes of different sizes and thickness uniformity. (c, d) AFM images of selected areas in these samples and (e, f) corresponding height line-scans [254].

5.4.1 Effects of thermal treatment in an Oxygen atmosphere

To investigate the effects of oxygen treatments similar to those inducing doping in graphene, a sample of MoS₂ has been treated in O₂ atmosphere at 2 bar in the temperature range 300°C-430°C in the linkam cell, indeed in this temperature range doping should be effective for few layers [210]. In particular, 10°C increase of temperature steps were applied from 300°C up to 390°C and, at each step, the sample was maintained at the selected temperature for 10 minutes and Raman measurements were collected every minute; afterward the sample temperature was increased to 400°C for 30 minutes, collecting Raman measurements. As reported in Fig. 5.36, the Raman spectrum of the native sample features the typical bands of bulk MoS₂ relative to the E_{2g}¹ and A_{1g} modes at 383 cm⁻¹ and 409 cm⁻¹, respectively, showing that the applied exfoliation process produced multilayer flakes.

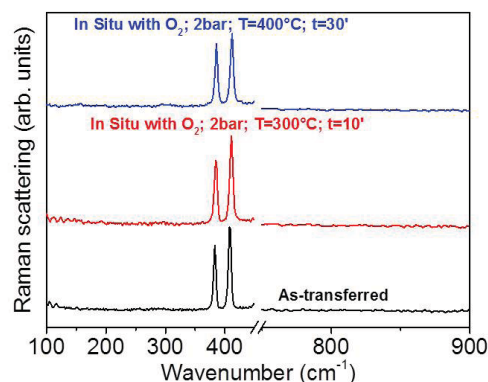


Figure 5.36: In-situ Raman spectra of MoS₂ before thermal treatments (bottom line), after thermal treatment in O₂ at 300°C (middle) and 400°C (top). Spectra are vertically shifted for the sake of comparison.

For all the investigated temperatures, the treatments give no detectable changes in the Raman band features, and in particular we did not observe the appearance of the bands at 158, 285 and 820 cm⁻¹ associated to MoO₃, expected as side product of the oxygen thermally induced doping of MoS₂ [210]. Nevertheless, during these treatments, we observed by the microscope a gradual size reduction of the flakes.

A further increase of temperature up to 430°C had the same effects as lower temperatures. However, as shown in Fig. 5.37, we noticed by the optical microscope measurements a increase of optical contrast between the center of the various MoS_2 flakes and their edges, these latter appearing more dark. To go deeper in this aspect we carried out AFM measurements and, as shown in Fig. 5.37, we found that the edges of the flakes are thinner, suggesting the presence of less layers.

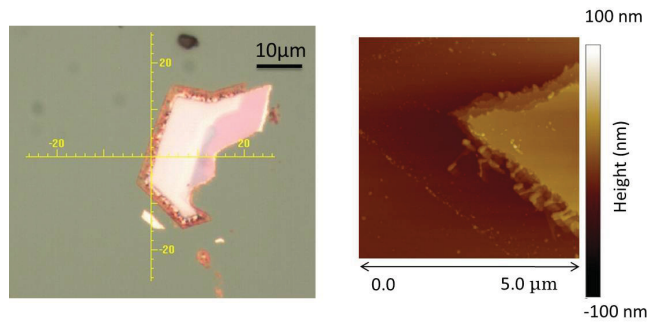


Figure 5.37: MoS_2 flake after the thermal treatment up to 430°C in O_2 optical microscope (left) and AFM (right) images.

As shown in Fig. 5.38, by carrying out Raman measurements ex-situ, we found that the flakes edge zone has a different spectrum.

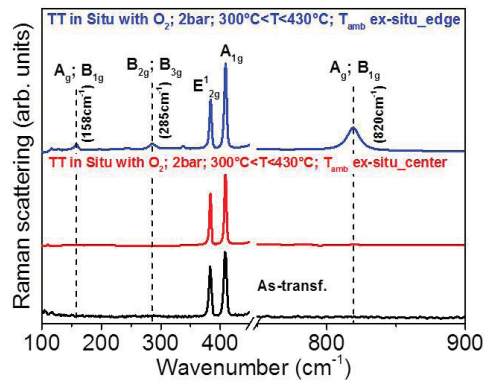


Figure 5.38: Ex-situ Raman spectra of MoS_2 before thermal treatments (bottom line), after thermal treatment in O_2 at $T < 430^{\circ}\text{C}$ in the center of a flake (middle) and on the edge of a flake (top). Spectra are vertically shifted for the sake of comparison.

In particular, the bands attributed to MoO_3 at the spectral positions 158, 285 and 820 cm^{-1} are now clearly seen. This finding suggests that the observed erosion of the flakes during the thermal treatments in oxygen is driven by the formation of oxidized regions in the borders of the MoS_2 flakes that gradually convert them to MoO_3 , before completely destroying it. Similar effects have been suggested for transition metal dichalcogenides and show that the thermal processes could be driven by analogous reactions [255]. In particular, these effects are of relevance for the application of 2D materials in ambient environments where the temperature could be increased during their use. Finally, the possibility that doping of central parts of the flakes occurred during the treatments carried out could not be excluded, but to further highlight it other in-situ measurements with higher spectral resolution, able to detect MoS_2 Raman bands shift or broadening, should be used.

Summary

In this thesis work we have conducted a study on 2D materials, which are of wide interest and relevance in materials science and solid state physics, due to their excellent physical properties. In particular we studied the effects, caused by thermal treatments in air and controlled atmosphere, on graphene and molybdenum disulfide samples.

Gr samples used in these studies were obtained by controlled graphitization of SiC(000 $\bar{1}$) surface during high temperature annealing and by chemical vapour deposition on copper foils and the subsequent transfer to SiO₂/Si or Al₂O₃/Si substrates. MoS₂ thin films have been obtained by exfoliation from the bulk crystal and transfer to SiO₂/Si substrates.

The first phase of the work was focused on the characterization of the different materials by optical microscopy, μ -Raman spectroscopy and atomic force microscopy. Such characterization was found to be relevant to follow the changes of the materials connected to the presence of defects, surface roughness, presence of different numbers of layers of materials, different doping levels and/or different stress effects.

The graphene samples (Gr) were grown on the C face of 4H-SiC under optimized conditions (high annealing temperatures ranging from 1850°C to 1950°C in Ar ambient at 900 mbar) in order to achieve few layers of Gr coverage, with the absence of defects. Several microscopy techniques, including optical microscopy (OM), μ -Raman spectroscopy, atomic force microscopy (AFM) and atomic resolution scanning transmission electron microscopy (STEM) have been used to extensively characterize the lateral uniformity of the as-grown layers at different temperatures. μ -Raman analysis provided information on

the variation of the number of layers, of the stacking-type, doping and strain. For all the growth temperatures from 1850°C to 1950°C, Gr layers were defects-free and their coverage onto SiC was inhomogeneous (the same sample areas with the presence of different thickness graphene), also, the average number of layers was found to increase with the annealing temperature. It's interestingly, that the doping of Gr appears to be uniform basing on the G band analysis; also, in each sample there is the presence of single layer of Gr, Gr with few layers of Bernal stacking type and few layers of Gr with turbostratic stacking type. For all growth temperatures, it has also been observed that layers are compressively strained, with strain increasing with the layer number. Overall these results enabled to find a route to produce high quality graphene on large area showing that the higher temperature gives more uniform spectral features distribution suggesting more uniform properties of graphene.

The graphene samples on SiO₂/Si, consisting of single crystalline monolayer domains, were grown on copper (Cu) by chemical vapor deposition (CVD) and then transferred on a 300 nm thick SiO₂ layer on Si by using the PMMA-assisted transfer procedure. Doping and stability of monolayer are investigated by μ -Raman spectroscopy and atomic force microscopy (AFM) during thermal treatments in oxygen and vacuum controlled atmosphere at temperature lower than 300°C, without destroying the sample. The exposure to molecular oxygen induces graphene changes as evidenced by a blue-shift of the G and 2D Raman bands, together with the decrease of I_{2D}/I_G intensity ratio, which are consistent with a high p-type doping ($\sim 10^{13}$ cm⁻²) of graphene. The successive thermal treatment in vacuum does not affect the induced doping showing this latter stability. By isothermal treatments, made at different temperatures, it is seen that the equilibrium configuration depends on the temperature, indicating a distribution of doping states. Finally, an activation energy of 56 meV of the doping process has been estimated together with a stability or bonding energy larger than 49 meV.

The Raman 2D and G bands spectral positions and amplitude ratio after treatment in O₂ are affected by the permanence in air atmosphere in a time scale of months whereas the vacuum safely maintains the doping effects determined through Raman bands.

We have focused on the possible effects caused by the atmosphere on the p-type doping induced by thermal treatments in O₂ gas of Gr on SiO₂ substrate. It has been shown that thermal treatments in nitrogen (N₂), carbon dioxide (CO₂), or in vacuum controlled atmospheres induce only minor effects on the doping of Gr and principally affect its defectiveness. By contrast, a treatment in H₂O clearly evidences a recovery in the Raman spectral features, towards undoped sample, suggesting that the literature reported air influence on the doping depends on water present in the atmosphere. The disentanglement of strain and doping effects has been also highlighted showing that in presence of oxygen this latter is overwhelming.

While a high p-type doping ($\sim 10^{13}$ cm⁻²) is observed for Gr on SiO₂, no significant doping is found for Gr samples on the Al₂O₃ substrate, suggesting a key role of the Gr/SiO₂ interface states in the trapping of oxygen responsible for the Gr p-type doping. It is deduced that the oxygen, during the doping step, is positioned between the SiO₂ and the layer of graphene, giving the interface Gr/SiO₂ a relevant role for the doping to take place.

The effects of temperature and atmosphere (air and O₂) on the doping of monolayers of graphene (Gr) on SiO₂ substrate on Si have been investigated by in-situ micro-Raman spectroscopy, during thermal treatments up to 350°C. The spectral positions of the G and 2D Raman bands of Gr undergo minor changes during treatment, whereas their amplitude and full width at half maximum (FWHM) experience variations with temperature and with the atmosphere used. The thermal treatments in oxygen atmosphere show, in addition to a thermal effect, an effect attributable to a p-type doping given by this gas. The lineshape thermal broadening, found during thermal treatments by in-situ Raman measurements, can be related to thermal phonon effects whereas the absence of band shift is in agreement to the balancing of red shift, due to thermal effects, and blue shift, induced by doping, showing the potentiality of in-situ measurements to follow the doping kinetics.

Similar in-situ measurements carried out to monitor O₂ doping of MoS₂ on SiO₂/Si substrate have been investigated by in-situ micro-Raman spectroscopy, during thermal treatments up to 430°C, and by Atomic Force Microscopy (AFM). The MoS₂ treatment in O₂ has

evidenced a progressive erosion of the flakes at $T > 300^\circ\text{C}$ without relevant spectral changes in their central zone, during in-situ measurements, whereas the formation of MoO_3 on the flakes edges is observed indicative of the oxygen activated transformation.

In conclusion in this thesis we have focused attention on the possibility of doping and change 2D material properties such as graphene and molybdenum disulfide by means of thermal treatment in a controlled atmosphere showing some potentialities and weaknesses of this procedure. In recent years there has been great interest in order to modify and control the 2D material properties, used in various fields. Regarding the doping it would further be appropriate to understand the role that has the substrate, in that, as seen in the experimental work carried out the doping can depend on the substrate used. For this purpose it would be interesting to perform further experiments varying further the substrate. In this thesis we have seen the effect of SiC, SiO_2/Si and $\text{Al}_2\text{O}_3/\text{Si}$ substrates on graphene samples, noting a invariance of Raman characteristics, as contrasted to a not invariance of the doping of untreated 2D material. As regards the thermal treatment under controlled atmosphere it is necessary to further clarify the role and how is trapped oxygen (in our case, between the graphene and the substrate), or the action of oxygen on different samples (as the oxidation of MoS_2). It would be also interesting to study the variation of the thermal and thermal doping effects on other types of 2D materials, or build and observe the changes obtained on heterostructures consisting of suitably doped 2D materials in order to obtain devices with appropriate physical properties.

Bibliography

- [1] J. I. Gersten and F. W. Smith. *The Physics and Chemistry of Materials*. John Wiley & Sons, 2001.
- [2] M. Chhowalla, H. S. Shin, G. Eda, L.-J. Li, K. P. Loh, and H. Zhang. The chemistry of two-dimensional layered transition metal dichalcogenide nanosheets. *Nature Chemistry*, 5:263–275, 2013.
- [3] M. Xu, T. Liang, M. Shi, and H. Chen. Graphene-Like Two-Dimensional Materials. *Chem. Rev.*, 113:3766–3798, 2013.
- [4] A. K. Geim and K. S. Novoselov. The rise of graphene. *Nature Materials*, 6:183–191, 2007.
- [5] K. S. Novoselov, D. Jiang, F. Schedin, T. J. Booth, V. V. Khotkevich, S. V. Morozov, and A. K. Geim. Two-dimensional atomic crystals. *Proc. Natl. Acad. Sci.*, 102:10451–10453, 2005.
- [6] K. S. Novoselov, A. K. Geim, S. V. Morozov, D. Jiang, Y. Zhang, S. V. Dubonos, I. V. Grigorieva, and A. A. Firsov. Electric Field Effect in Atomically Thin Carbon Films. *Science*, 306:666–669, 2004.
- [7] A. K. Geim and I. V. Grigorieva. Van der Waals heterostructures. *Nature*, 499:419–425, 2013.
- [8] X. Li, W. Cai, J. An, S. Kim, J. Nah, D. Yang, R. Piner, A. Velamakanni, I. Jung, E. Tutuc, S. K. Banerjee, L. Colombo, and R. S. Ruoff. Large-Area Synthesis of High-Quality and Uniform Graphene Films on Copper Foils. *Science*, 324:1312–1314, 2009.

- [9] T. Ohta, A. Bostwick, T. Seyller, K. Horn, and E. Rotenberg. Controlling the Electronic Structure of Bilayer Graphene. *Science*, 313:951–954, 2006.
- [10] W. A. de Heer, C. Berger, X. Wu, P. N. First, E. H. Conrad, X. Li, T. Li, M. Sprinkle, J. Hass, M. L. Sadowski, M. Potemski, and G. Martinez. Epitaxial graphene. *Solid State Communications*, 143:92–100, 2007.
- [11] Y. H. Lee, X. Q. Zhang, W. Zhang, M. T. Chang, C. T. Lin, K. D. Chang, Y. C. Yu, J. T. W. Wang, C. S. Chang, L. J. Li, and T. W. Lin. Synthesis of Large–Area MoS₂ Atomic Layers with Chemical Vapor Deposition. *Adv. Mater.*, 24:2320–2325, 2012.
- [12] Y. Zhan, Z. Liu, S. Najmaei, P. M. Ajayan, and J. Lou. Large–Area Vapor–Phase Growth and Characterization of MoS₂ Atomic Layers on a SiO₂ Substrate. *Small*, 8:966–971, 2012.
- [13] J. Kim, C. Bayram, H. Park, C.-W. Cheng, C. Dimitrakopoulos, J. A. Ott, K. B. Reuter, S. W. Bedell, and D. K. Sadana. Principle of direct van der Waals epitaxy of single–crystalline films on epitaxial graphene. *Nature Commun.*, 5:1–7, 2014.
- [14] H. W. Kroto, J. R. Heath, S. C. O’Brien, R. F. Curl, and R. E. Smalley. C₆₀ : Buckminsterfullerene. *Nature*, 318:162–163, 1985.
- [15] B. Bharat. *Scanning Probe Microscopy in Nanoscience and Nanotechnology*. Springer, 2010.
- [16] P. R. Wallace. The Band Theory of Graphite. *Phys. Rev.*, 31:622–634, 1947.
- [17] E. McCann and M. Koshino. The electronic properties of bilayer graphene. *Rep. Prog. Phys.*, 76:056503(1–28), 2013.
- [18] S. Reich, J. Maultzsch, , C. Thomsen, and P. Ordejón. Tight–binding description of graphene. *Phys. Rev. B*, 66:035412(1–5), 2002.
- [19] F. Giannazzo and V. Raineri. Graphene: synthesis and nanoscale characterization of electronic properties. *Rivista del Nuovo Cimento*, 35:267–304, 2012.

- [20] A. H. Castro Neto, F. Guinea, N. M. R. Peres, K. S. Novoselov, and A. K. Geim. The electronic properties of graphene. *Rev. Mod. Phys.*, 81:109–162, 2009.
- [21] C. Bena and S. A. Kivelson. Quasiparticle scattering and local density of states in graphite. *Phys. Rev. B*, 72:125432(1–5), 2005.
- [22] K. S. Novoselov, A. K. Geim, S. V. Morozov, D. Jiang, M. I. Katsnelson, I. V. Grigorieva, S. V. Dubonos, and A. A. Firsov. Two-dimensional gas of massless Dirac fermions in graphene. *Nature*, 438:197–200, 2005.
- [23] K.I. Bolotin, K.J. Sikes, Z. Jiang, M. Klima, G. Fudenberg, J. Hone, P. Kim, and H.L. Stormer. Ultrahigh electron mobility in suspended graphene. *Solid State Communications*, 146:351–355, 2008.
- [24] T. Stauber, N. M. R. Peres, and F. Guinea. Electronic transport in graphene: A semiclassical approach including midgap states. *Phys. Rev. B*, 76:205423(1–10), 2007.
- [25] E. H. Hwang, S. Adam, and S. Das Sarma. Carrier Transport in Two-Dimensional Graphene Layers. *Phys. Rev. Lett.*, 98:186826(1–4), 2007.
- [26] J.H. Chen, C. Jang, S. Xiao, M. Ishigami, and M. S. Fuhrer. Intrinsic and Extrinsic Performance Limits of Graphene Devices on SiO₂. *Nature Nanotechnology*, 3:206–209, 2008.
- [27] T. Ando. Screening Effect and Impurity Scattering in Monolayer Graphene. *J. Phys. Soc. Jpn*, 75:074716(1–7), 2006.
- [28] S. Bae, H. Kim, Y. Lee, X. Xu, J. Park, Y. Zheng, J. Balakrishnan, T. Lei, H. R. Kim, Y. I. Song, Y. J. Kim, K. S. Kim, B. Özyilmaz, J. H. Ahn, B. H. Hong, and S. Iijima. Roll-to-roll production of 30-inch graphene films for transparent electrodes. *Nature Nanotechnology*, 5:574–578, 2010.
- [29] F. Bonaccorso, Z. Sun, T. Hasan, and A. C. Ferrari. Graphene photonics and optoelectronics. *Nature Photonics*, 4:611–622, 2010.

- [30] R. R. Nair, P. Blake, A. N. Grigorenko, K. S. Novoselov, T. J. Booth, T. Stauber, N. M. R. Peres, and A. K. Geim. Fine Structure Constant Defines Visual transparency of graphene. *Science*, 320:1308, 2008.
- [31] A. B. Kuzmenko, E. van Heumen, F. Carbone, and D. van der Marel. Universal Optical Conductance of Graphite. *Phys. Rev. Lett.*, 100:117401(1–4), 2008.
- [32] A. A. Balandin, S. Ghosh, W. Bao, Irene Calizo, D. Teweldebrhan, F. Miao, and C. N. Lau. Superior Thermal Conductivity of Single-Layer Graphene. *Nano Lett.*, 8:902–907, 2008.
- [33] A. A. Balandin. Thermal properties of graphene and nanostructured carbon materials. *Nature Materials*, 10:569–581, 2011.
- [34] S. Chen, Q. Wu, C. Mishra, J. Kang, H. Zhang, K. Cho, W. Cai, A. A. Balandin, and R. S. Ruoff. Thermal conductivity of isotopically modified graphene. *Nature Materials*, 11:203–207, 2012.
- [35] T. Tohei, A. Kuwabara, F. Oba, and I. Tanaka. Debye temperature and stiffness of carbon and boron nitride polymorphs from first principles calculations. *Phys. Rev. B*, 73:064304(1–7), 2006.
- [36] G. D. Sanders, A. R. T. Nugraha, K. Sato, J. H. Kim, J. Kono, R. Saito, and C. J. Stanton. Theory of coherent phonons in carbon nanotubes and graphene nanoribbons. *J. Phys.:Condens. Matter*, 25:144201(1–32), 2013.
- [37] E. Pop, V. Varshney, and A. K. Roy. Thermal properties of graphene: Fundamentals and applications. *MRS Bull.*, 37:1273–1281, 2012.
- [38] B. Qiu and X. Ruan. Reduction of spectral phonon relaxation times from suspended to supported graphene. *Appl.Phys.Lett.*, 100:193101(1–4), 2012.
- [39] C. Lee, X. Wei, J. W. Kysar, and J. Hone. Measurement of the Elastic Properties and Intrinsic Strength of monolayer graphene. *Science*, 321:385–388, 2008.

- [40] B. I. Yakobson, C. J. Brabec, and J. Bernholc. Nanomechanics of Carbon Tubes: Instabilities beyond Linear Response. *Phys. Rev. Lett.*, 76:2511–2514, 1996.
- [41] D. C. Elias, R. R. Nair, T. M. G. Mohiuddin, S. V. Morozov, P. Blake, M. P. Halsall, A. C. Ferrari, D. W. Boukhvalov, M. I. Katsnelson, A. K. Geim, and K. S. Novoselov. Control of Graphene’s Properties by Reversible Hydrogenation: Evidence for Graphane. *Science*, 323:610–613, 2009.
- [42] A. Savchenko. Transforming Graphene. *Science*, 323:589–590, 2009.
- [43] M. Inagaki and F. Kang. Graphene Derivatives: Graphane, fluorographene, graphene oxide, graphyne and graphdiyne. *J. Mater. Chem. A*, 2:13193–13206, 2014.
- [44] S.-S. Li, K.-H. Tu, C.-C. Lin, C.-W. Chen, and M. Chhowalla. Solution-Processable Graphene Oxide as an Efficient Hole Transport Layer in Polymer Solar Cells. *ACS Nano*, 4:3169–3174, 2010.
- [45] F. Molitor, A. Jacobsen, C. Stampfer, J. Güttinger, T. Ihn, and K. Ensslin. Transport gap in side-gated graphene constrictions. *Phys. Rev. B*, 79:075426(1–5), 2009.
- [46] J.-P. Shim, M. Choe, S.-R. Jeon, D. Seo, T. Lee, and D.-S Lee. InGaN-Based p-i-n Solar Cells with Graphene Electrodes. *Appl. Phys. Express*, 4:052302(1–3), 2011.
- [47] Z. Yin, S. Wu, X. Zhou, X. Huang, Q. Zhang, F. Boey, and H. Zhang. Electrochemical Deposition of ZnO Nanorods on Transparent Reduced Graphene Oxide Electrodes for Hybrid Solar Cells. *Small*, 6:307–312, 2010.
- [48] X. Wang, L. Zhi, and K. Müllen. Transparent, Conductive Graphene Electrodes for Dye-Sensitized Solar Cells. *Nano Lett.*, 8:323–327, 2008.
- [49] S. Casaluci, M. Gemmi, V. Pellegrini, A. Di Carlo, and F. Bonaccorso. Graphene-based large area dye-sensitized solar cell modules. *Nanoscale*, 8:5368–5378, 2016.

- [50] L. A. Ponomarenko, F. Schedin, M. I. Katsnelson, R. Yang, E. W. Hill, K. S. Novoselov, and A. K. Geim. Chaotic Dirac Billiard in Graphene Quantum Dots. *Science*, 320:356–358, 2008.
- [51] Y.-M. Lin, C. Dimitrakopoulos, K. A. Jenkins, D. B. Farmer, H.-Y. Chiu, A. Grill, and Ph. Avouris. 100-GHz Transistors from Wafer-Scale Epitaxial Graphene. *Science*, 327:662, 2010.
- [52] J. R. Williams, L. DiCarlo, and C. M. Marcus. Quantum Hall Effect in a Gate-Controlled p-n Junction of Graphene. *Science*, 317:638–641, 2007.
- [53] J. Cai, P. Ruffieux, R. Jaafar, M. Bieri, T. Braun, S. Blankenburg, M. Muoth, A. P. Seitsonen, M. Saleh, X. Feng, K. Müllen, and R. Fasel. Atomically precise bottom-up fabrication of graphene nanoribbons. *Nature*, 466:470–473, 2010.
- [54] K. Kim, J.-Y. Choi, T. Kim, S.-H. Cho, and H.-J. Chung. A role for graphene in silicon-based semiconductor devices. *Nature*, 479:338–344, 2011.
- [55] F. Schwierz. Graphene transistors. *Nature Nanotechnology*, 5:487–496, 2010.
- [56] C. A. Merchant, K. Healy, M. Wanunu, V. Ray, N. Peterman, J. Bartel, M. D. Fischbein, K. Venta, Z. Luo, A. T. C. Johnson, and M. Drndić. DNA Translocation through Graphene Nanopores. *Nano Lett.*, 10:2915–2921, 2010.
- [57] S. Garaaj, W. Hubbard, A. Reina, J. Kong, D. Branton, and J. A. Golovchenko. Graphene as a subnanometre trans-electrode membrane. *Nature*, 467:190–193, 2010.
- [58] F. Yavari, Z. Chen, A. V. Thomas, W. Ren, H.-M. Cheng, and N. Koratkar. High Sensitivity Gas Detection Using a Macroscopic Three-Dimensional Graphene Foam Network. *Sci. Rep.*, 1:1–5, 2011.
- [59] Y. Lu, B. R. Goldsmith, N. J. Kybert, and A. T. C. Johnson. DNA-decorated graphene chemical sensors. *Appl. Phys. Lett.*, 97:083107(1–3), 2010.

- [60] Y. Ohno, K. Maehashi, and K. Matsumoto. Label-Free Biosensors Based on Aptamer-Modified Graphene Field-Effect Transistors. *J. AM. CHEM. SOC.*, 132:18012–18013, 2010.
- [61] V. C. Sanchez, A. Jachak, R. H. Hurt, and A. B. Kane. Biological Interactions of Graphene-Family Nanomaterials: An Interdisciplinary Review. *Chem. Res. Toxicol.*, 25:15–34, 2012.
- [62] Y. Wang, Z. Li, J. Wang, J. Li, and Y. Lin. Graphene and graphene oxide: biofunctionalization and applications in biotechnology. *Trends in Biotechnology*, 29:205–212, 2011.
- [63] M. D. Stoller, S. Park, Y. Zhu, J. An, and R. S. Ruoff. Graphene-Based Ultracapacitors. *Nano Lett.*, 8:3498–3502, 2008.
- [64] E. Yoo, T. Okata, T. Akita, M. Kohyama, J. Nakamura, and I. Honma. Enhanced Electrocatalytic Activity of Pt Subnanoclusters on Graphene Nanosheet Surface. *Nano Lett.*, 9:2255–2259, 2009.
- [65] K. S. Novoselov, V. I. Fal’ko, L. Colombo, P. R. Gellert, M. G. Schwab, and K. Kim. A roadmap for graphene. *Nature*, 490:192–200, 2012.
- [66] E. Yoo, J. Kim, E. Hosono, H. Zhou, T. Kudo, and I. Honma. Large Reversible Li Storage of Graphene Nanosheet Families for Use in Rechargeable Lithium Ion Batteries. *Nano Lett.*, 8:2277–2282, 2008.
- [67] M. Cai, D. Thorpe, D. H. Adamsonb, and H. C. Schniepp. Methods of graphite exfoliation. *J. Mater. Chem.*, 22:24992–25002, 2012.
- [68] C. Gómez-Navarro, M. Burghard, and K. Kern. Elastic Properties of Chemically Derived Single Graphene Sheets. *Nano Lett.*, 8:2045–2049, 2008.
- [69] D.R. Dreyer, S. Park, C.W. Bielawski, and R.S. Ruoff. The chemistry of graphene oxide. *Chem. Soc. Rev.*, 39:228–240, 2010.

- [70] H. C. Schniepp, J. L. Li, M. J. McAllister, H. Sai, M. Herrera-Alonso, D. H. Adamson, R. K. Prudhomme, R. Car, D. A. Saville, and I. A. Aksay. Functionalized Single Graphene Sheets Derived from Splitting Graphite Oxide. *J. Phys. Chem. B*, 110:8535–8539, 2006.
- [71] W. J. Choyke, H. Matsunami, and G. Pensl. *Silicon Carbide: Recent Major Advances*. Springer-Verlag, 2004.
- [72] C. Berger, Z. Song, T. Li, X. Li, A. Y. Ogbazghi, R. Feng, Z. Dai, A. N. Marchenkov, E. H. Conrad, P. N. First, and W. A. de Heer. Ultrathin Epitaxial Graphite: 2D Electron Gas Properties and a Route toward Graphene-based Nanoelectronics. *J. Phys. Chem. B*, 108:19912–19916, 2004.
- [73] C. Riedl, U. Starke, J. Bernhardt, M. Franke, and K. Heinz. Structural properties of the graphene–SiC(0001) interface as a key for the preparation of homogeneous large-terrace graphene surfaces. *Phys. Rev. B*, 76:245406(1–8), 2007.
- [74] C. Berger, Z. Song, X. Li, X. Wu, N. Brown, C. Naud, D. Mayou, T. Li, J. Hass, A. N. Marchenkov, E. H. Conrad, P. N. First, and W. A. de Heer. Electronic Confinement and Coherence in Patterned Epitaxial Graphene. *Science*, 312:1191–1196, 2006.
- [75] C. Virojanadara, M. Syväjarvi, R. Yakimova, L. I. Johansson, A. A. Zakharov, and T. Balasubramanian. Homogeneous large-area graphene layer growth on 6H–SiC(0001). *Phys. Rev. B*, 78:245403(1–6), 2008.
- [76] I. Forbeaux, J. M. Themlin, and J. M. Debever. Heteroepitaxial graphite on 6H–SiC (0001): Interface formation through conduction-band electronic structure. *Phys. Rev. B*, 58:16396–16406, 1998.
- [77] J. Hass, F. Varchon, J. E. Millán-Otoya, M. Sprinkle, N. Sharma, W. A. de Heer, C. Berger, P. N. First, L. Magaud, , and E. H. Conrad. Why Multilayer Graphene on 4H–SiC (000 $\bar{1}$) Behaves Like a Single Sheet of Graphene. *Phys. Rev. Lett.*, 100:125504(1–4), 2008.

- [78] F. Varchon, R. Feng, J. Hass, X. Li, B. Ngoc Nguyen, C. Naud, P. Mallet, J.-Y. Veullen, C. Berger, E. H. Conrad, and L. Magaud. Electronic Structure of Epitaxial Graphene Layers on SiC: Effect of the Substrate. *Phys. Rev. Lett.*, 99:126805(1–4), 2007.
- [79] K. V. Emtsev, F. Speck, Th. Seyller, L. Ley, and J. D. Riley. Interaction, growth, and ordering of epitaxial graphene on SiC0001 surfaces: A comparative photoelectron spectroscopy study. *Phys. Rev. B*, 77:155303(1–10), 2008.
- [80] G. Nicotra, I. Deretzis, M. Scuderi, C. Spinella, P. Longo, R. Yakimova, F. Giannazzo, and A. La Magna. Interface disorder probed at the atomic scale for graphene grown on the C face of SiC. *Phys. Rev. B*, 91:155411(1–6), 2015.
- [81] C. Riedl, C. Coletti, T. Iwasaki, A. A. Zakharov, and U. Starke. Quasi-Free-Standing Epitaxial Graphene on SiC Obtained by Hydrogen Intercalation. *Phys. Rev. Lett.*, 103:246804(1–4), 2009.
- [82] C. Mattevi, H. Kima, and M. Chhowalla. A review of chemical vapour deposition of graphene on copper. *J. Mater. Chem.*, 21:3324–3334, 2011.
- [83] A. W. Tsen, L. Brown, M. P. Levendorf, F. Ghahari, P. Y. Huang, R. W. Havener, C. S. Ruiz-Vargas, D. A. Muller, P. Kim, and J. Park;. Tailoring Electrical Transport Across Grain Boundaries in Polycrystalline Graphene. *Science*, 336:1143–1146, 2012.
- [84] Y. Wei, J. Wu, H. Yin, X. Shi, R. Yang, and M. Dresselhaus. The nature of strength enhancement and weakening by pentagon-heptagon defects in graphene. *Nature Materials*, 11:759–763, 2012.
- [85] K. S. Kim, Y. Zhao, H. Jang, J. M. Kim S. Y. Lee and, K. S. Kim, J. H. Ahn, P. Kim, J. Y. Choi, and B. H. Hong. Large-scale pattern growth of graphene films for stretchable transparent electrodes. *Nature*, 457:706–710, 2009.
- [86] X. Li, Y. Zhu, W. Cai, M. Borysiak, B. Han, D. Chen, R. D. Piner, L. Colombo, and R. S. Ruoff. Transfer of Large-Area

- Graphene Films for High-Performance Transparent Conductive Electrodes. *Nano Lett.*, 9:4359–4363, 2009.
- [87] A. Reina, X. Jia, J. Ho, D. Nezich, H. Son, V. Bulovic, M. S. Dresselhaus, and J. Kong. Large Area, Few-Layer Graphene Films on Arbitrary Substrates by Chemical Vapor Deposition. *Nano Lett.*, 9:30–35, 2009.
- [88] J. W. Suk, A. Kitt, C. W. Magnuson, Y. Hao, S. Ahmed, J. An, A. K. Swan, B. B. Goldberg, and R. S. Ruoff. Transfer of CVD-Grown Monolayer Graphene onto Arbitrary Substrates. *ACS Nano*, 5:6916–6924, 2011.
- [89] Z. Cheng, Q. Zhou, C. Wang, Q. Li, C. Wang, and Y. Fang. Toward Intrinsic Graphene Surfaces: A Systematic Study on Thermal Annealing and Wet-Chemical Treatment of SiO₂-Supported Graphene Devices. *Nano Lett.*, 11:767–771, 2011.
- [90] J. Kedzierski, P. L. Hsu, A. Reina, J. Kong, P. Healey, P. Wyatt, and C. Keast. Graphene-on-Insulator Transistors Made Using C on Ni Chemical-Vapor Deposition. *IEEE ELECTRON DEVICE LETTERS*, 30:745–747, 2009.
- [91] T. O. Wehling, K. S. Novoselov, S. V. Morozov, E. E. Vdovin, M. I. Katsnelson, A. K. Geim, and A. I. Lichtenstein. Molecular Doping of Graphene. *Nano Lett.*, 8:173–177, 2008.
- [92] C. Casiraghi, S. Pisana, K. S. Novoselov, A. K. Geim, and A. C. Ferrari. Raman fingerprint of charged impurities in graphene. *Appl. Phys. Lett.*, 91:233108(1–3), 2007.
- [93] S. Masubuchi, M. Arai, and T. Machida. Atomic Force Microscopy Based Tunable Local Anodic Oxidation of Graphene. *Nano Lett.*, 11:4542–4546, 2011.
- [94] S. Zhao, S. P. Surwade, Z. Li, and H. Liu. Photochemical oxidation of CVD-grown single layer graphene. *Nanotechnology*, 23:355703(1–6), 2012.
- [95] L. Liu, S. Ryu, M. R. Tomasik, E. Stolyarova, N. Jung, M. S. Hybertsen, M. L. Steigerwald, L. E. Brus, and G. W. Flynn.

- Graphene Oxidation: Thickness-Dependent Etching and Strong Chemical Doping. *Nano Lett.*, 8:1965–1970, 2008.
- [96] S. Ryu, L. Liu, S. Berciaud, Y. J. Yu, H. Liu, P. Kim, G. W. Flynn, and L. E. Brus. Atmospheric Oxygen Binding and Hole Doping in Deformed Graphene on a SiO₂ Substrate. *Nano Lett.*, 10:4944–4951, 2010.
- [97] A. Felten, A. Eckmann, J. J. Pireaux, R. Krupke, and C. Casiraghi. Controlled modification of mono- and bilayer graphene in O₂, H₂ and CF₄ plasmas. *Nanotechnology*, 24:355705(1–8), 2013.
- [98] T. G. A. Verhagen, K. Drogowska, M. Kalbac, and J. Vejpravova. Temperature-induced strain and doping in monolayer and bilayer isotopically labeled graphene. *Phys. Rev. B*, 92:125437(1–9), 2015.
- [99] H. Liu, Y. Liu, and D. Zhu. Chemical doping of graphene. *J. Mater. Chem.*, 21:3335–3345, 2011.
- [100] F. Schedin, A. K. Geim, S. V. Morozov, E. W. Hill, P. Blake, M. I. Katsnelson, and K. S. Novoselov. Detection of individual gas molecules adsorbed on graphene. *Nature Materials*, 6:652–655, 2007.
- [101] M. Lafkioti, B. Krauss, T. Lohmann, U. Zschieschang, H. Klauk, K. v. Klitzing, and J. H. Smet. Graphene on a Hydrophobic Substrate: Doping Reduction and Hysteresis Suppression under Ambient Conditions. *Nano Lett.*, 10:1149–1153, 2010.
- [102] Q. Yu, J. Lian, S. Siriponglert, H. Li, Y. P. Chen, and S.-S. Pei. Graphene segregated on Ni surfaces and transferred to insulators. *Appl. Phys. Lett.*, 93:113103(1–3), 2008.
- [103] M.P. Levendorf, C.S. Ruiz-Vargas, S. Garg, and J. Park. Transfer-free batch fabrication of single layer graphene transistors. *Nano Lett.*, 9:4479–4483, 2009.
- [104] J.-M. Aubry, C. Pierlot, J. Rigaudy, and R. Schmidt. Reversible Binding of Oxygen to Aromatic Compounds. *Acc. Chem. Res.*, 36:668–675, 2003.

- [105] P. G. Collins, K. Bradley, M. Ishigami, and A. Zettl. Extreme oxygen sensitivity of electronic properties of carbon nanotubes. *Science*, 287:1801–1804, 2000.
- [106] Z. H. Ni, H. M. Wang, Z. Q. Luo, Y. Y. Wang, T. Yu, Y. H. Wu, and Z. X. Shen. The effect of vacuum annealing on graphene. *J. Raman Spectrosc.*, 41:479–483, 2010.
- [107] D. Wei, Y. Liu, Y. Wang, H. Zhang, L. Huang, and G. Yu. Synthesis of N-doped graphene by chemical vapor deposition and its electrical properties. *Nano Lett.*, 9:1752–1758, 2009.
- [108] L. S. Panchakarla, K. S. Subrahmanyam, S. K. Saha, Achutharao Govindaraj, H. R. Krishnamurthy, U. V. Waghmare, and C. N. R. Rao. Synthesis, Structure, and Properties of Boron- and Nitrogen-Doped Graphene. *Adv. Mater.*, 21:4726–4730, 2009.
- [109] B. Guo, Q. Liu, E. Chen, H. Zhu, L. Fang, and J. R. Gong. Controllable N-Doping of Graphene. *Nano Lett.*, 10:4975–4980, 2010.
- [110] K. K. Kim, A. Reina, Y. Shi, H. Park, L. J. Li, Y. H. Lee, and J. Kong. Enhancing the conductivity of transparent graphene films via doping. *Nanotechnology*, 21:285205(1–6), 2010.
- [111] Y. Yang and R. Murali. Binding mechanisms of molecular oxygen and moisture to graphene. *Appl. Phys. Lett.*, 98:093116(1–3), 2011.
- [112] Z. Jin, J. Yao, C. Kittrell, and J. M. Tour. Large-Scale Growth and Characterizations of Nitrogen-Doped Monolayer Graphene Sheets. *ACS Nano*, 5:4112–4117, 2011.
- [113] C. Zhang, L. Fu, N. Liu, M. Liu, Y. Wang, and Z. Liu. Synthesis of nitrogen-doped graphene using embedded carbon and nitrogen sources. *Adv. Mater.*, 23:1020–1024, 2011.
- [114] X. Dong, D. Fu, W. Fang, Y. Shi, P. Chen, and L. J. Li. Doping single-layer graphene with aromatic molecules. *Small*, 5:1422–1426, 2009.

- [115] B. Das, R. Voggu, C. S. Rout, and C. N. R. Rao. Changes in the electronic structure and properties of graphene induced by molecular charge–transfer. *Chem. Commun.*, pages 5155–5157, 2008.
- [116] A. C. Ferrari and D. M. Basko. Raman spectroscopy as a versatile tool for studying the properties of graphene. *Nature Nanotechnology*, 8:235–246, 2013.
- [117] R. Saito, A. Jorio, A. G. Souza Filho, G. Dresselhaus, M. S. Dresselhaus, and M. A. Pimenta. Probing Phonon Dispersion Relations of Graphite by Double Resonance Raman Scattering. *Phys. Rev. Lett.*, 88:027401(1–4), 2002.
- [118] D. L. Mafra, G. Samsonidze, L. M. Malard, D. C. Elias, J. C. Brant, F. Plentz, E. S. Alves, and M. A. Pimenta. Determination of LA and TO phonon dispersion relations of graphene near the Dirac point by double resonance Raman scattering. *Phys. Rev. B*, 76:233407(1–4), 2007.
- [119] S. Piscanec, M. Lazzeri, F. Mauri, and A.C. Ferrari. Optical phonons of graphene and nanotubes. *Eur. Phys. J. Special Topics*, 148:159–170, 2007.
- [120] J. Maultzsch, S. Reich, C. Thomsen, H. Requardt, and P. Ordejón. Phonon Dispersion in Graphite. *Phys. Rev. Lett.*, 92:075501(1–4), 2004.
- [121] L. M. Malard, M. A. Pimenta, G. Dresselhaus, and M. S. Dresselhaus. Raman spectroscopy in graphene. *Physics Reports*, 473:51–87, 2009.
- [122] G. G. Samsonidze, E. B. Barros, R. Saito, J. Jiang, G. Dresselhaus, and M. S. Dresselhaus. Electron–phonon coupling mechanism in two–dimensional graphite and single–wall carbon nanotubes. *Phys. Rev. B*, 75:155420(1–8), 2007.
- [123] M.S. Dresselhaus, A. Jorio, and R. Saito. Characterizing Graphene, Graphite, and Carbon Nanotubes by Raman Spectroscopy. *Annu. Rev. Condens. Matter Phys.*, 12:89–108, 2010.

- [124] W. Kohn. Image of the Fermi Surface in the Vibration Spectrum of a Metal. *Phys. Rev. Lett.*, 2:393–394, 1959.
- [125] S. Piscanec, M. Lazzeri, Francesco Mauri, A. C. Ferrari, and J. Robertson. Kohn Anomalies and Electron–Phonon Interactions in Graphite. *Phys. Rev. Lett.*, 93:185503(1–4), 2004.
- [126] F. Tuinstra and J. L. Koenig. Raman Spectrum of Graphite. *J. Chem. Phys.*, 53:1126–1130, 1970.
- [127] A. C. Ferrari and J. Robertson. Interpretation of Raman spectra of disordered and amorphous carbon. *Phys. Rev. B*, 61:14095–14107, 2000.
- [128] A. C. Ferrari. Raman spectroscopy of graphene and graphite: Disorder, electron-phonon coupling, doping and nonadiabatic effects. *Solid State Communications*, 143:47–57, 2007.
- [129] A. C. Ferrari, J. C. Meyer, V. Scardaci, C. Casiraghi, M. Lazzeri, F. Mauri, S. Piscanec, D. Jiang, K. S. Novoselov, S. Roth, and A. K. Geim. Raman Spectrum of Graphene and Graphene Layers. *Phys. Rev. Lett.*, 97:187401(1–4), 2006.
- [130] L. M. Malard, J. Nilsson, D. C. Elias, J. C. Brant, F. Plentz, E. S. Alves, A. H. Castro Neto, and M. A. Pimenta. Probing the electronic structure of bilayer graphene by Raman scattering. *Phys. Rev. B*, 76:201401(1–4), 2007.
- [131] P. Lespade, A. Marchand, M. Couzi, and F. Cruege. Characterisation de matériaux carbonés par microspectrométrie Raman. *Carbon*, 22:375–385, 1984.
- [132] P. H. Tan, W. P. Han, W. J. Zhao, Z. H. Wu, K. Chang, H. Wang, Y. F. Wang, N. Bonini, N. Marzari, N. Pugno, G. Savini, A. Lombardo, and A. C. Ferrari. The shear mode of multilayer graphene. *Nature Materials*, 11:294–300, 2012.
- [133] A. Das, S. Pisana, B. Chakraborty, S. Piscanec, S. K. Saha, U. V. Waghmare, K. S. Novoselov, H. R. Krishnamurthy, A. K. Geim, A. C. Ferrari, and A. K. Sood. Monitoring dopants by Raman scattering in an electrochemically top-gated graphene transistor. *Nature Nanotechnology*, 3:210–215, 2008.

- [134] S. Piscanec, S. Pisana, A. K. Sood, A. Das, B. Chakraborty and A. C. Ferrari. Phonon renormalization in doped bilayer graphene. *Phys. Rev. B*, 79:155417(1–7), 2009.
- [135] S. Pisana, M. Lazzeri, C. Casiraghi, K. S. Novoselov, A. K. Geim, A. C. Ferrari, and F. Mauri. Breakdown of the adiabatic Born–Oppenheimer approximation in graphene. *Nature Materials*, 6:198–201, 2007.
- [136] Z. H. Ni, T. Yu, Y. H. Lu, Y. Y. Wang, Y. P. Feng, and Z. X. Shen. Uniaxial strain on graphene: Raman spectroscopy study and band–gap opening. *ACS Nano*, 2:2301–2305, 2008.
- [137] T. M. G. Mohiuddin, A. Lombardo, R. R. Nair, A. Bonetti, G. Savini, R. Jalil, N. Bonini, D. M. Basko, C. Galiotis, N. Marzari, K. S. Novoselov, A. K. Geim, and A. C. Ferrari. Uniaxial strain in graphene by Raman spectroscopy: G peak splitting, Grüneisen parameters, and sample orientation. *Phys. Rev. B*, 79:205433(1–8), 2009.
- [138] M. Huang, H. Yan, C. Chen, D. Song, T. F. Heinz, and J. Hone. Phonon softening and crystallographic orientation of strained graphene studied by Raman spectroscopy. *Proceedings of the National Academy of Sciences of the United States of America*, 106:7304–7308, 2009.
- [139] V. Geringer, M. Liebmann, T. Echtermeyer, S. Runte, M. Schmidt, R. Rckamp, M. C. Lemme, and M. Morgenstern. Intrinsic and extrinsic corrugation of monolayer graphene deposited on SiO₂. *Phys. Rev. Lett.*, 102:076102(1–4), 2009.
- [140] J. E. Lee, G. Ahn, J. Shim, Y. S. Lee, and S. Ryu. Optical separation of mechanical strain from charge doping in graphene. *Nature Communications*, 3:1–8, 2012.
- [141] C. Metzger, S. Rémi, M. Liu, S. V. Kusminskiy, A. H. C. Neto, A. K. Swan, and B. B. Goldberg. Biaxial Strain in Graphene Adhered to Shallow Depressions. *Nano Lett.*, 10:6–10, 2010.
- [142] J. Zabel, R. R. Nair, A. Ott, T. Georgiou, A. K. Geim, K. S. Novoselov, and C. Casiraghi. Raman Spectroscopy of Graphene

- and Bilayer under Biaxial Strain: Bubbles and Balloons. *Nano Lett.*, 12:617–621, 2012.
- [143] Q. H. Wang, K. Kalantar-Zadeh, A. Kis, J. N. Coleman, and M. S. Strano. Electronics and optoelectronics of two-dimensional transition metal dichalcogenides. *Nature Nanotechnology*, 7:699–712, 2012.
- [144] Th. Böker, R. Severin, A. Müller, C. Janowitz, and R. Manzke. Band structure of MoS_2 , MoSe_2 , and $\alpha\text{-MoTe}_2$: Angle-resolved photoelectron spectroscopy and ab initio calculations. *Phys. Rev. B*, 64:235305(1–11), 2001.
- [145] B. Schonfeld, J. J. Huang, and S. C. Moss. Anisotropic Mean-Square Displacements (MSD) in Single Crystals of 2H- and 3R- MoS_2 . *Acta Cryst. B*, 39:404–407, 1983.
- [146] S. Sugai and T. Ueda. High-pressure Raman spectroscopy in the layered materials 2H- MoS_2 , 2H- MoSe_2 , and 2H- MoTe_2 . *Phys. Rev. B*, 26:6554–6558, 1982.
- [147] T.J. Wieting, A. Grisel, and F. Lévy. INTERLAYER BONDING AND LOCALIZED CHARGE IN MoSe_2 AND $\alpha\text{-MoTe}_2$. *Physica B*, 99:337–342, 1980.
- [148] A. Kumar and P. K. Ahluwalia. Electronic structure of transition metal dichalcogenides monolayers 1H- MX_2 ($\text{M} = \text{Mo}, \text{W}$; $\text{X} = \text{S}, \text{Se}, \text{Te}$) from ab-initio theory: new direct band gap semiconductors. *Eur. Phys. J. B*, 85:186–192, 2012.
- [149] K. F. Mak, C. Lee, J. Hone, J. Shan, and T. F. Heinz. Atomically Thin MoS_2 : A New Direct-Gap Semiconductor. *Phys. Rev. Lett.*, 105:136805(1–4), 2010.
- [150] G. Eda, H. Yamaguchi, D. Voiry, T. Fujita, M. Chen, and M. Chhowalla. Photoluminescence from Chemically Exfoliated MoS_2 . *Nano Lett.*, 11:5111–5116, 2011.
- [151] A. Splendiani, L. Sun, Y. Zhang, T. Li, J. Kim, C. Y. Chim, G. Galli, and F. Wang. Emerging Photoluminescence in Monolayer MoS_2 . *Nano Lett.*, 10:1271–1275, 2010.

- [152] A. Ramasubramaniam, D. Naveh, and E. Towe. Tunable band gaps in bilayer transition–metal dichalcogenides. *Phys. Rev. B*, 84:205325(1–10), 2011.
- [153] A. N. Enyashin and G. Seifert. Density–functional study of Li_xMoS_2 intercalates ($0 \leq x \leq 1$). *Computational and Theoretical Chemistry*, 999:13–20, 2012.
- [154] T. Ando, A. B. Fowler, and F. Stern. Electronic–properties of two–dimensional systems. *Reviews of Modern Physics*, 54:437–672), 1982.
- [155] F. Stern and W. E. Howard. Properties of Semiconductor Surface Inversion Layers in the Electric Quantum Limit. *Phys. Rev.*, 163:816–835, 1967.
- [156] R. E. Prange and T. W. Nee. Quantum Spectroscopy of the Low–Field Oscillations in the Surface Impedance. *Phys. Rev.*, 168:779–786, 1968.
- [157] B. Radisavljevic, A. Radenovic, J. Brivio, V. Giacometti, and A. Kis. Single–layer MoS_2 transistors. *Nature Nanotechnology*, 6:147–150, 2011.
- [158] D. Jena and A. Konar. Enhancement of Carrier Mobility in Semiconductor Nanostructures by Dielectric Engineering. *Phys. Rev. Lett*, 98:136805(1–4), 2007.
- [159] S. Kim, A. Konar, W.-S. Hwang, J. H. Lee, J. Lee, J. Yang, C. Jung, H. Kim, J.-B. Yoo, J.-Y. Choi, Y. W. Jin, S. Y. Lee, D. Jena, W. Choi, and K. Kim. High–mobility and low–power thin–film transistors based on multilayer MoS_2 crystals. *Nature Communications*, 3:1–7, 2012.
- [160] R. Fivaz and E. Mooser. Mobility of charge carriers in semiconducting layer structures. *Phys. Rev.*, 163:743–755, 1967.
- [161] C. Lee, H. Yan, L. E. Brus, T. F. Heinz, J. Hone, and S. Ryu. Anomalous Lattice Vibrations of Single and Few–Layer MoS_2 . *ACS Nano*, 4:2695–2700, 2010.

- [162] H. Li, Q. Zhang, C. C. R. Yap, B. K. Tay, T. H. T. Edwin, A. Olivier, and D. Baillargeat. From Bulk to Monolayer MoS₂ : Evolution of Raman Scattering. *Adv. Funct. Mater.*, 22:1385–1390, 2012.
- [163] D. J. Late, B. Liu, H. S. S. R. Matte, C. N. R. Rao, and V. P. Dravid. Rapid Characterization of Ultrathin Layers of Chalcogenides on SiO₂/Si Substrates. *Adv. Funct. Mater.*, 22:1894–1905, 2012.
- [164] V. Varshney, S. S. Patnaik, C. Muratore, A. K. Roy, A. A. Voevodin, and B. L. Farmer. MD simulations of molybdenum disulphide (MoS₂): Force-field parameterization and thermal transport behavior. *Computational Materials Science*, 48:101–108, 2010.
- [165] J. Y. Kim, S. M. Choi, W. S. Seo, and W. S. Cho. Thermal and Electronic Properties of Exfoliated Metal Chalcogenides. *Bull. Korean Chem. Soc.*, 31:3225–3227, 2010.
- [166] S. Bertolazzi, J. Brivio, and A. Kis. Stretching and Breaking of Ultrathin MoS₂. *ACS Nano*, 5:9703–9709, 2011.
- [167] A. Castellanos-Gomez, M. Poot, G. A. Steele, H. S. J. van der Zant, N. Agrait, and G. Rubio-Bollinger. Elastic Properties of Freely Suspended MoS₂ Nanosheets. *Adv. Mater.*, 24:772–775, 2012.
- [168] P. Johari and V. B. Shenoy. Tuning the Electronic Properties of Semiconducting Transition Metal Dichalcogenides by Applying Mechanical Strains. *ACS Nano*, 6:5449–5456, 2012.
- [169] T. Li. Ideal strength and phonon instability in single-layer MoS₂. *Phys. Rev. B*, 85:235407(1–5), 2012.
- [170] B. Radisavljevic, M. B. Whitwick, and A. Kis. Integrated Circuits and Logic Operations Based on Single-Layer MoS₂. *ACS Nano*, 5:9934–9938, 2011.
- [171] B. Radisavljevic, M. B. Whitwick, and A. Kis. Small-signal amplifier based on single-layer MoS₂. *Appl. Phys. Lett.*, 101:043103(1–4), 2012.

- [172] H. Wang, L. Yu, Y. H. Lee, Y. Shi, A. Hsu, M. L. Chin, L. J. Li, M. Dubey, J. Kong, and T. Palacios. Integrated Circuits Based on Bilayer MoS₂ Transistors. *Nano Lett.*, 12:4674–4680, 2012.
- [173] W. Bao, X. Cai, D. Kim, K. Sridhara, and M. S. Fuhrer. High mobility ambipolar MoS₂ field-effect transistors: Substrate and dielectric effects. *Appl. Phys. Lett.*, 102:042104(1–4), 2013.
- [174] S. Das, H.-Y. Chen, A. V. Penumatcha, and J. Appenzeller. High Performance Multilayer MoS₂ Transistors with Scandium Contacts. *Nano Lett.*, 13:100–105, 2013.
- [175] S. Larentis, B. Fallahazad, and E. Tutuc. Field-effect transistors and intrinsic mobility in ultra-thin MoSe₂ layers. *Appl. Phys. Lett.*, 101:223104(1–4), 2012.
- [176] R. Späh, M. Lux-Steiner, M. Obergfell, E. Bucher, and S. Wagner. n-MoSe₂/p-WSe₂ heterojunctions. *Appl. Phys. Lett.*, 47:871–873, 1985.
- [177] K. F. Mak, K. He, J. Shan, and T. F. Heinz. Control of valley polarization in monolayer MoS₂ by optical helicity. *Nature Nanotechnology*, 7:494–498, 2012.
- [178] H. Zeng, J. Dai, W. Yao, D. Xiao, and X. Cui. Valley polarization in MoS₂ monolayers by optical pumping. *Nature Nanotechnology*, 7:490–493, 2012.
- [179] H. Liu, D. Su, R. Zhou, B. Sun, G. Wang, and S. Z. Qiao. Highly Ordered Mesoporous MoS₂ with Expanded Spacing of the (002) Crystal Plane for Ultrafast Lithium Ion Storage. *Adv. Energy Mater.*, 2:970–975, 2012.
- [180] G. Du, Z. Guo, S. Wang, R. Zeng, Z. Chenb, and H. Liu. Superior stability and high capacity of restacked molybdenum disulfide as anode material for lithium ion batteries. *Chem. Commun.*, 46:1106–1108, 2010.
- [181] H. Hwang, H. Kim, and J. Cho. MoS₂ Nanoplates Consisting of Disordered Graphene-like Layers for High Rate Lithium Battery Anode Materials. *Nano Lett.*, 11:4826–4830, 2011.

- [182] K. Chang and W. Chen. Single-layer MoS₂/graphene dispersed in amorphous carbon: towards high electrochemical performances in rechargeable lithium ion batteries. *J. Mater. Chem.*, 2011, 21, 17175, 21:17175–17184, 2011.
- [183] K. Chang, W. Chen, L. Ma, H. Li, H. Li, F. Huang, Z. Xu, Q. Zhangd, and J. Y. Leed. Graphene-like MoS₂/amorphous carbon composites with high capacity and excellent stability as anode materials for lithium ion batteries. *J. Mater. Chem.*, 21:6251–6257, 2011.
- [184] X. Zhou, L. J. Wan, and Y. G. Guo. Synthesis of MoS₂ nanosheet-graphene nanosheet hybrid materials for stable lithium storage. *Chem. Commun.*, 49:1838–1840, 2013.
- [185] K. Chang and W. Chen. In situ synthesis of MoS₂/graphene nanosheet composites with extraordinarily high electrochemical performance for lithium ion batteries. *Chem. Commun.*, 47:4252–4254, 2011.
- [186] X. Zhou, L. J. Wan, and Y. G. Guo. Facile synthesis of MoS₂@CMK-3 nanocomposite as an improved anode material for lithium-ion batteries. *Nanoscale*, 4:5868–5871, 2012.
- [187] Y. Liang, R. Feng, S. Yang, H. Ma, J. Liang, and J. Chen. Rechargeable Mg Batteries with Graphene-like MoS₂ Cathode and Ultrasmall Mg Nanoparticle Anode. *Adv. Mater.*, 23:640–643, 2011.
- [188] J. Morales, J. Santos, and J. L. Tirado. Electrochemical studies of lithium and sodium intercalation in MoSe₂. *Solid State Ionics*, 83:57–64, 1996.
- [189] Z. D. Huang, W. Bensch, L. Kienle, S. Fuentes, G. Alonso, and C. Ornelas. SBA-15 as Support for MoS₂ and Co-MoS₂ Catalysts Derived from Thiomolybdate Complexes in the Reaction of HDS of DBT. *Catal. Lett.*, 122:57–67, 2008.
- [190] X. Zong, H. Yan, G. Wu, G. Ma, F. Wen, L. Wang, and C. Li. Enhancement of Photocatalytic H₂ Evolution on CdS by Loading MoS₂ as Cocatalyst under Visible Light Irradiation. *J. Am. Chem. Soc.*, 130:7176–7177, 2008.

- [191] B. Hinnemann, P. G. Moses, J. Bonde, K. P. Jorgensen, J. H. Nielsen, S. Horch, I. Chorkendorff, and J. K. Nørskov. Biomimetic Hydrogen Evolution: MoS₂ Nanoparticles as Catalyst for Hydrogen Evolution. *J. Am. Chem. Soc.*, 127:5308–5309, 2005.
- [192] T. F. Jaramillo, K. P. Jorgensen, J. Bonde, J. H. Nielsen, S. Horch, and I. Chorkendorff. Identification of Active Edge Sites for Electrochemical H₂ Evolution from MoS₂ Nanocatalysts. *Science*, 317:100–102, 2007.
- [193] J. Chen, S. L. Li, Q. Xub, and K. Tanaka. Synthesis of open-ended MoS₂ nanotubes and the application as the catalyst of methanation. *Chem. Commun.*, pages 1722–1723, 2002.
- [194] K. H. Hua, X. G. Hua, and X. J. Sun. Morphological effect of MoS₂ nanoparticles on catalytic oxidation and vacuum lubrication. *Appl. Surf. Science*, 256:2517–2523, 2010.
- [195] Y. Li, H. Wang, L. Xie, Y. Liang, G. Hong, and H. Dai. MoS₂ Nanoparticles Grown on Graphene: An Advanced Catalyst for the Hydrogen Evolution Reaction. *J. Am. Chem. Soc.*, 133:7296–7299, 2011.
- [196] E. Gourmelon, O. Lignier, H. Hadouda, G. Couturier, J.C. Bernède, J. Tedd, J. Pouzet, and J. Salardenne. MS₂ (M = W, Mo) Photosensitive thin films for solar cells. *Solar Energy Materials and Solar Cells*, 46:115–121, 1997.
- [197] V. M. Pathak and R. Srivastava. Better Photoconversion Yield from MoSe₂ Based PEC Solar Cells. *Phys. Stat. Sol. a*, 134:37–40, 1992.
- [198] M. Wu, Y. Wang, X. Lin, N. Yu, L. Wang, L. Wang, A. Hagfeldt, and T. Ma. Economical and effective sulfide catalysts for dye-sensitized solar cells as counter electrodes. *Phys. Chem. Chem. Phys.*, 13:19298–19301, 2011.
- [199] J. Y. Lin, C. Y. Chan, and S. W. Chou. Electrophoretic deposition of transparent MoS₂graphene nanosheet composite films as counter electrodes in dye-sensitized solar cells. *Chem. Commun.*, 49:1440–1442, 2013.

- [200] C. J. Liu, S. Y. Tai, S. W. Chou, Y. C. Yu, K. D. Chang, S. Wang, F. S. S. Chien, J. Y. Lin, and T. W. Lin. Facile synthesis of MoS₂/graphene nanocomposite with high catalytic activity toward triiodide reduction in dye-sensitized solar cells. *J. Mater. Chem.*, 22:21057–21064, 2012.
- [201] G. Yue, J. Wu, Y. Xiao, M. Huang, J. Lina, and J. Y. Lin. High performance platinum-free counter electrode of molybdenum sulfide-carbon used in dye-sensitized solar cells. *J. Mater. Chem. A*, 1:1495–1501, 2013.
- [202] H. S. Lee, S.-W. Min, Y.-G. Chang, M. K. Park, T. Nam, H. Kim, J. H. Kim, S. Ryu, and S. Im. MoS₂ Nanosheet Phototransistors with Thickness-Modulated Optical Energy Gap. *Nano Lett.*, 12:3695–3700, 2012.
- [203] Z. Yin, H. Li, H. Li, L. Jiang, Y. Shi, Y. Sun, G. Lu, Q. Zhang, X. Chen, and H. Zhang. Single-Layer MoS₂ Phototransistors. *ACS Nano*, 6:74–80, 2012.
- [204] Q. He, Z. Zeng, Z. Yin, H. Li, S. Wu, X. Huang, and H. Zhang. Fabrication of Flexible MoS₂ Thin-Film Transistor Arrays for Practical Gas-Sensing Applications. *Small*, 19:2994–2999, 2012.
- [205] H. Li, Z. Yin, Q. He, H. Li, X. Huang, G. Lu, D. W. H. Fam, A. I. Y. Tok, Q. Zhang, and H. Zhang. Fabrication of Single- and Multilayer MoS₂ Film-Based Field-Effect Transistors for Sensing NO at Room Temperature. *Small*, 8:63–67, 2012.
- [206] F. K. Perkins, A. L. Friedman, E. Cobas, P. M. Campbell, G. G. Jernigan, and B. T. Jonker. Chemical Vapor Sensing with Monolayer MoS₂. *Nano Lett.*, 13:668–673, 2013.
- [207] S. Wu, Z. Zeng, Q. He, Z. Wang, S. J. Wang, Y. Du, Z. Yin, X. Sun, W. Chen, and H. Zhang. Electrochemically Reduced Single-Layer MoS₂ Nanosheets: Characterization, Properties, and Sensing Applications. *Small*, 8:2264–2270, 2012.
- [208] K. K. Liu, W. Zhang, Y. H. Lee, Y. C. Lin, M. T. Chang, C. Y. Su, C. S. Chang, H. Li, Y. Shi, H. Zhang, C. S. Lai, and L. J. Li. Growth of Large-Area and Highly Crystalline MoS₂ Thin Layers on Insulating Substrates. *Nano Lett.*, 12:1538–1544, 2012.

- [209] H. Li, G. Lu, Z. Yin, Q. He, H. Li, Q. Zhang, and H. Zhang. Optical Identification of Single- and Few-Layer MoS₂ Sheets. *Small*, 8:682–686, 2012.
- [210] M. Yamamoto, T. L. Einstein, M. S. Fuhrer, and W. G. Cullen. Anisotropic Etching of Atomically Thin MoS₂. *J. Phys. Chem. C*, 117:25643–25649, 2013.
- [211] N. Kang, H. P. Paudel, M. N. Leuenberger, L. Tetard, and S. I. Khondaker. Photoluminescence Quenching in Single-Layer MoS₂ via Oxygen Plasma Treatment. *J. Phys. Chem. C*, 118:21258–21263, 2014.
- [212] M. R. Islam, N. Kang, U. Bhanu, H. P. Paudel, M. Erementchouk, L. Tetard, M. N. Leuenberger, and S. I. Khondaker. Tuning the electrical property via defect engineering of single layer MoS₂ by oxygen plasma. *Nanoscale*, 6:10033–10039, 2014.
- [213] J. R. Ferraro, K. Nakamoto, and C. W. Brown. *Introductory Raman Spectroscopy*. Elsevier, 2003.
- [214] D. R. Vij. *Handbook of Applied Solid State Spectroscopy*. Springer, 2006.
- [215] R. García. *Amplitude Modulation Atomic Force Microscopy*. Wiley-VCH, 2010.
- [216] G. Haugstad. *ATOMIC FORCE MICROSCOPY; Understanding Basic Modes and Advanced Applications*. Wiley, 2012.
- [217] © 2008 BRUKER OPTIK GmbH. *Bruker SENTERRA Manual*.
- [218] © 2004 Veeco Instruments Inc. *Dimension 3100 Manual*.
- [219] G. Nicotra, Q. M. Ramasse, I. Deretzis, A. La Magna, C. Spinella, and F. Giannazzo. Delaminated Graphene at Silicon Carbide Facets: Atomic Scale Imaging and Spectroscopy. *ACS Nano*, 7:3045–3052, 2013.
- [220] K. V. Emtsev, A. Bostwick, K. Horn, J. Jobst, G. L. Kellogg, L. Ley, J. L. McChesney, T. Ohta, S. A. Reshanov, J. Röhrl, E. Rotenberg, A. K. Schmid, D. Waldmann, H. B. Weber, and

- T. Seyller. Towards wafer-size graphene layers by atmospheric pressure graphitization of silicon carbide. *Nature Materials*, 8:203–207, 2009.
- [221] F. Speck, J. Jobst, F. Fromm, M. Ostler, D. Waldmann, M. Hundhausen, H. B. Weber, and Th. Seyller. The quasi-free-standing nature of graphene on H-saturated SiC(0001). *Appl. Phys. Lett.*, 99:122106(1–3), 2011.
- [222] S. Sonde, F. Giannazzo, V. Raineri, R. Yakimova, J.-R. Huntzinger, A. Tiberj, and J. Camassel. Electrical properties of the graphene/4H-SiC (0001) interface probed by scanning current spectroscopy. *Phys. Rev. B*, 80:241406(1–4), 2009.
- [223] X. Wu, Y. Hu, M. Ruan, N. K Madiomanana, J. Hankinson, M. Sprinkle, C. Berger, and W. A. de Heer. Half integer quantum Hall effect in high mobility single layer epitaxial graphene. *Appl. Phys. Lett.*, 95:223108(1–3), 2009.
- [224] S. Sonde, F. Giannazzo, C. Vecchio, R. Yakimova, E. Rimini, and V. Raineri. Role of Graphene/Substrate Interface on the Local Transport Properties of the Two-Dimensional Electron Gas. *Phys. Lett.*, 97:132101(1–3), 2010.
- [225] G. Deokar, J. Avila, I. Razado-Colambo, J. L. Codron, C. Boyaval, E. Galopin, M. C. Asensio, and D. Vignaud. Towards High Quality CVD Graphene Growth and Transfer. *Carbon*, 89:82–92, 2015.
- [226] Y. Yin, Z. Cheng, L. Wang, and K. Jin W. Wang. Graphene, a material for high temperature devices-intrinsic carrier density, carrier drift velocity, and lattice energy. *Scientific Reports*, 4:5758(1–6), 2014.
- [227] SPI Supplies. SPI Supplies Molybdenum Disulfide (MoS₂) Crystal. Available on line: <http://www.2spi.com/item/z429ml/>.
- [228] G. Fisichella, S. Di Franco, F. Roccaforte, S. Ravesi, and F. Giannazzo. Microscopic mechanisms of graphene electrolytic delamination from metal substrates. *Appl. Phys. Lett.*, 104:233105(1–5), 2014.

- [229] A. Piazza, S. Agnello, I. Deretzis, A. La Magna, M. Scuderi, G. Nicotra, C. Spinella, G. Fisichella, F. Roccaforte, M. Cannas, F. M. Gelardi, R. Yakimova, and F. Giannazzo. Micro-Raman characterization of graphene grown on SiC(000-1). *IEEE 9th Nanotechnology Materials and Devices Conference, NMDC 2014*, pages 15–18, 2014.
- [230] D. S. Lee, C. Riedl, B. Krauss, K. von Klitzing, U. Starke, and J. H. Smet. Raman Spectra of Epitaxial Graphene on SiC and of Epitaxial Graphene Transferred to SiO₂. *Nano Lett.*, 8:4320–4325, 2008.
- [231] C. Vecchio, S. Sonde, C. Bongiorno, M. Rambach, R. Yakimova, V. Raineri, and F. Giannazzo. Nanoscale structural characterization of epitaxial graphene grown on off-axis 4H-SiC (0001). *Nanoscale Research Letters*, 6:269–275, 2011.
- [232] C. H. Lui, Z. Li, Z. Chen, P. V. Klimov, L. E. Brus, and T. F. Heinz. Imaging Stacking Order in Few-Layer Graphene. *Nano Lett.*, 11:164–169, 2011.
- [233] J. A. Robinson, C. P. Puls, N. E. Staley, J. P. Stitt, M. A. Fanton, K. V. Emtsev, T. Seyller, and Y. Liu. Raman Topography and Strain Uniformity of Large-Area Epitaxial Graphene. *Nano Lett.*, 9:964–968, 2009.
- [234] Y. Sato, K. Takai, and T. Enoki. Electrically Controlled Adsorption of Oxygen in Bilayer Graphene Devices. *Nano Lett.*, 11:3468–3475, 2011.
- [235] S. Berciaud, S. Ryu, L. E. Brus, and T. F. Heinz. Probing the Intrinsic Properties of Exfoliated Graphene: Raman Spectroscopy of Free-Standing Monolayers. *Nano Lett.*, 9:346–352, 2009.
- [236] G. Hong, Q.-H. Wu, C. Wang, J. Ren, T. Xu, W. Zhang, and S.-T. Lee. Surface doping of nitrogen atoms on graphene via molecular precursor. *Appl. Phys. Lett.*, 102:051610(1–4), 2013.
- [237] A. Nourbakhsh, M. Cantoro, T. Vosch, G. Pourtois, F. Clemente, M. H. van der Veen, J. Hofkens, M. M Heyns, S. De

- Gendt, and B. F. Sels. Bandgap opening in oxygen plasma-treated graphene. *Nanotechnology*, 21:435203(1–9), 2010.
- [238] S. M. Hornett, M. Heath, D. W. Horsell, and E. Hendry. Optically induced oxygen desorption from graphene measured using femtosecond two-pulse correlation. *Phys. Rev. B*, 90:081401(1–5), 2014.
- [239] J. Liu, L. Dong, C. Wang, T. Liang, and W. Lai. First principles study of oxidation behavior of irradiated graphite. *Nucl. Instr. and Meth. in Phys. Res. B*, 352:160–166, 2015.
- [240] Y. Yamada, K. Murota, R. Fujita, J. Kim, A. Watanabe, M. Nakamura, S. Sato, K. Hata, P. Ercius, J. Ciston, C. Y. Song, K. Kim, W. Regan, W. Gannett, and A. Zettl. Subnanometer Vacancy Defects Introduced on Graphene by Oxygen Gas. *J. Am. Chem. Soc.*, 136:2232–2235, 2014.
- [241] A. Piazza, F. Giannazzo, G. Buscarino, G. Fisichella, A. La Magna, F. Roccaforte, M. Cannas, F.M. Gelardi, and S. Agnello. Graphene p-Type Doping and Stability by Thermal Treatments in Molecular Oxygen Controlled Atmosphere. *J. Phys. Chem. C*, 119:22718–22723, 2015.
- [242] F. Giannazzo, S. Sonde, V. Raineri, G. Patanè, G. Compagnini, F. Aliotta, R. Ponterio, and E. Rimini. Optical, Morphological and Spectroscopic Characterization of Graphene on SiO₂. *Phys. Status Solidi C*, 7:1251–1255, 2010.
- [243] F. Giannazzo, S. Sonde, R. Lo Nigro, E. Rimini, and V. Raineri. Mapping the Density of Scattering Centers Limiting the Electron Mean Free Path in Graphene. *Nano Lett.*, 11:4612–4618, 2011.
- [244] A. Piazza, F. Giannazzo, G. Buscarino, G. Fisichella, A. La Magna, F. Roccaforte, M. Cannas, F.M. Gelardi, and S. Agnello. Effect of air on oxygen p-doped graphene on SiO₂. *Phys. Status Solidi A*, 213:2341–2344, 2016.
- [245] M. Kratzer, B. C. Bayer, P. R. Kidambi, A. Matković, R. Gajić, A. Cabrero-Vilatela, R. S. Weatherup, S. Hofmann, and C. Teichert. Effects of polymethylmethacrylate-transfer residues on

- the growth of organic semiconductor molecules on chemical vapor deposited graphene. *Appl. Phys. Lett.*, 106:103101(1–5), 2015.
- [246] Y. Ahn, H. Kim, Y.-H. Kim, Y. Yi, and S.-I. Kim. Procedure of removing polymer residues and its influences on electronic and structural characteristics of graphene. *Appl. Phys. Lett.*, 102:091602(1–5), 2013.
- [247] A. Piazza, F. Giannazzo, G. Buscarino, G. Fisichella, A. La Magna, F. Roccaforte, M. Cannas, F.M. Gelardi, B. Pignataro, M. Scopelliti, and S. Agnello. Substrate and atmosphere influence on oxygen p-doped graphene. *Carbon*, 107:696–704, 2016.
- [248] Q. H. Wang, Z. Jin, K. K. Kim, A. J. Hilmer, G. L. C. Paulus, C.-J. Shih, M.-H. Ham, J. D. Sanchez-Yamagishi, K. Watanabe, T. Taniguchi, J. Kong, P. Jarillo-Herrero, and M. S. Strano. Understanding and controlling the substrate effect on graphene electron-transfer chemistry via reactivity imprint lithography. *Nature Chemistry*, 4:724–732, 2012.
- [249] S.M. Song and B.J. Cho. Investigation of interaction between graphene and dielectrics. *Nanotechnology*, 21:335706(1–6), 2010.
- [250] A. Pirkle, J. Chan, A. Venugopal, D. Hinojos, C. W. Magnuson, S. McDonnell, L. Colombo, E. M. Vogel, R. S. Ruoff, and R. M. Wallace. The effect of chemical residues on the physical and electrical properties of chemical vapor deposited graphene transferred to SiO₂. *Appl. Phys. Lett.*, 99:122108(1–3), 2011.
- [251] S. Tian, Y. Yang, Z. Liu, C. Wang, R. Pan, C. Gu, and J. Li. Temperature-dependent Raman investigation on suspended graphene: Contribution from thermal expansion coefficient mismatch between graphene and substrate. *Carbon*, 104:27–32, 2016.
- [252] D. K. Schroder. *Semiconductors Materials and Device Characterization, third ed.* John Wiley & Sons, New York, 2006.
- [253] Y. Wang, Z. Ni, T. Yu, Z. X. Shen, H. Wang, Y. Wu, W. Chen, and A. T. S. Wee. Raman Studies of Monolayer Graphene: The Substrate Effect. *J. Phys. Chem. C*, 112:10637–10640, 2008.

- [254] F. Giannazzo, G. Nicotra, I. Deretzis, A. Piazza, G. Fisichella, S. Agnello, C. Spinella, A. La Magna, F. Roccaforte, and R. Yakimova. Graphene p-Type Doping and Stability by Thermal Treatments in Molecular Oxygen Controlled Atmosphere. *Materials Science Forum*, 858:1129–1132, 2016.
- [255] Y. Liu, C. Tan, H. Chou, A. Nayak, D. Wu, R. Ghosh, H.-Y. Chang, Y. Hao, X. Wang, J.-S. Kim, R. Piner, R. S. Ruoff, D. Akinwande, and K. Lai. Thermal Oxidation of WSe₂ Nanosheets Adhered on SiO₂/Si Substrates. *Nano Lett.*, 15:4979–4984, 2015.

Curriculum Vitae

Personal Information

<i>Surname</i>	Piazza
<i>First Name</i>	Aurora
<i>Nationality</i>	Italian
<i>Date of birth</i>	June 18, 1989
<i>Gender</i>	Female

Education

2007: Scientific High School "I.T.I.S. A. Volta" of Palermo (PA), Italy (77/100)

2012: Bachelor Degree in Physical Sciences (96/110) at the University of Palermo, Italy.

Thesis: "Determinazione sperimentale del rapporto carica-massa di un elettrone."; Tutor: Prof. S. Agnello

2013: Master Degree in Physic (110 cum laude/110) at the University of Palermo, Italy.

Thesis: "Modifiche dell'ossido di grafene e nanocompositi ossido di grafene/silice indotte da trattamenti termici."; Tutor: Prof. S. Agnello

June 2015: National School of Physical Chemistry, Otranto, (LE), Italy.

Publications

- S. Agnello, A. Piazza, A. Alessi, A. Maio, R. Scaffaro, G. Buscarino, F. M. Gelardi, R. Boscaino; "*Graphene oxide and Fumed silica graphene oxide nanocomposites modification by thermal treatments*"; NANOCON 2013 - Conference Proceedings, 5th International Conference, pp. 56-61 (2013);
- A. Piazza, S. Agnello, I. Deretzis, A. La Magna, M. Scuderi, G. Nicotra, C. Spinella, G. Fisichella, F. Roccaforte, M. Cannas, F. M. Gelardi, R. Yakimova, F. Giannazzo; "*Micro-Raman characterization of graphene grown on SiC(000-1)*"; 2014 IEEE 9th Nanotechnology Materials and Devices Conference, NMDC 2014, pp. 15-18 (2014);
- F. Giannazzo, G. Fisichella, A. Piazza, S. Agnello, F. Roccaforte; "*Nanoscale inhomogeneity of the Schottky barrier and resistivity in MoS₂ multilayers*"; Phys. Rev. B 92, 081307(1-4) (2015);
- A. Piazza, F. Giannazzo, G. Buscarino, G. Fisichella, A. La Magna, F. Roccaforte, M. Cannas, F. M. Gelardi, S. Agnello; "*Graphene p-Type Doping and Stability by Thermal Treatments in Molecular Oxygen Controlled Atmosphere*"; J. Phys. Chem. C, 119 (39), pp 2271822723, (2015);
- F. Giannazzo, G. Nicotra, I. Deretzis, A. Piazza, G. Fisichella, S. Agnello, C. Spinella, A. La Magna, F. Roccaforte, R. Yakimova; "*Interfacial disorder of graphene grown at high temper-*

atures on $4H\text{-SiC}(000\text{-}1)$ "; Materials Science Forum 858, pp. 1129-1132 (2016);

- A. Maio, S. Agnello, R. Khatibi, L. Botta, A. Alessi, A. Piazza, G. Buscarino, A. Mezzi, G. Pantaleo, R. Scaffaro; "*A rapid and eco-friendly route to synthesize graphene-doped silica nanohybrids*"; Journal of Alloys and Compounds 664, pp 428438 (2016);
- A. Piazza, F. Giannazzo, G. Buscarino, G. Fisichella, A. La Magna, F. Roccaforte, M. Cannas, F.M. Gelardi, S. Agnello; "*Effect of air on oxygen p-doped graphene on SiO_2* "; Phys. Status Solidi A 213, pp 23412344 (2016);
- A. Piazza, F. Giannazzo, G. Buscarino, G. Fisichella, A. La Magna, F. Roccaforte, M. Cannas, F. M. Gelardi, B. Pignataro, M. Scopelliti, S. Agnello; "*Substrate and atmosphere influence on oxygen p-doped graphene*"; Carbon 107, pp 696704 (2016).

Conferences partecipazione

- Oral presentation "*Micro-Raman characterization of graphene grown on Silicon Carbide*" at IEEE 9th Nanotechnology Materials and Devices Conference, NMDC October 12nd-15th, 2014 Aci Castello, (CT), Italy; (2014)
- Oral presentation "*Doping graphene with thermal treatments in oxygen controlled atmosphere*" at E-MRS Spring Meeting, May 11st-15th, 2015 Lille, France (2015);
- Oral presentation "*Ambient stability of oxygen p-doped graphene*" at FisMat 2015, Italian National Conference on Condensed Matter Physics, September 28th - October 2nd, 2015, Palermo, Italy (2015);
- Poster presentation "*Current injection from metal to MoS₂ probed at nanoscale*" at FisMat 2015, Italian National Conference on Condensed Matter Physics, September 28th - October 2nd, 2015, Palermo, Italy (2015);
- Oral presentation "*Role of ambient gas in the doping of graphene by thermal treatments*" at E-MRS Spring Meeting, May 2nd-6th, 2016 Lille, France (2016);

- Oral presentation "*In-situ monitoring thermal doping in O₂ controlled atmosphere of graphene and MoS₂ by Raman spectroscopy*" at NanoSEA 2016, July 3rd-8th, 2016 Giardini Naxos (ME), Italy.

Acknowledgments

In this space I would like to thank all the people that contributed to the realization of this thesis and who have provided me all the essential basis in these years of study.

The first thanks go to Dr. Filippo Giannazzo and Prof. Simonpietro Agnello for giving me the opportunity to explore an interesting research topic, for their great availability and patience and the many answer to questions (in addition to sustain me during these years!).

Furthermore, I would like to thank Dr. Corrado Spinella, former director of CNR-IMM, Catania and Dr. Guglielmo Fortunato, present director, for the access to the facilities of the institute, in particular to the AFM laboratory, the clean room and TEM.

Special thanks go to the CHAB laboratories for the AFM, XPS, Linkam equipments use (<http://www.chab.center/home>, *Med – CHHAB, PONA30273*, University of Palermo).

I would also like to thank the members of CNR-IMM of Catania (<https://hq.imm.cnr.it/>), especially Dr. Fabrizio Roccaforte, Dr. Patrick Fiorenza, Dr. Raffaella Lo Nigro, Dr. Domenico Corso and the members of the LAMP group (<http://www.unipa.it/lamp/>) of the department of physics and chemistry of Palermo in particular Prof. Roberto Boscaino, Prof. Franco Gelardi, Prof. Marco Cannas, Dr. Gianpiero Buscarino, Dr. Fabrizio Messina, the Dr. Luisa Sciortino and Dr. Antonino Alessi for the many and valuable advices, suggestions as well as scientific and technical support.

A big acknowledgement goes to Giacomo Tricomi, Gianluca Napoli of the department of physics and chemistry of the University of Palermo for the valuable assistance during the thermal treatments in a controlled atmosphere and Salvatore Di Franco of CNR-IMM of Catania for the skillful assistance with cleanroom equipment and the

sample preparation.

Prof. R. Yakimova, University of Linköping (Sweden), is acknowledged for the collaboration in the growth of graphene on SiC(000 $\bar{1}$) by thermal sublimation at high temperature.

My thanks go also to other members of the CNR-IMM, Dr. Giuseppe Nicotra and Corrado Bongiorno for the useful TEM analysis, Dr. Antonino La Magna and Dr. Ioannis Deretzis for their contribution with simulations.

Prof. B. Pignataro and Dr. M. Scopelliti are acknowledged for XPS analysis.

A loving thank you goes to Marilena, Giuseppe, Gabriele, Michela, Luisa, Emanuela e Pietro for sharing with me the long days in the laboratory and for the fruitful exchange of ideas.

Finally, but not least, a special thanks goes to Davide and to my parents who have allowed me to achieve this great objective always encouraging me, even kilometers far away.

GRAZIE!